Chemical Industry & Chemical Engineering Quarterly

SERBIA

Belgrade

AChE

Chemical Industry & Chemical Engineering CI&CE Quarterly

CONTENTS

The activities of the Association of Chemical Engineers of Serbia are supported by:

MINISTRY OF SCIENCE,
TECHNOLOGICAL DEVELOPMENT
AND INNOVATION
OF REPUBLIC OF SERBIA

Faculty of Technology and
Metallurgy, University of Belgrade

Faculty of Science, University of Novi Sad

Institute for Technology of Nuclear
and Other Mineral Raw Materials,
Bekgrade

Faculty of Technology,
University of Novi Sad

Institute of Chemistry, Technology and Metallurgy,
University of Belgrade

Faculty of Technical Sciences
University of Novi Sad

Faculty of Technology,
University of Niš, Leskovac

Faculty of Technical Sciences,
University of Priština, Kosovska Mitrovica

IMS Institute, Belgrade

DCP HEMIGAL
Leskovac

Elixir Prahovo

ROBERTA DEL SOLE
ALVARO MAGGIO
LUCIA MERGOLA

¹Department of Engineering for Innovation, University of Salento, Lecce, Italy

GREEN GRAPE MARC BIOSORBENTS PREPARATION FOR MERCURY REMOVAL IN AQUEOUS MEDIA

Article Highlights
- Grape marc-based biosorbents from wastes of Negroamaro wine production
- The green approach was used in biosorbent preparation with water, ethanol, and citric acid
- Biosorbent has a good adsorption capacity of Hg(II) ions in the water of 36.39 mg g^{-1}
- A physical adsorption mechanism of Hg(II) on the biosorbent was observed
- Biosorbent selectivity compared to Cu(II) and Ni(II) was proven

Abstract

In this study, grape marc waste from Negroamaro (a South of Italy vine variety) winery production was used to prepare biosorbents for Hg(II) removal in aqueous media. A green approach was used to develop a proper biosorbent through two different grape marc washing procedures. In particular, the common chloridric acid and the greener citric acid were evaluated. The biosorbent prepared using citric acid as a washing agent (GM-CA) gave similar results to the biosorbent washed with HCl (GM-HCl) with a maximum adsorption capacity of 36.39 mg g^{-1}. Isothermal studies revealed heterogeneous physical adsorption of Hg(II) on the biosorbents. Moreover, FTIR analysis of the grape marc-based biosorbent without and with Hg(II) confirmed ionic interactions in the biosorbent that fit with a pseudo-second-order kinetic model. Furthermore, no significant adsorption on the biosorbent was observed when two other heavy metals, copper(II) and nickel(II), previously studied for similar sorbents, were considered. Finally, the reusability of GM-CA biosorbent was also demonstrated over three cycles. Thus, the green preparation approach used in this work can be considered suitable for developing grape marc-based biosorbents.

Keywords: adsorption isotherms, citric acid, Hg(II) removal, grape marc, green waste biosorbent, kinetic study.

Nowadays, the widespread diffusion of heavy metals in the environment, mainly released from industrial and agricultural processes, is one of the major and critical issues in the fight against pollution. The World Health Organization considered mercury one of the most hazardous pollutants for human health [1]. Mercury ions and organomercury compounds are easily solubilized in water and living tissues. As a result, they can bioaccumulate in the human body, causing weakness, damage to the central nervous system, chromosomal mutations, etc., with lesser effects on the renal and gastrointestinal sections [2,3]. Its chemical and physical characteristics are fundamental for industrial processes such as pharmaceutical, oil refinery, electroplating, battery manufacturing, and mining activities [4]. Conventional methods for Hg(II) removal from water include solvent extraction, coagulation-flocculation, flotation, membrane filtration, ion exchange resin, and bioremediation [5–8]. However, traditional methods used to remove metal and heavy metal ions have many disadvantages, such as incomplete removal, low selectivity, the need to use chemical reagents, and high energy costs.

In the last years, the interest in materials, defined

as biopolymers, extracted from natural matrices with a potential adsorbent capacity of metal ions, has grown considerably for the development of new treatment techniques and alternative technologies for the removal of toxic metals, especially from natural water and wastewater [9]. Biopolymers have interesting characteristics, such as easy availability, low cost, high binding capacity, biodegradability, and the possibility of reuse. Most of these materials derive from agricultural products processing, fruit, wood, and barks, as well as wastes of the textile and fish industries. It is important to underline the significance of using biopolymers since it is in line with some of the fundamental principles of the circular economy, such as the careful and efficient management of resources and their recycling and reuse. In this contest, recent biosorbents, such as Rosmarinus officinalis leaves [10], Spanish broom plants [11], and exhausted coffee waste [12] were used for the removal of Hg(II) from water. Grape marc represents a widespread biopolymer that remains a byproduct of wine-making production. Tens of millions of tons of grapes are produced worldwide each year and are mainly used for wine production. Currently, grape marc is directly treated as fertilizer and animal feed. However, it is worth noting that some efforts are addressed in developing other more profitable grape marc utilization that point out their high potential commercial value.

Additionally, as reported by the International organization of vine and wine (OIV), Italy has been the largest wine-producing nation in the world, at least for the last four years [13]. Thus, in this work, the adsorption behavior of grape marc for mercury removal was studied. Chemical-physical characterization of grape marc has been extensively studied [14], as well as its application as a source of added-value compounds. A recent review of Muhlack *et al.* covers the value-added uses via extraction of valuable components from grape marc and thermochemical and biological treatments for energy recovery [15]. Furthermore, grape marc has been used as a potential biosorbent for the adsorption of organic compounds such as pesticides [16] and caffeine [17]. On the contrary, the application of grape marc for metal ions adsorption has been only little considered in the literature, such as the removal of Cd(II) ions [18], Cu(II), and Ni(II) ions [19] and Cr(VI), Cu(II), Ni(II) ions [20,21]. To our knowledge, the use of grape marc for mercury ion adsorption has not been considered in the literature.

The present work aims first to study the potential use of grape marc wasted from red wine production in Salento, a South of Italy area, as a biosorbent for mercury removal. A green procedure that employs green substances such as ethanol, citric acid (CA), and water during the preparation procedure, was

developed. A comparison was made between the common chloridric acid and the greener citric acid as a washing agent. Both prepared grape marc biosorbents, GM-HCl and GM-CA, were tested in batch Hg(II) adsorption experiments. The pH of Hg(II) ions solutions was considered to evaluate the performance of the biosorbent at pH 7 to minimize additional pretreatment of the water sample. A complete isotherm study was made using Langmuir, Freundlich, Temkin, and Dubinin-Radushkevich (D-R) equations. Further, kinetics, FTIR characterization, comparative experiments with other metal ions, and reusability were also evaluated.

MATERIAL AND METHODS

Chemicals

Mercury(II) chloride ($HgCl_2$), anhydrous CA, and $Cu(NO_3)_2 \cdot 2.5H_2O$ were supplied from Sigma-Aldrich (Steinheim, Germany). $Ni(NO_3)_2 \cdot 6H_2O$ was purchased from Fluka (Steinheim, Germany). Analytical grade ethanol and HCl 36-38% were obtained from J.T. Baker (Deventer, Holland). Nitric Acid (67-69%) for trace metal analysis, Ni(II), Cu(II), and Hg(II) standard solutions (1000 mg L^{-1}) were supplied from Romil-SpA. All solutions were prepared with deionized water provided by a water purification system (Human Corporation, Korea).

Instrumentation

Fourier transform infrared spectroscopy (FTIR) analysis was performed on a JASCO 660 plus infrared spectrometer. UV-vis analyses were performed by using a Jasco V-660 UV−visible spectrophotometer. An ultrasonic water bath from Bandelin Electronic, Sonorex RK 102H, was used (Bandelin Electronic, Berlin, Germany, Europe, www.bandelin.com). A centrifuge PK121 multispeed of Thermo Electron Corporation was adopted (Thermo Electron Corporation, Waltham, Massachusetts, USA, www.thermoscientific.com). Equilibrium batch adsorption studies and selectivity evaluations were carried out using a Thermo Scientific inductively coupled plasma mass spectrometry (ICP-MS) iCAP Q (Thermo Fisher, Scientific, Waltham, USA). pH was defined using a pH meter (Basic 20, Crison, Alella, Barcelona, Spain).

Biosorbents collection and preparation

Grape marc of Negroamaro variety, achieved in the wine production process, were supplied by a wine manufacturer in the Salento region (Lecce, Italy). They were sun-dried for three days, milled using a grinder, and finally sieved (< 2 mm) to remove coarse particles

and fibers. After that, the biosorbents preparation process was carried out following various washing steps described below. Each washing step was made by shaking the dispersion for 15−30 min at 250 rpm, centrifugation for 15 min at 9000 rpm, and finally with the supernatant removal.

After a preliminary washing in water, grape marc was washed with ethanol to remove the most polar organic components, which could interfere with the adsorption process, until no UV-vis absorbance was observed in the 280−800 nm.

Washings with acidic aqueous solutions were carried out to eliminate most cation ions in the grape marc. Thus, different experimental conditions were adopted by using HCl (0.1 M, pH 1), similar to the pH used in the literature [19], and also with CA at milder pH conditions that were pH 3 (0.002 M) and pH 2 (0.6 M). The number of washings was defined by monitoring cation ions concentration (Ca^{2+}, Mg^{2+}, K^+, and Na^+) using ICP-MS until a value lower than 1 mg L^{-1} was found. After, five washings with water were made to eliminate the acidic environment and chlorine or citrate ions. Finally, the biosorbents were dried in the oven at 60 °C till constant weight was reached. The above-described adsorbents were tested with an aqueous solution of Hg(II) (100 mg L^{-1}) and washed five times with the aqueous solution of HCl (0.1 M, pH 1) or CA (0.6 M, pH 2), denoted GM-HCl and GM-CA, respectively, that were selected for further studies.

Hg(II) adsorption experiments

Batch adsorption experiments were performed for both biosorbents GM-HCl and GM-CA by shaking the dispersion prepared by mixing 3 mg of the dry biosorbent with 3 ml of $HgCl_2$ aqueous solution at known concentrations in the range of 23−300 mg L^{-1} [18,22]. The mixture was shaken for 20 h at room temperature and 250 rpm and filtrated through a 0.20 μm filter to remove the sorbent. The solution was then analyzed to determine Hg(II) concentration by ICP-MS. The ion amount adsorbed on the biosorbent matrix (mg g^{-1}) was calculated by the following equation:

$$q_e = (C_i - C_e)\frac{V}{m} \qquad (1)$$

where C_i is the initial Hg(II) concentration (mg L^{-1}) and C_e is the equilibrium metal ion concentration (mg L^{-1}), V is the volume of Hg(II) aqueous solution (L), and m is the mass of biosorbent (g). Each experiment was carried out in triplicate.

Isotherms studies

The adsorption data were fitted into four linearized Langmuir, Freundlich, Temkin, and D-R isotherms [22]. Langmuir isotherm model describes the formation of a monolayer adsorbate on the outer surface of the biosorbent, and it is represented in the following linear form [12,18,22,23,24]:

$$\frac{1}{q_e} = \frac{1}{q_{max}C_e K_L} + \frac{1}{q_{max}} \qquad (2)$$

where q_e is the amount of Hg(II) adsorbed per gram of biosorbent at equilibrium (mg g^{-1}), C_e is the equilibrium Hg(II) concentration (mg L^{-1}) of the incubated solution, while K_L (L mg^{-1}) and q_{max} (mg g^{-1}) are the Langmuir equilibrium constant and the maximum monolayer adsorption capacity of the biosorbent respectively that are calculated from the slope and intercept of the linear plot of 1 q_e^{-1} versus $1/C_e$.

The linearized Freundlich equation [12,18,22,24] is used to describe the adsorption characteristics of the heterogeneous surface:

$$\ln q_e = \ln K_f + \frac{1}{n}\ln C_e \qquad (3)$$

where q_e (mg g^{-1}) and C_e (mg L^{-1}) are defined above while K_f and n are Freundlich isotherm constant related to the apparent affinity constant and adsorption intensity related to the number of the sites, respectively K_f and n were determined respectively from the intercept and slope of the linear plot of $\ln q_e$ versus $\ln C_e$.

The linearized Temkin isotherm [22], considering the effect of the adsorbate interaction on adsorption, is given by the following equation:

$$q_e = B\ln A_t + B\ln C_e \qquad (4)$$

$$B = RT / b_T \qquad (5)$$

where A_t is the Temkin isotherm equilibrium binding constant (L g^{-1}) and B is the constant related to the heat of adsorption (J mol^{-1}) that can be calculated respectively from the intercept and slope plot of q_e versus $\ln C_e$. Moreover, in Eq. (5), R (J $mol^{-1}K^{-1}$) is the universal gas constant, T (K) is the temperature, and b_T is a parameter associated with the heat of adsorption.

Finally, the D-R model [18,22], which does not assume a homogeneous surface or a constant biosorption potential, is given by Eq. (6):

$$\ln q_e = -K_{ad}\varepsilon^2 + \ln \ln q_{max} \qquad (6)$$

where K_{ad} and ε are the coefficients associated with the free energy adsorption (mol^2 kJ^{-2}) and the Polanyi's potential (kJ mol^{-1}), respectively, calculated from the slope and the intercept of $\ln q_e$ versus $\ln q_{max}$.

The free energy of adsorption E (kJ mol^{-1}), used to distinguish the physical and chemical adsorption of metal ions, was determined from K_{ad} following Eq. (7):

$$E = \frac{1}{\sqrt{2K_{ad}}} \qquad (7)$$

FTIR biosorbent characterization

FTIR spectra were registered on KBr pellets through 64 scans between 4000 and 650 cm^{-1}. Pellets were prepared by mixing a few dry biosorbent particles (1 mg) in 100 mg of KBr matrix and successively pressed at 10 tons. After incubation with 150 mg L^{-1} Hg(II) aqueous solution, the GM-CA was filtered and dried in the oven at 60 °C for two days (enough to reach a stable sample weight) before pellet preparation.

Kinetic adsorption

A kinetic adsorption experiment was performed, measuring Hg(II) concentration, in the incubated solution, at different times (t) up to 20 h. First, the adsorption experiment for biosorbent GM-CA was carried out following the procedure described in (Hg(II) adsorption experiments) by using an initial concentration of Hg(II) equal to 78 mg L^{-1} (C_i). Then, using Eq. (1), the milligrams of Hg(II) adsorbed per gram of biosorbent at time t, q_t (mg g^{-1}), was calculated by the difference between C_i and C_t, the concentration at the adsorption time t.

Kinetic adsorption data were fitted using two commonly adopted kinetic models: pseudo-first order and pseudo-second order [23]. The pseudo-first-order Lagergren model was expressed as Eq. (8):

$$\log(q_e - q_t) = \log \log(q_e) - \frac{K_1}{2.303}t \qquad (8)$$

where q_e is the milligram of Hg(II) adsorbed per gram of biosorbent at equilibrium, while q_t is the milligram of Hg(II) adsorbed per gram of biosorbent at time t, and K_1 (min^{-1}) is the rate constant of the first-order adsorption.

The pseudo-second-order model was given by Eq. (9):

$$\frac{t}{q_t} = \frac{1}{K_2 q_e^2} + \frac{1}{q_e}t \qquad (9)$$

where K_2 (g mg^{-1} min^{-1}) is the rate constant of the pseudo-second-order adsorption.

Comparative adsorption studies

The adsorption capacity of GM-CA biosorbent for other two divalent metal ions, Cu(II) and Ni(II), was measured. In particular aqueous solutions of 100 mg L^{-1} of Cu(II) and Ni(II) were prepared and used for batch experiments following the same procedure described for Hg(II) adsorption experiments. Eq. (1) was used to calculate their adsorption capacity. Each experiment was carried out in triplicate.

Reusability procedure

The reusability of GM-CA biosorbent was tested by washing the impregnated biosorbent after each batch experiment procedure. In detail, 30 mg of biosorbent was incubated with 30 mL of a Hg(II) 100 mg L^{-1} aqueous solution and taken under stirring for 7 h at 250 rpm to reach the adsorption equilibrium. Then, the mixture was centrifuged for 15 min at 9000 rpm, the supernatant was filtered and analyzed using ICP-MS to measure Hg(II) concentration, and the adsorption capacity qe was evaluated. Next, the impregnated biosorbent was treated with a 0.1 M (pH 1) solution of HCl and stirred for 30 min to release the adsorbed Hg(II). Then it was washed with water until neutral pH reached and finally dried before its reuse. The procedure herein described was repeated for three cycles. Finally, the regeneration efficiency (*RE*) was determined by using the following equation:

$$RE = q_n / q_0 \qquad (10)$$

where q_0 is the adsorption capacity before the regeneration process (mg g^{-1}) and q_n is the adsorption capacity (mg g^{-1}) at the n adsorption cycle. The same reusability procedure was carried out using a 0.6 M (pH 2) solution of CA for Hg(II) release.

RESULTS AND DISCUSSION

Biosorbents preparation

Fermented grape marc samples were collected from a small local winemaker at the end of the red Negroamaro wine production process and adequately treated. Grape marc represents a cheap and abundant wine production waste in the Salento area, and its utilization is of great interest (Figure 1).

After preliminary drying, grinding, and sieving steps to remove coarse particles and fibers, a progressive extraction process of polar organic compounds and ions was made by using ethanol, acidified water, and water. It is worth noting that a green approach was also adopted to set up the biosorbent preparation process. To this aim, only green solvents, water and ethanol, were used. Grape marc was firstly washed with ethanol to remove the polar organic compounds to avoid contamination of the analyzed solutions during the adsorption process. Moreover, it is interesting to note that the ethanol washing procedure could be helpful for successive value-added uses since the recovered supernatants contain polar organic extractives that could also be isolated as valuable products. Grape marc includes skin, seeds, and stalks with a variety of polar organic compounds that could be used by the food, cosmetic, and pharmaceutical industries. Thus, it can be considered a promising source of phytochemicals, phenolic compounds,
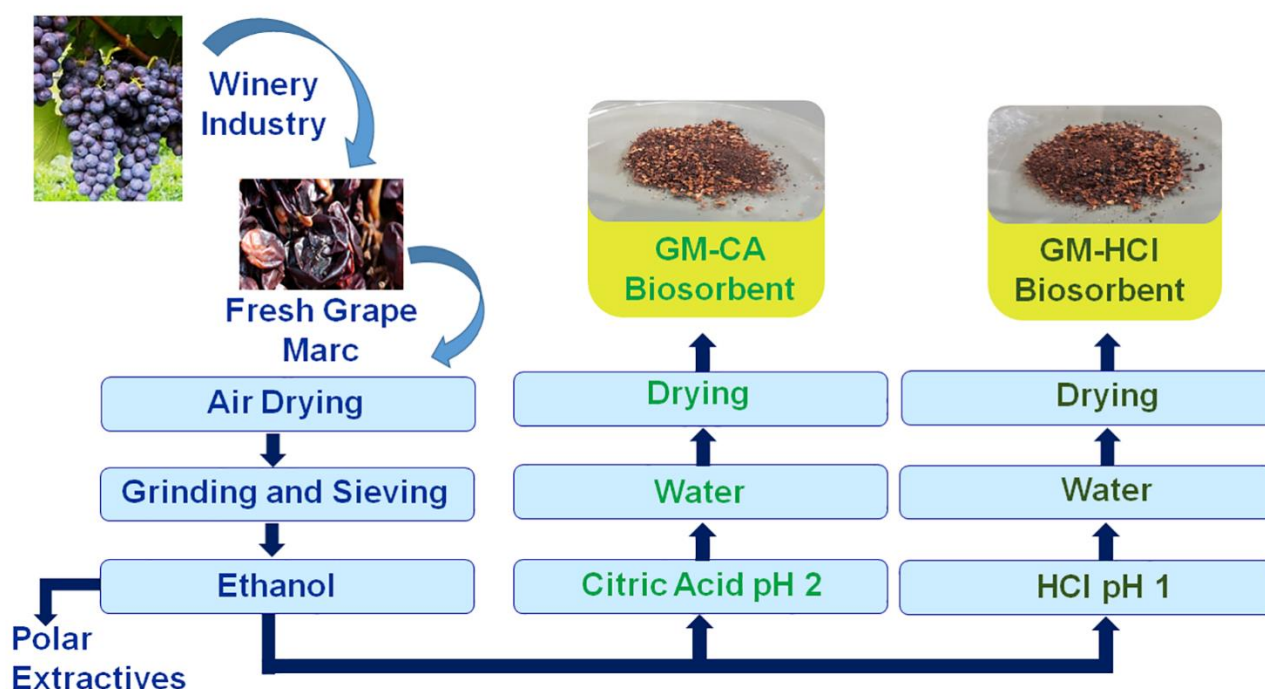
Figure 1. The experimental schematic preparation process of grape marc-based biosorbents.

pigments, and antioxidants [15]. Since phenolic compounds, pigments and antioxidants show absorption in the range of 280–800 nm; each ethanol washing solution was monitored using UV-vis analysis until almost no absorption was observed. Successively, a treatment with diluted acid was defined to remove some cations trapped inside it, leaving free coordination sites available for mercury cation uptake during the adsorption stage. It is known, in fact, the presence of some cations in grape marc matrices. Villaescusa *et al.* measured Ca(II), Mg(II), K(I), and Na(I) cations concentration from diluted HCl washing of grape marc waste and found mainly Ca(II) and K(I) ions released in solution [19]. In this study, this step was carried out by using a common and cheap acid HCl and also, as an alternative, a greener and inexpensive CA. Following Villaescusa *et al.* procedure, a preliminary washing with the 0.1 M (pH 1) HCl aqueous solution was used. Moreover, two other CA procedures at milder pH conditions (pH 3 and 2) were also tested. The washings were done till the concentration of cations (Ca^{2+}, Mg^{2+}, K$^+$, and Na$^+$) was lower than 1 mg L^{-1}. The adsorption capacity of biosorbents treated with each washing procedure was evaluated and biosorbent washed with CA at pH 3 gave lower adsorption capacity than grape marc treated with CA at pH 2. Thus, it was not considered for further studies.

Citric acid is an interesting alternative washing agent since it is also the main acidic compound of lemon fruit. Thus, the results of this research might be helpful as preliminary data for future studies that use lemon juice for the acidic washing steps of the grape marc, which is interesting from a green point of view. For the above consideration, a CA concentration with a pH close to lemon juice (close to pH 2) was used. Both biosorbents prepared with the different acids will be successfully tested as Hg(II) adsorption materials to verify the efficiency of the greener biosorbent GM-CA compared to GM-HCl.

Hg(II) adsorption isotherms

The adsorption behavior of both biosorbents was evaluated by batch experiments. The data were processed by Langmuir, Freundlich, Temkin, and D-R equations to assess their adsorption properties. This work aims to obtain a specific green biosorbent able to bind Hg(II) in a water solution with neutral pH, such as drinking water or tap water, to avoid additional pretreatments of the water sample before incubation. It is well known in the literature that the adsorption performances of similar matrices increase proportionally with the pH. Indeed, to obtain good adsorption results, pH in the range of 5–7 was required. In fact, under these conditions, the deprotonation of the acidic functional groups present in the modified biosorbent, such as lignin, increases the availability of active sites, favoring the electrostatic interactions between the metal ions and the surface of the biosorbent [11,12,19]. For this reason, HgCl$_2$ was directly dissolved in water with a pH of 7.

Adsorption experiments were done by shaking

3 mg of GM-HCl or GM-CA biosorbent with 3 mL of aqueous solutions of Hg(II) at known concentrations, from 23 to 300 mg L^{-1}. Adsorption equilibrium isotherms of GM-HCl and GM-CA are shown in Figure 2. Moreover, the concentrations of Ca^{2+}, Mg^{2+}, K$^+$, and Na$^+$ were monitored before and after mercury adsorption giving values lower than 0.5 mg L^{-1}, and no release can be assumed.
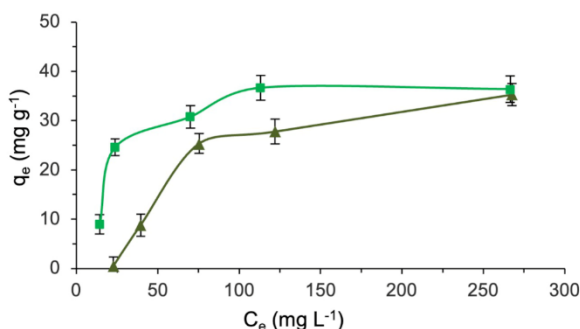
Figure 2. Adsorption capacity isotherm of Hg(II) using grape marc biosorbents GM-HCl (▲) and GM-CA (■).

As it can be seen, the graphics clearly show that the adsorption capacity increases with the increase of the analyte concentration until a saturation point is reached for both biosorbents. An experimental maximum adsorption capacity of 35.30 mg g^{-1} and 36.39 mg g^{-1} was obtained for the GM-HCl and GM-CA, respectively. Furthermore, it can be observed that the GM-CA curve has a sharper slop with qe values slightly higher than the corresponding qe values in the GM-HCl curve, with a plateau reached already at 150 mg L^{-1} of C_i. These results show that the acidic treatment helps obtain an efficient biosorbent for mercury removal by using CA under mild conditions, with a pH of around 2, similar to the pH of lemon juice. In Table S1 (supplementary materials), a comparison between the adsorption performances of GM-CA and GM-HCl against Hg(II) with other biosorbents from literature was reported.

In an attempt to verify the adsorption process starting from the experimental adsorption data, four different isotherms were used: Langmuir, Freundlich, Temkin, and D-R. Figures 3 and 4 show the isotherm linear regression curves obtained for GM-HCl and GM-CA biosorbents, respectively, while the significant isotherm parameters were summarized in Table S2.

Langmuir model describes homogeneous binding sites with a monolayer adsorption process only on the outer surface of the sorbent. This model assumes that the adsorption of each metal ion on the active sites takes place with uniform energies with no transmigration process of the adsorbates on the surface. In Figures 3a and 4a, the parameters $1/q_e$ versus $1/C_e$ were plotted. The obtained linear curves

showed R^2 values of 0.78 and 0.84, which are unsuitable for describing the adsorption process studied in this work.

On the contrary, the Freundlich isotherm adequately describes the adsorption on heterogeneous surface energy when monolayer adsorption occurs as in the Langmuir model but with a heterogeneous energetic distribution of the active sites and predicting interactions between the adsorbates metal ions. In Figures 3b and 4b, ln q_e versus ln C_e was plotted, and a bad agreement with the experimental data was found for both grape marc sorbents since regression coefficients lower than 0.73 were obtained.

The Temkin isotherm is generally suitable for a heterogeneous liquid and solid interface. This model assumes a linear decrease of heat adsorption of coverage rather than a logarithmic one predicted in the Freundlich model when the extremely low and high value of concentrations are excluded [22]. Temkin isotherm is characterized by a uniform binding energy distribution up to a maximum value. For this model, q_e versus ln C_e was plotted (Figures 3c and 4c), and the Langmuir, Freundlich, and Temkin parameters are compared in Table S2. The Temkin equation shows the highest regression coefficients, suggesting that this model best fits the adsorption curves for the applied biosorbents. Indeed, the corresponding B constants equal to 17.5 J mol^{-1} for the GM-HCl and 11.74 J mol^{-1} for the GM-CA are typical of physical adsorption.

Finally, the D-R model, which assumes a heterogeneous surface, was also used to test the experimental data to determine the mechanism of the adsorption process, plotting ln q_e versus ε^2. The model is generally successfully used with high solute activities and an intermediate range of concentrations. Linear curves with R^2 higher than 0.98 confirm the validity of this model. Moreover, a q_{max} of about 36 mg g^{-1}, very close to the experimental data, was obtained with energies E lower than 8 kJ mol^{-1}, typical of the physical adsorption mechanism [24]. In conclusion, the validity of the D-R model suggests a physical adsorption mechanism for both grape marc sorbents studied, following the results found in the previous Temkin isotherm model. The maximum adsorption capacities, calculated from DR-isotherm, were 35.71 mg g^{-1} and 36.41 mg g^{-1} for the GM-HCl and GM-CA, respectively, comparable to the values found in other similar biosorbents [12]. Therefore, it can be assumed that by using a greener citric acid instead of a common HCl (generally used for grape marc treatment) for acidic washing steps, biosorbents with similar adsorption performance were also obtained. Thus, from the adsorption isotherm studies, it can be concluded that citric acid is an attractive green alternative washing agent. Furthermore, the biosorbent prepared in this
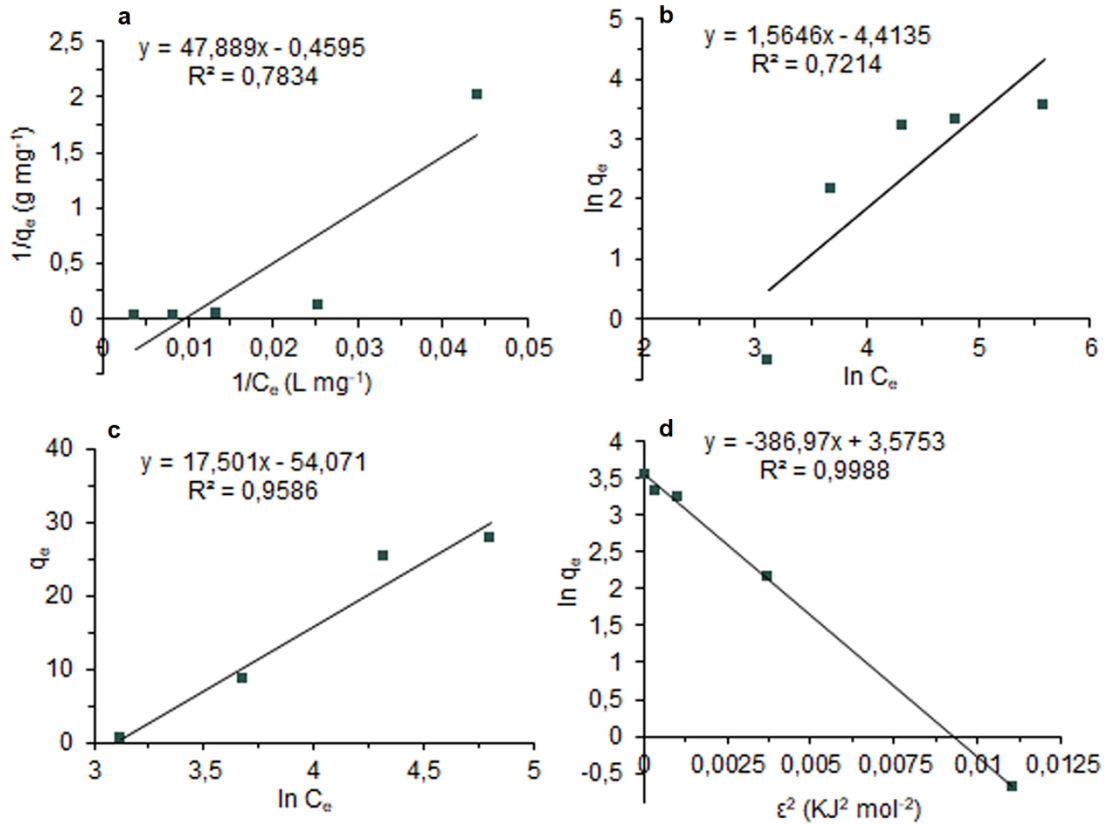
Figure 3. Langmuir (a), Freundlich (b), Temkin (c) and D-R (d) isotherms for adsorption of Hg(II) ions on GM-HCl.
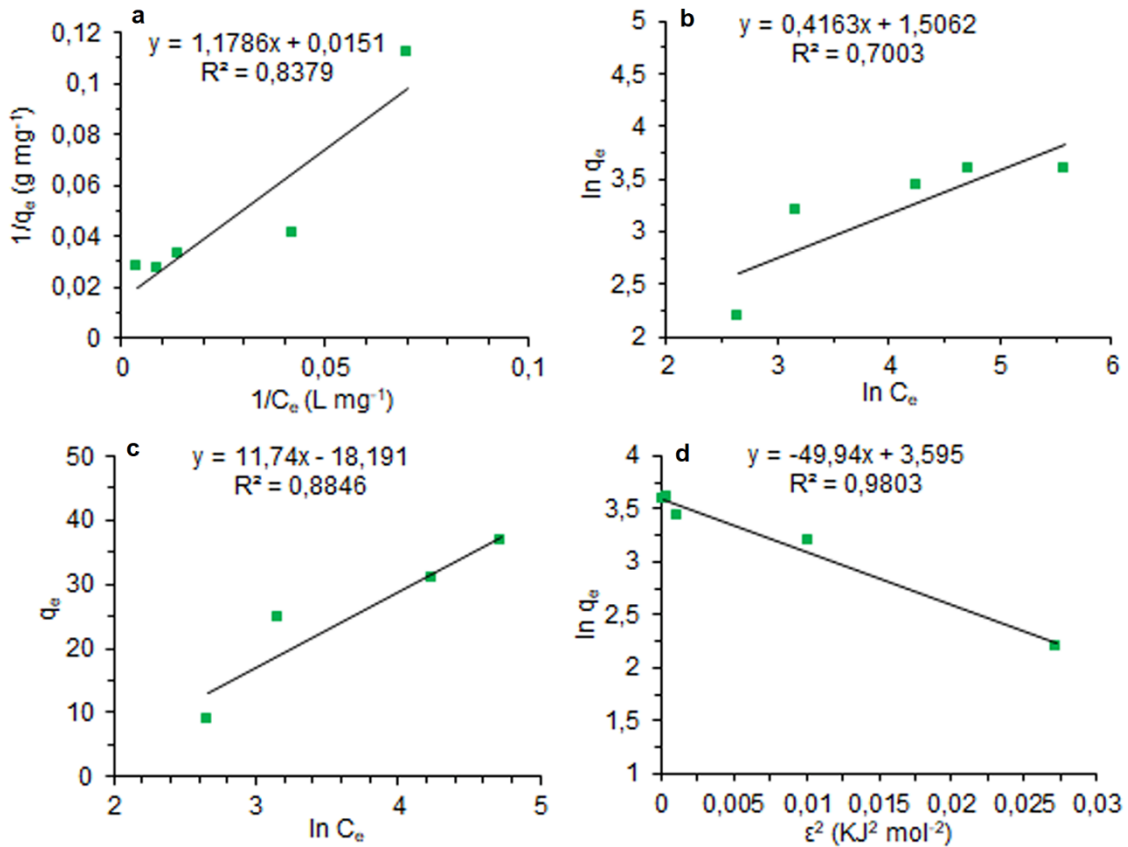
Figure 4. Langmuir (a), Freundlich (b), Temkin (c) and D-R (d) isotherms for adsorption of Hg(II) ions on GM-CA.

work using this solvent has interesting Hg(II) adsorption behavior with a physical adsorption mechanism. Therefore, only the biosorbent prepared with citric acid, GM-CA, was considered for further studies.

FTIR and kinetic study of GM-CA biosorbent

The FTIR spectrum of grape marc biosorbent treated with citric acid was analyzed to confirm Hg(II) adsorption on the matrix and assess the functional groups of the biomaterial involved in the uptake process. In Figure 5, the FTIR spectra of GM-CA before Hg(II) loading (Figure 5a) and after Hg(II) loading (Figure 5b) are shown. As can be seen in Figure 5a, some characteristic peaks of grape marc are due mainly to the lignocellulosic component [11]. In addition, the spectrum displays some absorption peaks, indicating the complex nature of the material analyzed. In detail, there is a broad band at 3419 cm^{-1} of the O-H stretching, the aliphatic C-H stretching peaks at 2918 cm^{-1} and 2850 cm^{-1}, and a peak at 1733 cm^{-1} for C=O stretching, typical of unconjugated carbonyl groups. Moreover, the peaks of the C=N (1623 cm^{-1}), C=C stretching of aromatic rings (1556 cm^{-1} and 1518 cm^{-1}), and aliphatic C-H bending (1456 cm^{-1} and 1436 cm^{-1}) are also observed [12,25,26]. In Figure 5b, some of the signals present in Figure 5a are slightly modified in terms of shape, intensity, or wavenumber due to mercury interaction. In detail, as can be observed in Figure 5b, the modified signals (highlighted in the circles) after the Hg(II) uptake are related to the O-H stretching (3410 cm^{-1}), C=N stretching (between 1658 cm^{-1} and 1611 cm^{-1}), C=C stretching (between 1546 cm^{-1} and 1513 cm^{-1}), and aliphatic C-H bending (around 1452 cm^{-1}). Thus, we suppose that the interaction of the Hg(II) involves mainly the lignocellulosic part, which is the main component of the biosorbent.
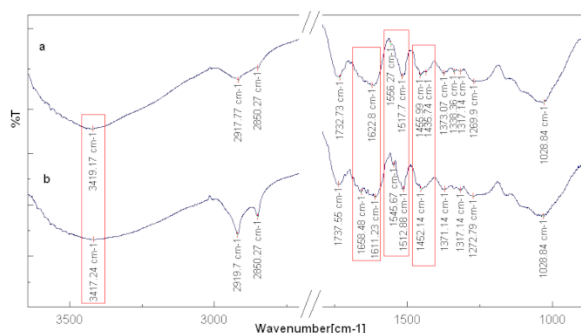
Figure 5. FTIR spectra of biosorbent GM-CA before Hg(II) ions loading (a) and after Hg(II) loading (b).

Further, the GM-CA biosorbent was evaluated by studying the Hg(II) adsorption kinetics. First, a Hg(II) solution of 78 mg L^{-1} was used to incubate the GM-CA biosorbent. Then, ICP measurements of the Hg(II) concentration at different times were registered, and

8

the corresponding Hg(II) amount adsorbed at time t, q_t (mg g^{-1}), was plotted against the time in Figure 6. The plateau phase was reached within 7 h of incubation. However, it is worth noting that in the first 60 min, almost 50% of the equilibrium Hg(II) amount is adsorbed (10.81 mg g^{-1}, 48%).
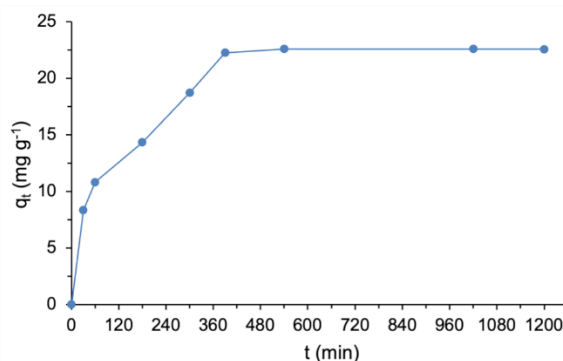
Figure 6. Adsorption kinetic curve of GM-CA with Hg(II) ions aqueous solution (78 mg L^{-1}).

Pseudo-first order and pseudo-second-order models were considered to fit the kinetic data (Figure 7). The corresponding kinetic parameters are summarized in Table S3. The pseudo-first-order equation assumes that one adsorbate ion adsorbs within one active site of the biosorbent. On the contrary, the pseudo-second-order model assumes that one adsorbate ion is linked with two active sites of the biosorbent [27]. Based on the correlation coefficient value of ($R^2 = 0.994$), the experimental data followed the second order kinetics (Figure 7b), with an adsorption rate constant K_2 of 7.67x10^{-4} (g mg^{-1} min^{-1}). The theoretical q_e value estimated from the pseudo-second-order kinetic model was 23.75 mg g^{-1}, similar to the experimental value obtained at an initial Hg(II) concentration of about 78 mg L^{-1}. On the contrary, the pseudo-first-order kinetic equation (Figure 7a) showed a correlation coefficient of 0.9300 with an estimated q_e value of 3.852 mg g^{-1}, significantly lower than the experimental one, resulting in a bad model to define the kinetics of the adsorption on the sorbent.

Comparative adsorption study and reusability

Finally, the behavior of the GM-CA biosorbent was tested by evaluating its adsorption capacity for two other divalent metal ions and its reusability. In previous works, the Cu(II) and Ni(II) adsorption capacities of about 10 mg g^{-1} have been found for similar biosorbents have been studied [19,20]. The adsorption experiments using Cu(II) and Ni (II) salts showed an adsorption capacity of 100 mg L^{-1}. For Cu(II) and Ni(II), the differences in the concentrations measured before and after incubation were statistically insignificant. It is worth noting that different behavior is found in the
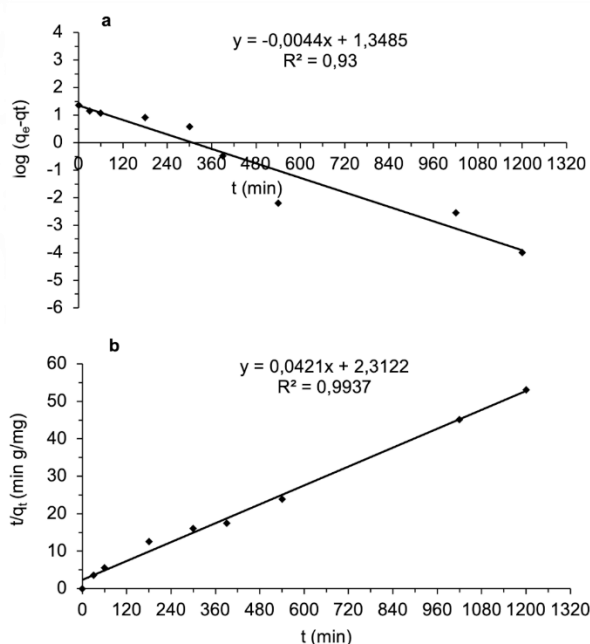
Figure 7. Adsorption kinetics of Hg(II) ions on the GM-CA grape marc-based biosorbent evaluated by the pseudo-first-order model (a) and pseudo-second-order model (b).

literature for similar matrices [20]. These results can be justified by considering the complex structure typical of the grape biomaterial and the different compositions of each grape variety, in addition to the modification of its structure during the biosorbent preparation steps.

After an adsorption experiment using the GM-CA and a Hg(II) aqueous solution of 100 mg L^{-1}, the mixture was centrifuged to separate the grape-marc-based biomaterial, which was then treated with an acidic aqueous solution to desorb Hg(II) ions. For this purpose, a solution of HCl or citric acid was used at the same concentration for biosorbent regeneration and reuse. The regenerated biomaterial was reused for another adsorption experiment. The regeneration efficiency for three successive adsorption/desorption experiments was higher than 93% for both treatments. Thus, the regenerated biomaterial showed similar adsorption capacities at least for three cycles.

CONCLUSION

In this work, two green grape marc-based biosorbents obtained from wastes of Negroamaro wine production were prepared and successfully used for the adsorption of Hg(II) ions in neutral aqueous solutions. A green approach adopted in the biosorbents preparation process allowed the positive evaluation of green chemicals, such as water, ethanol, and citric acid. In fact, from the adsorption isotherm study, the GM-CA biosorbent, prepared using citric acid, showed a maximum adsorption capacity of 36.39 mg g^{-1} with a

physical adsorption mechanism of Hg(II) on the matrix. Further, GM-CA was chemically characterized by FTIR, demonstrating the interactions of the Hg(II) with the lignocellulosic component of the grape marc.

Herein for the first time, the adsorption capacity of Hg(II) was demonstrated for a green and cheap grape marc-based biosorbent, and its selectivity, compared to other bivalent ions Cu(II) and Ni(II), was proven as well. Furthermore, the biosorbent developed in this study shows a specific adsorption behavior characteristic of the grape variety and the preparation process. Finally, it is worth noting that these results can help promise future studies to prepare innovative green adsorbents to remove Hg(II) ions from drinking water.

REFERENCES

[1]   WHO, Inorganic mercury - environmental health criteria 118. World Health Organization, International Programme on Chemical Safety, Geneva, Switzerland, 1991. https://apps.who.int/iris/bitstream/handle/10665/40626/IPCS_EHC_118.pdf?sequence=1

[2]   J.G. Wiener, D.P. Krabbenhoft, G.H. Heinz, A.M. Scheuhammer, Ecotoxicology of mercury. In: Handbook of Ecotoxicology, Hoffman D. J., Rattner B. A., Burton G. A., Cairns J. (Eds), 2nd Ed., Lewis Publishers, Boca Raton (2003), pp 409–463. https://doi.org/10.1201/9781420032505.ch16

[3]   B. Fernandes Azevedo, L. Barros Furieri, F.M. Peçanha, G. A. Wiggers, P. Frizera Vassallo, M. Ronacher Simões, J. Fiorim, P. Rossi de Batista, M. Fioresi, L. Rossoni, L. Stefanon, M.J. Alonso, M. Salaices, D. Valentim Vassallo, J. Biomed. Biotechnol. 2012 (2012) 949048. https://doi.org/10.1155/2012/949048

[4]   D.M. Manohar, K.A. Krishnan, T.S. Anirudhan, Water Res. 36 (2002) 1609–1619. https://doi.org/10.1016/S0043-1354(01)00362-1

[5]   X. Lu, X. Huangfu, J. Ma, J. Hazard. Mater. 280 (2014) 71–78. https://doi.org/10.1016/j.jhazmat.2014.07.056

[6]   M.A. Didi, B. Medjahed, W. Benaoudam, Am. J. Anal. Chem. (2013) 40–47. https://doi.org/10.4236/ajac.2013.47A006

[7]   L. Mergola, S. Scorrano, E. Bloise, M.P. Di Bello, M. Catalano, G. Vasapollo, R. Del Sole, Polym. J. 48 (2016) 73–79. https://doi.org/10.1038/pj.2015.79

[8]   M.W. Franco, L.A. Mendes, C.C Windmöller., K.A.F Moura., L.A.G. Oliveira, F.A.R. Barbosa, Water Air Soil Pollut. 229 (2018) 127. https://doi.org/10.1007/s11270-018-3782-5

[9]   A. Bhatnagar, M. Sillanpää, A. Witek-Krowiak, Chem. Eng. J., 270 (2015) 244–271. https://doi.org/10.1016/j.cej.2015.01.135

[10]   M. Erhayem, F. Al-Tohami, R. Mohamed, K. Ahmida, Am. J. Anal. Chem. 6 (2015) 1–10. https://doi.org/10.4236/ajac.2015.61001

[11]   F.E. Arias Arias, A. Beneduci, F. Chidichimo, E. Furia, S. Straface, Chemosphere. 180 (2017) 11–23. https://doi.org/10.1016/j.chemosphere.2017.03.137

[12]   N.M. Mora Alvarez, J.M. Pastrana, Y. Lagos, J.J. Lozada, Sustain. Chem. Pharm. 10 (2018) 60–70. https://doi.org/10.1016/j.scp.2018.09.004

[13] J. Aurand,2018 OIV statistical report on world vitiviniculture 2018 world vitiviniculture situation. http://www.oiv.int/public/medias/6371/oiv-statistical-report-on-world-vitiviniculture-2018.pdf (accessed 3 March 2020).

[14] M. A. Bustamante, R. Moral, C. Paredes, A. Pérez-Espinosa, J. Moreno-Caselles, M.D. Pérez-Murcia, Waste Manag. 28 (2008) 372–380. https://doi.org/10.1016/j.wasman.2007.01.013

[15] R.A. Mulhack, R. Potumarthi, D.W. Jeffery, Waste Manag. 72 (2018) 99–118. https://doi.org/10.1016/j.wasman.2017.11.011

[16] M.S Rodríguez-Cruz., E. Herrero-Hernández, J.M. Ordax, J.M. Marín-Benito, K. Draoui, M.J. Sánchez-Martín, Int. J. Environ. Anal. Chem. 92 (2012) 933–948. https://doi.org/10.1080/03067319.2011.609933

[17] R. Portinho, O. Zanella, L.A. Féris, Grape stalk application for caffeine removal through adsorption. J. Environ. Manage. 202 (2017) 178–187. https://doi.org/10.1016/j.jenvman.2017.07.033

[18] V. Grudić, J. Šćepanović, I. Bošković, 2015 Chem. Ind. Chem. Eng. Q. 21(2015) 285–293. https://doi.org/10.2298/CICEQ140418027G

[19] I. Villaescusa, N. Fiol, M. Martínez, N. Miralles, J. Poch, J. Serarols, Water Res. 38 (2004) 992–1002. https://doi.org/10.1016/j.watres.2003.10.040

[20] C. Liu, D. Pujol, N. Fiol, M.À. Olivella, F. de la Torre, J. Poch, I. Villaescusa, Water Air Soil Pollut. 226 (2015) 2006.

[21] https://doi.org/10.1007/s11270-014-2006-x R. Chand, K. Narimura, H. Kawakita, K. Ohto, T. Watari, K. Inoue, J. Hazard. Mater. 163 (2009) 245–2502. https://doi.org/10.1016/j.jhazmat.2008.06.084

[22] A.O. Dada, A.P. Olalekan, A.M. Olatunya, O. Dada, IOSR-JAC. 3 (2012) 38–45. https://doi.org/10.9790%2F5736-0313845

[23] M.P. Di Bello, L. Mergola, S. Scorrano, R. Del Sole, Polym. Int. 66 (2017) 1055–1063. https://doi.org/10.3390/ma10101133

[24] V.B.H. Dang, H.D. Doan, T. Dang-Vu, A. Lohi, Bioresour. Technol. 100 (2009) 211–219. https://doi.org/10.1016/j.biortech.2008.05.031

[25] F. Lionetto, R. Del Sole, D. Cannoletta, G. Vasapollo, A. Maffezzoli, Materials 5 (2012) 1910–1922. https://doi.org/10.3390/ma5101910

[26] S. Zmora-Nahuma, Y. Hadarb, Y. Soil Biol Biochem, 39 (2007) 1263–1276. https://doi.org/10.1016/j.soilbio.2006.12.017

[27] N. Naowanat, N. Thouchprasitchai, S. Pongstabodee, J. Environ. Manage. 169 (2016) 103–115. https://doi.org/10.1016/j.jenvman.2015.12.024

ROBERTA DEL SOLE
ALVARO MAGGIO
LUCIA MERGOLA

[1]Department of Engineering for Innovation, University of Salento, Lecce, Italy

DOBIJANJE BIOSORBENTA OD KOMINE GROŽĐA ZA UKLANJANJE ŽIVE IZ VODENIH MEDIJIMA

Otpadna komina iz vinarije Negroamaro (sorta vinove loze južne Italije) korišćen je za pripremu biosorbenata za uklanjanje Hg(II) u vodenoj sredini. Za razvoj odgovarajućeg biosorbenta korišćena su dva različita "zelena" postupka isipranja komine grožđa. Posebno su procenjene obična hlorovodonična kiselina i "zelenija" limunska kiselina. Biosorbent pripremljen korišćenjem limunske kiseline kao sredstva za ispiranje (GM-CA) dao je slične rezultate kao biosorbent ispran sa hlorovodoničnom kiselinom (GM-HCl) sa maksimalnim kapacitetom adsorpcije od 36,39 mg g⁻¹. Na osnovu izotermi otkrivena je heterogena fizička adsorpcija Hg(II) na biosorbentima. Štaviše, FTIR analiza biosorbenta na bazi komine grožđa bez i sa adsorbovanom Hg(II) potvrdila je jonske interakcije u biosorbentu koje se uklapaju u kinetički model pseudo-drugog reda. Takođe, nije primećena značajna adsorpcija na biosorbentu kada su razmatrana dva druga teška metala, bakar(II) i nikl(II), koji su prethodno adsorbovani na sličnim sorbentima. Konačno, ponovna upotreba GM-CA biosorbenta je, takođe, demonstrirana tokom tri ciklusa. Dakle, korišćeni pristup "zelene" pripreme može se smatrati pogodnim za razvoj biosorbenata na bazi komine grožđa.

Ključne reči: adsorpcione izoterme, limunska kiselina, uklanjanje Hg(II), komina grožđa, zeleni biosorbent od otpada, kinetička studija.

NAUČNI RAD

NAFEES AHMED[1]
MD. YASIN HOSSAIN[1]
JOYANTA KUMAR SAHA[1]
MOHAMMAD AL MAMUN[1,2]
A. K. M. LUTFOR RAHMAN[1]
JAMAL UDDIN[3]
ABDUL AWAL[1]
MD. SHAJAHAN[1]

[1]Department of Chemistry, Jagannath University, Dhaka, Bangladesh

[2]Nanotechnology and Catalysis Research Centre, Institute of Advanced Studies, University of Malaya, Kuala Lumpur, Malaysia

[3]Center for Nanotechnology, Chemistry, and Nanotechnology, Department of Natural Sciences, Coppin State University, Science and Technology Center, Baltimore, USA

ADSORPTIVE REMOVAL OF CRYSTAL VIOLET DYE FROM AQUEOUS SOLUTION ONTO COCONUT COIR

Article Highlights
- The dependence of pH on the adsorption mechanism of crystal violet on coconut coir was revealed
- The superiority of coconut coir in removing crystal violet from an aqueous solution was illuminated
- UT-CC and SCT-CC showed comparable removal capacity against crystal violet (CV) at high pH (8.00)
- The proposed adsorption mechanism of CV onto coconut coir was interpreted by FTIR data
- The DFT simulation revealed the interaction between CV and lignin in CC as chemisorption

Abstract

The untreated and sodium chlorite-treated coconut coir was implemented to remove crystal violet (CV) dye from an aqueous solution by batch adsorption experiments. The adsorption capacity, equilibrium time, and adsorption kinetics of CV on both adsorbents were regulated by the pH of the dye solution. High pH favors the comparative adsorption capacity for both adsorbents. In contrast, the untreated coconut coir (UT-CC) shows higher adsorption efficiency ($9.61 \ mg \ g^{-1}$) than sodium chlorite-treated coconut coir (SCT-CC) at low pH. At lower pH (2.00), the equilibrium was established within 60 min by both adsorbents. However, the quick attainment of the equilibrium (30 min) was observed using both the adsorbents at higher pH (8.00). The isotherm data for both the adsorbents was found to have better agreement with the Freundlich than the Langmuir model at pH 8.00. The kinetic data was well-fitted with Ho's pseudo-second-order model. Both adsorbents were characterized by FTIR and SEM to get evidence for the proposed adsorption mechanism. Density functional theory (DFT) also supports this result which illustrates the adsorption of CV on lignin of CC with the adsorption energy -51.16 kJ/mol at the B3LYP/6-31(d,p) level of theory.

Keywords: coconut coir, sodium chlorite, crystal violet, adsorption kinetics, adsorption mechanism, density functional theory.

The aquatic ecosystem is disturbed due to the interference in the penetration of light into the water and the degradation of the aesthetic value of water bodies caused by the color effluents discharged from dyeing industries [1]. Carcinogenic and mutagenic dyes and pigments [2,3] are toxic that affect aquatic biota and humans [4]. It is difficult to degrade the dyes under natural conditions; therefore, the conventional wastewater treatment systems are not effective in typically removing these dyes. Dye effluents are currently treated by several physical or chemical techniques, such as microbial degradation, flocculation [5,6], membrane separation [7], ultra-chemical filtration [8], chemical oxidation, bioaccumulation, electrochemical treatment, adsorption, and reverse osmosis [9]. The wide range of dye-containing wastewater cannot be treated using most of these

techniques because of being costly and time-consuming. Moreover, dye biodegradation may produce by-products and/or other metabolites with higher toxicity than the primary substrate [10]. Other conventional techniques, such as coagulation and flocculation, do not help remove dyes from the water-introduced metallic impurities producing a large amount of sludge that requires further disposal.

Adsorption is one of the promising techniques for removing hazardous and environmentally undesirable chemicals [11]. Adsorption is generally chosen owing to easy handling, high efficiency, low energy input, and availability of different adsorbents [12,13]. Activated carbon from various sources (e.g., *Ricinuscommunis pericarp* [14]) is the most widely used adsorbent in removing the dye staff. However, it is not economically feasible. Therefore, low-cost and easily available bioadsrobents are usually used to remove dye staff in place of activated carbon at different operating conditions.

CV, a cationic textile dye, is an enhancer of bloody red fingerprints. It is applied to manufacture paints and printing inks [15]. Crystal violet is also used for preventing fungal growth in poultry feed [16,17]. In addition, skin infections by *Staphylococcus aureus* can be treated by CV [18,19]. However, crystal violet is carcinogenic like other textile dyes. Furthermore, it is classified as an intractable molecule since it is poorly metabolized by microbes, non-biodegradable, and can persist in various environments. Scientists have already investigated the removal of CV from the

wastewater by using different adsorbents, such as sugarcane bagasse [20], some waste materials, i.e., bottom ash [21], powdered mycelial biomass of *Ceriporialacerata* P2 (CLB) [22]. So far, to the authors' knowledge, coconut coir, an environment-friendly bioadsorbent, has not been used to remove CV from the wastewater.

Therefore, low-cost and easily available coconut coir was used to remove CV from an aqueous solution. Coconut coir (as in dust, coir, or pith form) has been previously used to remove different dyes, such as malachite green [23], methylene blue, and remazol yellow [24]. But coconut coir, either raw or treated, has not been used to remove CV from the wastewater. Therefore, the present study not only portrayed the removal of CV from an aqueous solution using untreated coconut coir (UT-CC) and sodium chlorite-treated coconut coir (SCT-CC) but also shed light on the adsorption mechanism.

MATERIAL AND METHODS

All chemicals were reagent grade. CV was obtained from Scharlau Chemicals, Spain. All the experimentation solutions were prepared by diluting stock solution. The preparation and dilution of CV solution were done with Distilled Deionized Water (DDW). The chemical specifications for CV are mentioned in Table 1.

The adsorbents employed in this research were

Table 1. . Chemical Specification for CV*

Crysta

Crystal violet, C.I. 42555		
VI0025	Crystal violet, C.I. 42555, indicator, extra pure	

Synonyms: Hexamethylenepararosaniline chloride, Hexamethyl-p-rosanilinium chloride, Methyl violet 10 B
$C_{25}H_{30}ClN_3$
M = 407,99 g/mol
CAS [548-62-9]
EINECS-No.: 208-953-6
Solub. in water: (20 ºC): 10 g/l
Melting point: 189 - 194 ºC
LD 50 (oral, rat): 420 mg/kg
ADR: 9 M7 III UN 3077
IMDG: 9 III UN 3077
IATA/ICAO: 9 III UN 3077
GHS-signal word: Danger
GHS-H sentences: H318 - H351 - H410 - H302
GHS-P sentences: P280 - P281 - P305 + P351 + P338 - P310 - P405 - P501a
Tariff number: 3204 13 00 90

Applications: analytical chemistry, microscopy, indicator.

Specifications:
dye content
(spectrophotometric) . . . . .min. 85 %
Absorption maximum λ max (in H_2O) . . . 589 - 594 nm
Absorptivity (A 1%/1 cm;
(λ max; 0,002 g/l; H_2O). . . . . 2000 - 2450
loss on drying . . . . max. 10 %
suitability as indicator in
TLC test . . . . .passes test
non-aqueous solvents . . . . .passes test

Art. No.	Volume	Container
VI00250025	25 g	
VI00250100	100 g	

+Chemicals and Reagents Index (page 150): Scharlau Chemicals, Spain (scharlab@scharlab.com)

UT-CC, i.e., raw coconut coir, and SCT-CC. The former was collected from the local market, whereas the latter

was obtained by treating the raw coir with sodium chlorite (80% NaClO₂, BDH laboratory, England).

Furthermore, instruments including a pH meter (Yangzhong SHI YIBIAO QIJIAN CHANG), a combination electrode with a precession of ±0.01 pH units, and a UV-visible Spectrometer (OPTIZEN, Korea), were employed for measurement of pH and concentration of dye solution, respectively. In addition, scanning electron microscopic (SEM) analysis of the adsorbents was done with the help of an SEM -JEOL JSM 7600F electron microscope (JEOL, USA), while the recording of the IR spectrum of coconut coir was done with FT-IR Spectrometer [Model: Frontier FT-NIR/MIR] (Perkin Elmer, USA).

The raw fiber collected from the local market was washed with tap water followed by distilled water several times to remove dust and pigments. The washed fiber was sun-dried and then heated in an oven at 110 °C. The dried fiber was ground by a mechanical grinder and screened out to the desired mesh size using sieves of 150 and 300 μm BSS mesh. The fiber, termed UT-CC, was kept in a desiccator until use.

The UT-CC was treated according to Box-Behnken's experimental design [25]. In this case, 6.2 g of NaClO$_2$ was dissolved in distilled water in a three-neck flask, followed by adding 9.5 mL of acetic acid (99%) and stirring for about 60 min at 90 °C after adding 10 g of UT-CC. The treated coconut coir (SCT-CC) was washed thoroughly with distilled water until the filtrate reached pH at the neutral point, then dried the coir at 70 °C to a constant weight, screened through a sieve, and kept in desiccators for further use.

Preliminary investigations of the CV adsorption (equilibrium time and adsorption isotherm) onto UT-CC and SCT-CC helped select the optimum concentration and pH. The batch adsorption studies were carried out at three different pH values, 2.00, 7.00, and 8.00, by taking 40 mL of the dye solutions (100 mg/L) in a 250 mL reagent bottle and adding the adsorbents of selected mesh size (150–300 μm BSS) in the appropriate dosage (0.3 g) at room temperature (28.0±0.5 °C). These dye solutions were shaken for a specific time at the desired speed. The adsorbent dose, contact time, and temperature during adsorption were carefully controlled. After centrifugation, the concentration of the dye solution was analyzed by a UV-Visible spectrophotometer (OPTIZEN, Korea). Absorptions were measured at the wavelengths of 590 nm for pH 7.00/8.00 and 625 nm for pH 2.00. These experiments were carried out with different dye concentrations ranging from 40–150 mg/L.

Kinetic measurements were made by taking 40 mL of the dye solutions in 250 mL reagent bottles and adding 0.3 g adsorbent (UT-CC or SCT-CC) for each run. The solutions were shaken at regular intervals, and after centrifugation, the supernatant liquid was analyzed by a UV-visible spectrophotometer. Dye uptake was calculated from the concentration change of the dye solution before and after adsorption. For the kinetic studies, dye adsorption experiments were conducted at three different pH values, i.e., 2.00, 7.00, and 8.00.

FTIR spectra of the samples were recorded on a Frontier FT-NIR/MIR (Perkin Elmer, USA) spectrometer using potassium bromide pellets. The surface morphologies were determined using SEM (JSM 5600 LV, JEOL, USA) instrument with gold film.

RESULTS AND DISCUSSION

Adsorbent characterization

FTIR analysis of adsorbents

Coconut coir is composed of cellulose, hemicellulose, and lignin. FTIR analysis of the bare surface was carried out to know the surface functional groups. The investigated FTIR spectra of raw and treated fiber are shown in Figure 1. It was observed that the surface contained alcoholic (-OH) group [3449.7 cm^{-1}], carbon-hydrogen bond {-C-H (stretch} in alkane [2934 cm^{-1}], carbon-hydrogen bond {-C-H (stretch} in aldehyde group (-CHO) [2850.3 cm^{-1}], carbon-carbon double bond (>C=C<) [1602.9 cm^{-1}] and ethereal group (-O-) [1237.5 cm^{-1}] [26]. According to the previous report, the oxidation of lignin was rendered by chlorine dioxide produced by NaClO$_2$ after treating the fiber under acidic conditions [27]. The broadband at about 3397 cm^{-1} attributed to the stretching vibration of −OH in cellulose became broader after treatment, possibly due to part of hydrogen bonds and lignin being broken [25]. This information indicated that the treatment broke lignin in the coconut coir.
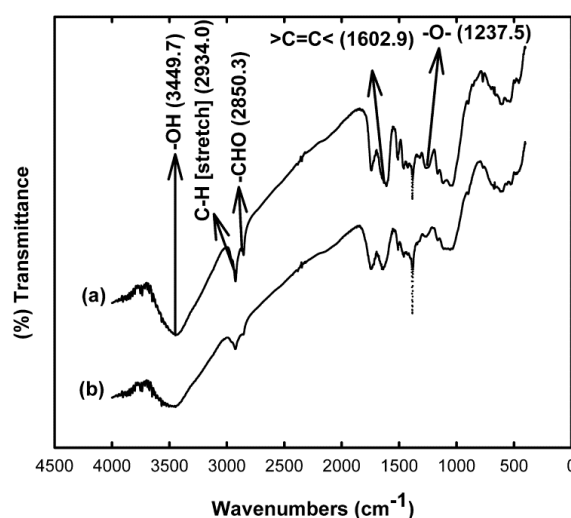
Figure 1. FTIR spectra of (a) UT-CC and (b) SCT-CC.

SEM Analysis

SEM micrographs of UT-CC and SCT-CC are shown in Figure 2. The tube-like shape for UT-CC was observed in Figure 2(a). The shape of the coir remained unchanged after being treated with NaClO$_2$ (Figure 2(b)). However, some porous structures were observed after the treatment, indicating the treatment altered the surface morphology of coconut coir fiber. The result was dissimilar to the previously published article on kapok fiber [25]. SEM photographs revealed the porosity and adsorptive nature of coconut coir. Due to the evolution of the porous site, the surface of SCT-CC became more conducive for the dye molecule to adsorb onto it rather than UT-CC. The porous morphology of SCT-CC observed in the SEM image was justified by the BET analysis shown in Table 2. EDS analysis shown the elementary composition of SCT-CC (Table 3).
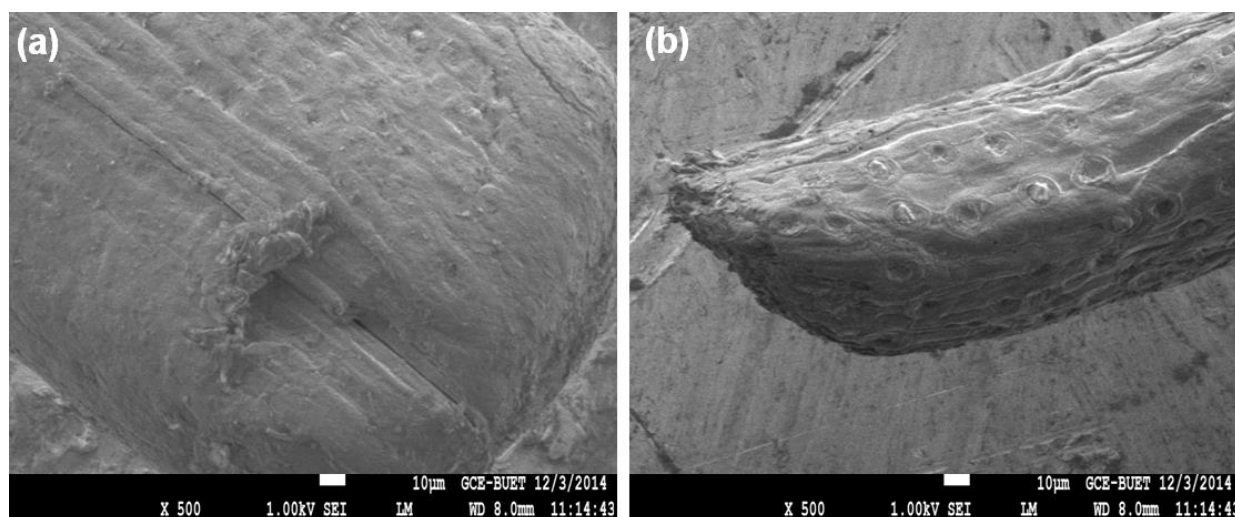
Figure 2. SEM micrographs of (a) UT-CC and (b) SCT-CC x 500 magnification.

Table 2. Summary of BET results of sodium chlorite treated coconut coir (SCT-CC)

Parameters	SCT-CC
BET-specific surface area (m^2/g)	6.48
Total pore volume (cc/g)	0.0652
Skeletal density (g/cc)	2.2845
Porosity based on skeletal density (per gram of sample)	0.1297
Average pore diameter (Å)	402.2296

Table 3. The elementary composition of SCT-CC obtained from EDS analysis

ZAF Method Standardless Quantitative Analysis

Fitting Coefficient : 0.0424

Element	(keV)	Mass %	Sigma	Atom %	K
C K	0.277	52.17	0.19	59.86	51.5228
O K	0.525	45.35	0.36	39.06	44.0002
Na K	1.041	0.25	0.03	0.15	0.2975
Si K	1.739	0.54	0.03	0.27	0.8945
Cl K	2.621	1.69	0.05	0.66	3.2850
Total		100.0		100.0	

Adsorption studies

Equilibrium time

The adsorption studies were carried out with UT-CC and SCT-CC at different pH values. The adsorption process was rapid and reached equilibrium within 60 min for both the adsorbents at pH 2.00 (Figure 3(a)).

However, the attainment of the equilibrium adsorption was found to be somewhat faster (30 min) at high pHvalues for both the adsorbents (Figure 3(b)). Experiments at low pH using SCT-CC showed gradual adsorption of CV up to equilibrium, revealing that the surface's active site became porous after treatment. On the other hand, the discontinuous adsorption phenomenon was observed with UT-CC because of the absence of such an active porous site.

Factors affecting the amount adsorbed

The amount adsorbed of CV was affected by several factors, such as adsorbents, the pH of the adsorbate solution, and the initial concentration of the adsorbate solution. A significant difference in the removal capacity of CV for both adsorbents, e.g., UT-CC and SCT-CC, is depicted in Figure 3(a). It shows that UT-CC (9.61 mg g^{-1}) is a better adsorbent than SCT-CC (1.01 mg g^{-1}) for the adsorption of CV at pH 2.00. However, both the adsorbents were found to

have comparable adsorption capacity at pH 8.00 (12.45 mg g^{-1} and 13.54 mg g^{-1} for UT-CC and SCT-CC, respectively).

The value of pH has a pronounced effect on surface phenomena. Adsorption of the dye was dependent on the pH of the adsorbate solution. The tests at different pH values (from 2.00 to 8.00) at an initial dye concentration of 100 mg/L determined the suitable pH for adsorption. In the present work, it was proved experimentally that the change in pH from lower to higher (2.00 to 8.00) caused the increase in the effective removal of CV by adsorption on both the adsorbents (UT-CC: 96.48%, and SCT-CC: 98.26%). It was found that the amount adsorbed (q_t) was lower at lower pH than the higher pH for both UT-CC and SCT-CC depicted in Figure 3(a). But the adsorption capability and the rate of adsorption pronouncedly
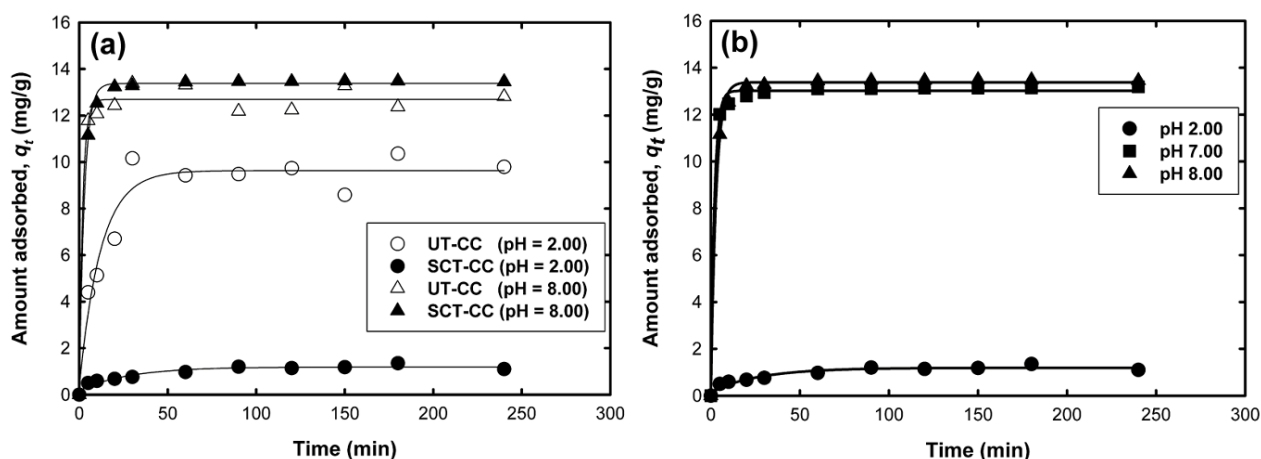
Figure 3. (a) Amount of CV adsorbed per gram of UT-CC and SCT-CC at pH 2.00 and 8.00 at room temperature (28±0.5 °C); (b) Amount of CV adsorbed per gram of SCT-CC at different pH values at room temperature (28±0.5 °C).

increased for SCT-CC at higher pH conditions. The variation of amount adsorbed (q_t) and equilibrium adsorbed amount (q_e) with pH for SCT-CC were shown in Figure 3(b) and Figure 4(a). Here both the amount adsorbed increases with increasing pH values. Since CV carries a positive charge on the nitrogen atom, the surface becomes positive at lower pH and generates a repulsive force between the adsorbate and the surface. But as the pH was increased to higher values, the surface became negatively charged, and CV felt the electrostatic force of attraction towards the surface. As a result, the amount adsorbed increased optimistically. It was reported that as pH increased, the dye solution's charge density decreased. Hence, the electrostatic repulsion between the positively charged dye molecule and the surface of the adsorbent lowered and increased dye sorption [28]. Similar results were also reported on

the adsorption of crystal violet by R. Ahmad (2009) [29].

Variation of the equilibrium amount of CV adsorbed per gram of SCT-CC at different pH values is depicted in Figure 4(a). The equilibrium adsorbed amount of CV increases with the pH from 2.00 to 8.00, and almost saturation arises at a pH higher than 7.00. A similar result was observed by using magnetic activated carbon [30]. However, similar findings were obtained for the adsorption of CV onto SDS-modified MNPs, where the adsorption efficiency decreased with an increase in the pH above pH$_{zpc}$ [31]. The experimental results also indicate that the rate of adsorption of CV onto SCT-CC increases with increasing pH, which agrees with the result published by A. L. Prasad and T. Shanti, 2012 [32]. According to them, the adsorption capacity and rate constant tend to increase as the initial pH of the solution increases due

to the pH_{zpc} of the adsorbents, which has an acidic value favorable for cation adsorption [32].

The pronounced effect of the equilibrium amount adsorbed was obtained by varying initial dye concentration for both the adsorbents. Adsorption experiments for both adsorbents were carried out at room temperature (28±0.5 °C) with an adsorbent dosage of 0.3 g in a concentration range of 40 to 150 mg/L. An increase in the concentration led to a rise in the amount of the adsorbed dye. This increase in adsorption with dye concentration is attributed to the retardation of resistance toward dye uptake, which increases the diffusion of the dye (Figure 4(b)). Figure 4(b) shows that the maximum adsorption of CV onto UT-CC is achieved at 150 ppm, whereas in the case of SCT-CC, the uptake increases further if the initial concentration of CV has been increased much. This finding can be compared with the results obtained from the removal of CV using a surfactant-modified magnetic nanoadsorbent [31], where the maximum removal of CV was 10 mg/L.

Adsorption isotherm

The most favored approach to an investigation of the adsorption mechanism is a study of the isotherm. The adsorption isotherm refers to the plot of the amount adsorbed against equilibrium concentration at a constant temperature [33]. The implication of the adsorption isotherms in the adsorption mechanism is based on a few aspects, such as the shape of the isotherm, the significance of the plateau in many isotherms, and the orientation of the adsorbed molecules [34,35]. The adsorption isotherms obtained for the adsorption of CV onto UT-CC and SCT-CC at pH 8.00 at room temperature (28±0.5 °C) were justified based on the Langmuir and Freundlich isotherms model.

Langmuir isotherm

The Langmuir isotherm assumed that once the adsorbent site is covered with the dye molecules, no

Figure 4. (a) Variation of the amount of CV dye adsorbed on SCT-CC as a function of pH; (b) Amount of CV dye adsorbed on UT-CC and SCT-CC with the varying initial concentration of dye at pH 8.00 at room temperature (28±0.5 °C).

further adsorption occurs at that site [36]. It also suggests that all the adsorption sites are of equivalent energy, which the Langmuir Isotherm equation can explain −

$$\frac{x}{m} = \frac{aC_e}{1 + bC_e}$$

$$\frac{C_e}{x/m} = \frac{1}{kK_{eq}} + \frac{C_e}{k} \tag{1}$$

or, $$\frac{C_e}{q_e} = \frac{1}{q_m K_{eq}} + \frac{C_e}{q_m} \tag{2}$$

where, x/m - amount adsorbed; C_e - equilibrium concentration; k - rate constant; K_{eq} - equilibrium constant; q_e - amount adsorbed at equilibrium; q_m - amount adsorbed at monolayer; a, b - Langmuir constants.

Freundlich isotherm

The Freundlich isotherm results from the

assumption that the adsorption occurs on a heterogeneous surface, and non-uniform distribution of the heat of adsorption over the adsorbent surface takes place [37,38]. The Freundlich model was applied to calculate the adsorption data of CV, as per the given relation:

$$\frac{x}{m} = K_F C_e^{1/n} \tag{3}$$

or, $$\log\left(\frac{x}{m}\right) = \log K_F + \frac{1}{n} \log C_e \tag{4}$$

The adsorption isotherm found experimentally was fitted relatively more precisely to Freundlich than to Langmuir isotherm for both experiments with UT-CC and SCT-CC at pH 8.00. In the case of UT-CC, the isotherm was found to be the Freundlich type rather

than the Langmuir model. On the other hand, the adsorption isotherm was found to match with both Langmuir and Freundlich isotherms (Figure 5, Table 4) in the case of SCT-CC. The Langmuir isotherm for UT-CC seemed to be quite similar to that of the removal of

CV using polyaniline nanoparticles at the temperature of 308 K with the value of R^2 is 0.607 [39]. However, other research reported a higher value of R^2 (0.99) at the temperature of 308 K for Langmuir isotherm [40].
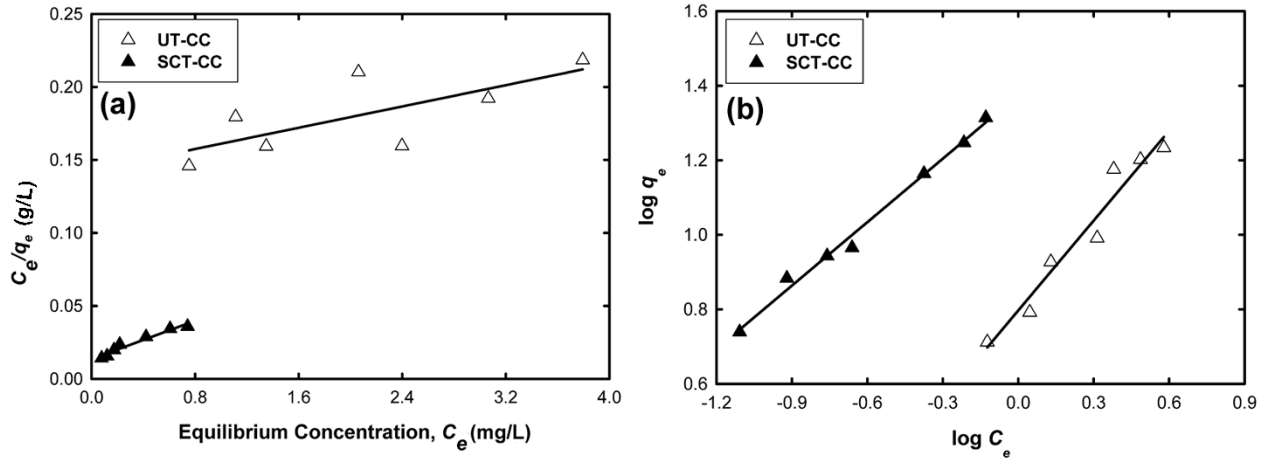
Figure 5. (a) A plot of log C_e/q_e vs. C_e for fitting with Langmuir isotherm for the adsorption of CV on UT-CC and SCT-CC at pH 8.00; (b) A plot of log q_e vs. log C_e for fitting with Freundlich Isotherm for the adsorption of CV on UT-CC and SCT-CC at pH 8.00.

Table 4. Langmuir and Freundlich coefficients for the adsorption of crystal violet dye on untreated (UT-CC) and sodium chlorite treated (SCT-CC) coconut coir at pH 8.00 and room temperature (28±0.5 °C)

Adsorbent	Langmuir Coefficients			Freundlich Coefficients		
	q_m (mg/g)	K_{eq} (L/mg)	R^2	K_F (L/g)	n	R^2
UT-CC	54.94	0.13	0.528	6.26	1.24	0.952
SCT-CC	30.49	2.43	0.950	23.70	1.76	0.991

[N.B.: q_m - amount of CV adsorbed in monolayer; K_{eq} - equilibrium constant; R^2 - correlation coefficient; K_F - Freundlich constant; n - adsorption intensity or number of layers formed.]

Adsorption kinetics

The adsorption kinetics is crucial for understanding the adsorption mechanism and the adsorbate uptake rate. The data obtained from the estimation of equilibrium time for the adsorption of CV on SCT-CC at pH 2.00, 7.00, and pH 8.00 were fitted in both Lagergren's first-order and Ho's pseudo-second-order kinetic equations [41], respectively:

$$\ln(q_e - q_t) = \ln q_e - k_1 t \qquad (5)$$

and

$$\frac{t}{q_t} = \frac{1}{k_2 q_e^2} + \frac{t}{q_e} \qquad (6)$$

where q_e and q_t denote the amounts adsorbed at equilibrium and at any time t, respectively, and k_1 and k_2 are the first-order and second-order rate constants.

The data for first- and second-order kinetics at different pH were depicted in Figures 6(a) and 6(b), respectively. The values of the correlation coefficient, R^2 (indicated in Table 5), revealed that the adsorption kinetics of CV onto SCT-CC mostly follow Ho's pseudo-

second-order kinetics model at all pH.

Adsorption thermodynamics

Thermodynamics determines the different parameters, such as internal energy, enthalpy, entropy, and free energy values of the system, during physical or chemical transformation, which examines how they depend on the reaction conditions. The reaction's spontaneity can be understood by studying the thermal properties of the reactants, such as entropy and enthalpy, to obtain information about the equilibrium. Thermodynamic parameters, such as the change in free energy (ΔG), enthalpy (ΔH), and entropy (ΔS), are calculated by using the following equations:

$$K_d = \frac{q_e}{C_e} \qquad (7)$$

$$\Delta G = -RT \ln K_d \qquad (8)$$

$$\Delta G = \Delta H - T\Delta S \qquad (9)$$

where R is the universal gas constant (8.314 J/mol K), T is the temperature (K), K_d is the distribution coefficient for the adsorption, ΔG is the change in free energy

17
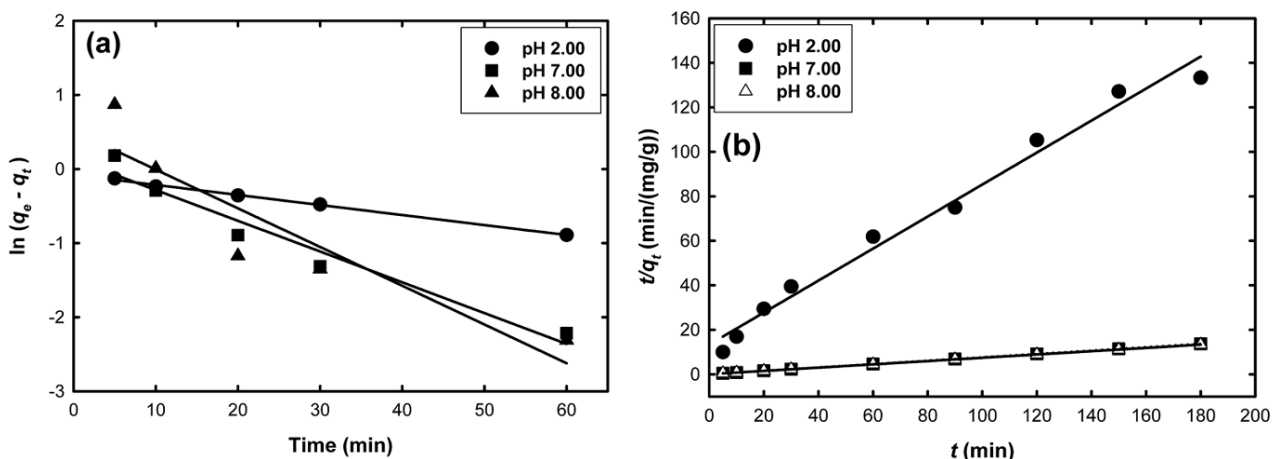
Figure 6. (a) A plot of ln (q_e-q_t) vs. time for fitting with Lagergren equation of first-order kinetics for adsorption of CV on SCT-CC at pH 2.00, 7.00, and 8.00; (b) A plot of t/q_t vs. time for fitting with Ho's equation of pseudo-second-order kinetics for adsorption of CV on SCT-CC at pH 2.00, 7.00 and 8.00.

Table 5. Pseudo first order and pseudo-second order kinetic parameters for the adsorption of crystal violet dye onto SCT-CC at different pH values

pH	q_e (mg/g)	Pseudo-first-order kinetic model		Pseudo-second-order kinetic model	
		k_1 (min^{-1})	R^2	k_2 (g /(mg min))	R^2
2.00	1.24	1.80×10^{-2}	0.996	3.87×10^{-2}	0.982
7.00	13.21	4.15×10^{-2}	0.936	14.65×10^{-2}	1.000
8.00	13.54	5.23×10^{-2}	0.789	10.62×10^{-2}	1.000

[N.B.: q_e - amount of CV adsorbed at equilibrium; k_1 - first order rate constant; k_2 - second order rate constant; R^2 - correlation coefficient]

(kJ/mole), ΔH is the change in enthalpy (kJ/mole), and ΔS is the change in entropy (kJ/mol K).

The value of ΔG can be determined by Eq. (9). As the authors did the thermodynamic study at room temperature only, they studied the variation of the value of ΔG for different adsorbents at different pH values. A more negative value of ΔG for SCT-CC at a high pH indicates how the basic medium is conducive to the spontaneity of the system. The data for free energy at different conditions are incorporated in Table 6.

Table 6. Data for the free energy of the Coir-CV system at room temperature (28±0.5 °C) at different pH values

Adsorbents	Free energy, ΔG (kJ/mol)		
	pH		
	2.00	7.00	8.00
UT-CC	-1.833.1	-	-7.947.4
SCT-CC	5.677.49	-10.153	-12.794

Adsorption mechanism

The FTIR studies have confirmed the existence of hydroxyl (-OH), aldehyde (-CHO), and ether (-O-) groups of lignin in UT-CC and SCT-CC. The biosorption

of CV onto UT-CC and SCT-CC may likely be due to the electrostatic force of attraction between these groups and the cationic dye molecules. The hydroxyl groups become more polar at a high pH (i.e., 7.00 and 8.00). Hence, partially charged hydroxyl can attract the positively charged dye molecules, and binding can occur through H-bond (Figure 7). At pH 2.00, the peak for ether (-O-) at 1237.5 cm^{-1} diminished after adsorption (Figure 7(a) ii), which revealed that in acidic conditions, the ethereal group is protonated, and thus the absorption peak disappeared. There is a weak electrostatic interaction between the dyes and the electron-rich sites of the adsorbent surface, i.e., ether (-O-) groups. The FTIR spectrum shows that the peak for carbon-hydrogen bond {-C-H (stretch} in -CHO at 2860.2 cm^{-1} almost diminishes after adsorption at pH 8 (Figure 7(a) iii), which indicates the van der Waals interaction between polar -HCO group (i.e., aldehyde) and cationic dye, CV.

The FTIR data for the bare SCT-CC in Figure 7(b) illustrates that the broad band at about 3449.7 cm^{-1} (mentioned in Figure 1) became sharpened as the pH of the adsorbate solution was increased from 2.00 to 8.00 (Figure 7(b) ii-iv). It might be owing to the reformation of a hydrogen bond. On the other hand, the
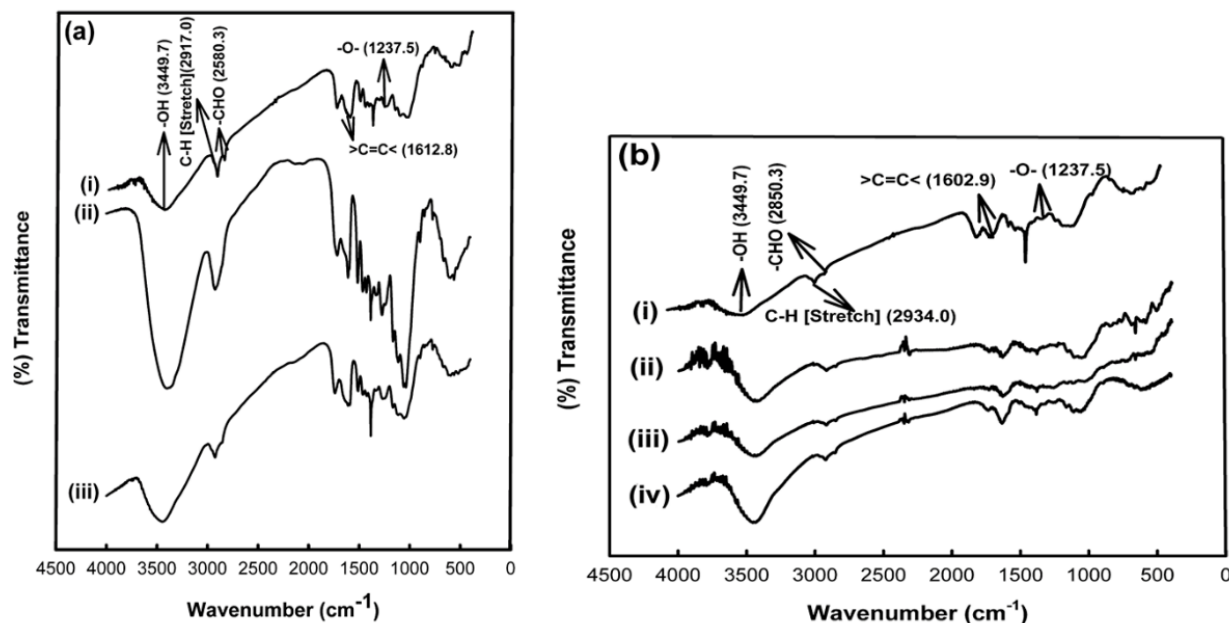
Figure 7. (a) FTIR Spectra of (i) bare UT-CC and CV-adsorbed UT-CC at (ii) pH 2.00 and (iii) pH 8.00; (b) FTIR Spectra of (i) bare SCT-CC and CV-adsorbed SCT-CC at (ii) pH 2.00 and (iii) pH 7.00 and (iv) pH 8.00.

band at 1737 cm⁻¹ in bare SCT-CC, which indicates the existence of aldehydic C=O (Figure 7(b) i) [26], completely diminishes at pH 2.00 because of the protonation of the surface at low pH. On the other hand, the surface becomes conducive to adsorbing cationic dye, CV at pH 8.00 (Figure 7(b) iii). As a result, the peak for aldehydic C=O has a lower intensity, and its frequency shifts to the lower wavenumber (1732.5 cm⁻¹). It may be due to the electrostatic interaction between negatively charged SCT-CC and cationic dye, CV.

DFT simulation

The adsorption scenario of CV⁺ (cationic form) on UT-CC was performed using a density functional theory (DFT) study. A lignin molecule of CC was considered to interact with CV⁺. Firstly, the lignin molecule of CC and a CV⁺ molecule were optimized separately using B3LYP [42,43] functional, and the basis set 6-31G(d,p). Then, CV⁺ was kept on top of the lignin molecule at a certain distance to interact. Figure 8(a) shows the optimized structure of the lignin-CV⁺ complex where
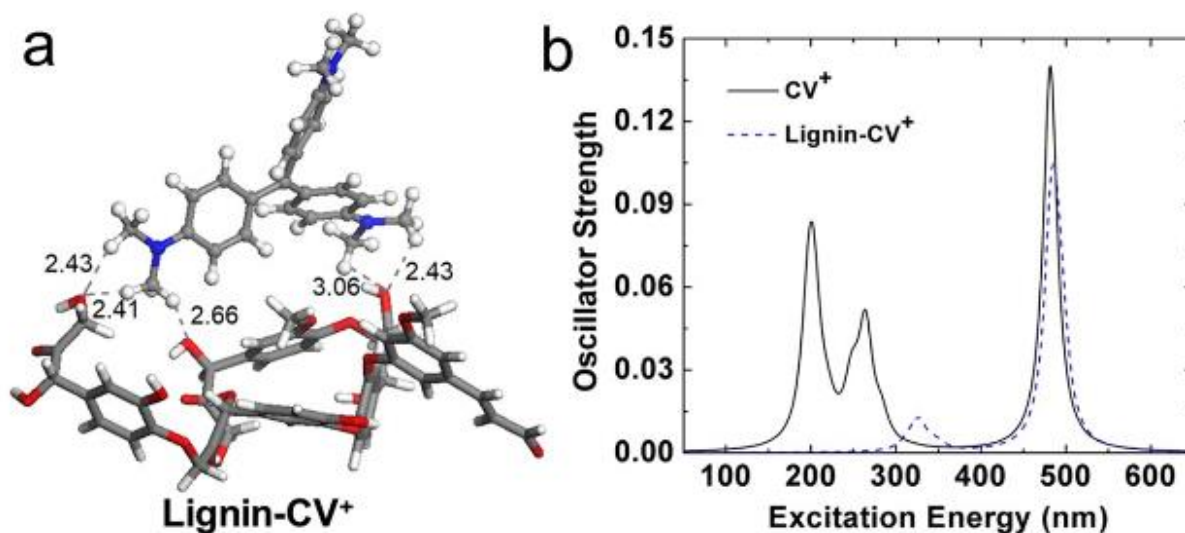
Figure 8. (a) Adsorption of CV⁺ (ball and stick model) on lignin (stick model); (b) UV-vis spectrum of lignin-CV⁺ complex. In figure 8(b), the solid line represents the adsorption spectrum of pristine CV⁺ and the dotted line for the lignin-CV⁺ complex.

CV^+ interacts with lignin through hydrogen bonds. The adsorption energy (ΔE_{ad}) was calculated by subtracting the total energy of lignin and CV^+ from that of the lignin-CV^+ complex. The calculated adsorption energy is -51.16 kJ/mol. Natural bond orbital (NBO) analysis reasserts that during adsorption of CV^+ on lignin, CV detracts 0.033e- charges from lignin. The amount of this charge transfer measures the strength of the interaction between lignin and CV^+ [44]. The adsorption spectra of pristine CV^+ and lignin-CV^+ complex were calculated using TD-DFT with the above-mentioned level of theory to confirm this interaction. The estimated λ_{max} for the pristine CV^+ was found at 482 nm with two low-intensity bands at 201 nm and 264 nm (Figure 8(b)). When CV^+ interacts with lignin, λ_{max} was red-shifted by only 2.0 nm, but the two low-intensity bands of pristine CV^+ diminished towards a weak band and red-shifted at 326 nm. This red shifting and newly appeared weak band for the lignin-CV^+ complex confirms the interaction between CV^+ and lignin. All DFT calculations were carried out using Gaussian16 [45].

CONCLUSION

The adsorption of CV on UT-CC and SCT-CC at different pH values in the batch method was investigated by studying the analytical data and some experimental evidence. On the other hand, the authors also explain the superiority of UT-CC and SCT-CC in removing CV from an aqueous solution by setting a particular experimental condition. Though at lower pH (2.00), UT-CC was observed to be a better adsorbent than SCT-CC in removing CV from aqueous solution, both of these adsorbents showed comparable removal capacity of CV at higher pH (8.00) by the quick attainment (within 30 min) of the equilibrium. Furthermore, the treatment of coconut coir by sodium chlorite brought some change in coir, evidenced by the FTIR data and SEM images. According to the experimental data and other findings, the authors believe that SCT-CC can be treated as a relatively better adsorbent than UT-CC under basic conditions. Using DFT calculation, the calculated adsorption energy of CV on lignin of CC was found to be -51.16 kJ/mol, and the adsorption (of CV on lignin of CC) was confirmed by the calculated adsorption spectra, where the ·max of pristine CV red-shifted after its adsorption.

Acknowledgment

REFERENCES

[1] J.H. Weisburger, Mutat. Res. 506-507 (2002) 9–20. https://doi.org/10.1016/S0027-5107(02)00147-1

[2] R.O. Alves de Lima, A. P. Bazo, D.M.F. Salvadori, C. M. Rech, O. Danielle de Palma, U. Gisela de Aragao, Mut. Res. 626 (2007) 53–60. https://doi.org/10.1016/j.mrgentox.2006.08.002

[3] N. Mathur, P. Bhatnagar, P. Sharma, Univ. J. Environ. Res. Technol. 2(2) (2012) 1–18. https://www.environmentaljournal.org/2-2/ujert-2-2-1.pdf

[4] B. Lellis, C.Z. Fávaro-Polonio, J.A. Pamphile, J.C. Polonio, Biotechnol. Res. Innov. 3(2) (2019) 275–290. https://doi.org/10.1016/j.biori.2019.09.001

[5] M .Sudha, A. Saranya, G. Selvakumar, N. Sivakumar, Int. J. Curr. Microbiol. App. Sci. 3(2) (2014) 670–690. https://www.ijcmas.com/vol-3-2/M.Sudha,%20et%20al.pdf

[6] S. P. Upadhyay, J. Environ. Res. Dev. 3(2) (2008) 490–494.http://www.jerad.org/ppapers/V003N002/V003N002 P0490.pdf

[7] A. Gurses, C. Dogar, M. Yalcin, M. Acikyildiz, R. Bayrak, S. Karaca, J. Hazard. Mater. 131(6) (2006) 217–228. https://doi.org/10.1016/j.jhazmat.2005.09.036

[8] C. Allegre, P. Moulin, M. Maisseu, F. Charbit, J. Membr. Sci. 269(4) (2006) 15–34. https://doi.org/10.1016/j.memsci.2005.06.014

[9] K. Kadirvelu, K. Thamaraiselvi, C. Namasivayam, Bioresour. Technol. 76 (2001) 63–65. https://doi.org/10.1016/S0960-8524(00)00072-9

[10] J.A. Ramsay, T. Nguyen, Biotech. Lett. 24(21) (2002) 1757–1761. https://doi.org/10.1023/A:1020644817514

[11] K.B. Hu, Y.L. Wang, C.R. Li, Y.Q. Zheng, Acta Sci. Circumstantiae 30(11) (2010) 2174–2183. http://caod.oriprobe.com/articles/25753718/Fractal_charac teristics_of_adsorption_of_direct_dye_compounds_onto_ mod.htm

[12] E. Bascetin, G. Atun, J. Chem. Eng. Data 55 (2010) 783–788. https://doi.org/10.1021/je9004678

[13] M.L. Zanota, N. Heymans, F. Gilles, B.L. Su, M. Frer, G.D. Weireld, J. Chem. Eng. Data 55 (2010) 448–458. https://doi.org/10.1021/je900539m

[14] S. Madhavakrishnan, K. Manickavasagam, R. Vasanthakumar, K. Rasappan, R. Mohanraj, S. Pattabhi, e-J. Chem. 6(4) (2009) 1109–1116. https://doi.org/10.1155/2009/764197

[15] A. Adak, M. Bandyopadhyay, A. Pal, Sep. Purif. Technol. 44(2) (2005) 139–144. https://doi.org/10.1016/j.seppur.2005.01.002

[16] C.D. Lin, C.T. Chen, Anim. Feed Sci. Technol. 54 (1995) 217–226. https://doi.org/10.1016/0377-8401(94)00760-7

[17] C.L. Hall, P.B. Hamilton, Poult. Sci. 6 (1982) 62–66. https://doi.org/10.3382/ps.0610062

[18] R.L. Berrios, J.L. Arbiser, Dermatol. Clin. 29(1) (2011) 69–73. https://doi.org/10.1016/j.det.2010.08.009

[19] A. Pona, E.Y. Quan, A. Cline, S.R. Feldman, Dermatol Online J. 26(5) (2020) 13030.

https://doi.org/10.5070/D3265048772

[20] P. Das, S. Chakraborty, S. Chowdhury, Arch. Environ. Sci. 6 (2012) 57–61. https://aes.asia.edu.tw/Issues/AES2012/SahaPD2012-1.pdf

[21] A. Mittal, J. Mittal, A. Malviya, D. Kaur, V.K. Gupta, J. Colloid Interface Sci. 343 (2009) 463–473. https://doi.org/10.1016/j.jcis.2009.11.060

[22] Y. Lin, X. He, G. Han, Q. Tian, W. Hu, J. Environ. Sci. 23(12) (2011) 2055–2062. https://doi.org/10.1016/S1001-0742(10)60643-2

[23] U.J. Etim, E. Inam, S.A. Umoren, U.M. Eduok, Int. J. Environ. Bioenergy 5(2) (2013) 62–79. https://modernscientificpress.com/Journals/ViewArticle.aspx?gkN1Z6Pb60HNQPymfPQlZF418S3XB/1Y/g5SJIrtEz9tnj9x30LtKANTNh7z40/x

[24] J. de Souza Macedo, C.J. Nivan B. da, E.A. Luis, S.V. Eunice F. da, R.C. Antonio, F.G. Iara de, V.C. Neftali L., S.B. Ledjane, J. Colloid Interface Sci. 298 (2006) 515–522. https://doi.org/10.1016/j.jcis.2006.01.021

[25] L. Yi, W. Jintao, Z. Yian, W. Aiqin, Chem. Eng. J. 184 (2012) 248–255.https://doi.org/10.1016/j.cej.2012.01.049

[26] D.L. Pavia, G.M. Lampman, G.S. Kriz, Introduction to Spectroscopy: A Guide for Students of Organic Chemistry, 3rd Ed, Thomson Learning, (2001), p. 26. https://www.hdki.hr/_download/repository/Pavia-Introduction-to-Spectroscopy%5B1%5D.pdf

[27] S. Keshk, W. Suwinarti, K. Sameshima, Carbohydr. Polym. 65 (2006) 202–206. https://doi.org/10.1016/j.carbpol.2006.01.005

[28] A. Saeed, M. Sharif, M. Iqbal, J. Hazard. Mater. 179(1-3) (2010) 564–572. https://doi.org/10.1016/j.jhazmat.2010.03.041

[29] R. Ahmad, J. Hazard. Mater. 171(1-3) (2009) 767–773. https://doi.org/10.1016/j.jhazmat.2009.06.060

[30] S. Iman, S. Mahboube, S. Abolfazl, H. Mohsen, H. Saeed, Arab. J. Sci. Eng. 41 (2016) 2611–2621. https://doi.org/10.1007/s13369-016-2109-3

[31] M. Chandrasekaran, M.S. Vaiyazhipalayam, T. Marimuthu, J. Taiwan Inst. Chem. Eng. 63 (2016) 354–362. https://doi.org/10.1016/j.jtice.2016.03.034

[32] A.L. Prasad, T. Shanti, Sustain. Environ. Res. 22(2)

(2012) 113–122.

[33] S.H. Maron, C.F. Prutton, Principles of Physical Chemistry, MacMiillan Publishing Co., (1972), p. 813.

[34] R.A. Latour, J. Biomed. Mater. Res. A: 103A: (2015) 949–958. https://doi.org/10.1002/jbm.a.35235

[35] M.B. Yahia, Y.B. Torkia, S. Knani, M.A. Hachicha, M. Khalfaoui, A.B. Lamine, Adsorpt. Sci. Technol. 31(4) (2013) 341–357. https://doi.org/10.1260/0263-6174.31.4.341

[36] R.P.H, Gasser, An Introduction to Chemisorption and Catalysis by Metals, Oxford University Press, (1987), p. 12. ISBN 0198552718

[37] N. Ayawei, S.S. Angaye, D. Wankasi, E.D. Dikio, Open J. Phys. Chem. 5(3) (2015a) 56–70. https://doi.org/10.4236/ojpc.2015.53007

[38] N. Ayawei, A.T. Ekubo, D. Wankasi, E.D. Dikio, Orient. J. Chem. 31(30) (2015b) 1307–1318. http://dx.doi.org/10.13005/ojc/310307

[39] S. Muhammad, T. Hajira, K. Jawariya, H. Uzma, S. Atika, Ultrason. Sonochem. 34 (2017) 600–608. https://doi.org/10.1016/j.ultsonch.2016.06.022

[40] S.R. Shirsath, A.P. Patil, B.A. Bhanvase, S.H. Sonawane, J. Environ. Chem. Eng. 3(2) (2015) 1152–1162. https://doi.org/10.1016/j.jece.2015.04.016

[41] Y. Ho, G. McKay, Process Biochem. 34(5) (1999) 451–465. https://doi.org/10.1016/S0032-9592(98)00112-5

[42] A.D. Becke, J. Chem. Phys. 98(7) (1993) 5648–5652. https://doi.org/10.1063/1.464913

[43] C. Lee, W. Yang, R.G. Parr, Phys. Rev. B 37(2) (1988) 785–789. https://doi.org/10.1103/physrevb.37.785

[44] J.K. Saha, M.S. Hossain, M.K. Ghosh, Struct. Chem. 30 (2019) 1427–1436. https://doi.org/10.1007/s11224-018-1272-4

[45] M.J. Frisch, G.W. Trucks, H.B. Schlegel, G.E. Scuseria, M.A. Robb, J.R. Cheeseman, G. Scalmani, V. Barone, et. al., Gaussian 16 Rev. C.01, Wallingford, CT (2016).

NAFEES AHMED[1]
MD. YASIN HOSSAIN[1]
JOYANTA KUMAR SAHA[1]
MOHAMMAD AL MAMUN[1,2]
A. K. M. LUTFOR RAHMAN[1]
JAMAL UDDIN[3]
ABDUL AWAL[1]
MD. SHAJAHAN[1]

[1]Department of Chemistry, Jagannath University, Dhaka, Bangladesh

[2]Nanotechnology and Catalysis Research Centre, Institute of Advanced Studies, University of Malaya, Kuala Lumpur, Malaysia

[3]Center for Nanotechnology, Chemistry, and Nanotechnology, Department of Natural Sciences, Coppin State University, Science and Technology Center, Baltimore, USA

UKLANJANJE BOJE KRISTAL VIOLET IZ VODENOG RASTVORA NA ADSORPCIJOM NA KOKOSOVOM VLAKNU

Netretirana i kokosova vlakna obrađena natrijum-hloritom su primenjena za uklanjanje kristal violeta (CV) iz vodenog rastvora šaržnom adsorpcijom. Kapacitet adsorpcije, vreme ravnoteže i kinetika adsorpcije CV na oba adsorbenta su istraženi na kontrolisanim pH vrednostima rastvora boje. Visok pH poboljšava kapacitet adsorpcije oba adsorbenta. Nasuprot tome, pri niskoj pH vrednosti, neobrađena kokosova vlakna (UT-CC) pokazuju veću efikasnost adsorpcije (9,61 mg g^{-1}) nego kokosova vlakna obrađena natrijum-hloritom (SCT-CC). Na pH = 2,00, ravnoteža se uspostavlja za 60 min sa oba adsorbenta. Međutim, brže postizanje ravnoteže (30 min) primećeno je za adsorbenta na višem pH (8,00). Utvrđeno je da se podaci istraživanja ravnoteže pri pH 8,00 za oba adsorbenta bolje slažu sa Frojndlihovim nego sa Langmirovim modelom. Kinetički podaci se dobro slažu sa Huovim modelom pseudo-drugog reda. Oba adsorbenta su okarakterisana FTIR i SEM da bi se dobili dokazi za predloženi mehanizam adsorpcije. Teorija funkcionalne gustine (DFT), takođe, podržava ovaj rezultat koji ilustruje adsorpciju CV na ligninu kokosovog vlakna sa adsorpcionom energijom -51,16 kJ/mol na nivou teorije B3LIP/6-31(d,p).

Ključne reči: kokosovo vlakno, natrijum-hlorit, kristal violet, kinetika adsorpcije, mehanizam adsorpcije, teorija funkcionalne gustine.

ATHEER M. AL-YAQOOBI[1]
MUNA N. AL-RIKABEY[2]

[1]Department of Chemical Engineering, College of Engineering, University of Baghdad, Iraq

[2]Department of Biochemical Engineering, Al-Khwarizmi College of Engineering, University of Baghdad, Iraq

ELECTROCHEMICAL HARVESTING OF *CHLORELLA* SP.: ELECTROLYTE CONCENTRATION AND INTERELECTRODE DISTANCE

Article Highlights

- The presence of Cl⁻ ions have a noticeable effect on the performance of the harvesting process
- Maximum efficiency achieves in a short electrolysis time at 2 g NaCl/l for both electrodes
- It takes a longer time to achieve maximum efficiency at 5 g/l NaCl
- The lower energy consumption is achieved with Al, which decreases with increasing NaCl concentration
- Reducing the electrode gap decreases the time required to reach the maximum efficiency

Abstract

Two modes of electrochemical harvesting for microalgae were investigated in the current work. A sacrificial anode (aluminum) was used to study the electrocoagulation-flotation process, and a nonsacrificial anode (graphite) was used to investigate the electroflotation process. The study inspected the effect of chloride ions concentration and the interelectrode distance on the performance of the electrochemical harvesting processes. The results demonstrated that both electrodes achieved maximum harvesting efficiency with a 2 g/L NaCl concentration. Interestingly, by increasing the NaCl concentration to 5 g/L, the harvesting efficiency reduced dramatically to its lowest value. Generally, the energy consumption decreased with increasing of NaCl concentration. Moreover, the energy consumption achieved with aluminum anodes is lower than that achieved with graphite. However, by increasing the gap between the electrodes from 15 mm to 30 mm, the time required to achieve the maximum efficiency doubled, and energy consumption increased consequently.

Keywords: electrochemical harvesting, electrocoagulation, Chlorella sp., non-sacrificial electrode, energy consumption.

SCIENTIFIC PAPER

UDC 544.6:58:66

The two significant challenges facing human developments in recent decades are world energy and global warming. These challenges are intensified because of the fast population growth, industries, and the consequent increase in conventional fossil fuel production demands [1]. The complete reliance on fossil-based fuels associated with escalating emissions of Green House Gases (GHG) in the atmosphere is considered the primary factor of severe global climate problems in the present and future years. Moreover, because of the probability of depletion in the fossil fuel reserves, many developed countries have invested considerable funds to investigate alternative renewable and environment-friendly energy sources [2]. Biofuels are considered promising forms of energy that can overcome the negative impacts of fossil fuels on living organisms, including human health. Among various biofuel sources, microalgae have been proposed as an ideal renewable energy route that can efficiently replace conventional fossil-based fuels. Several features make microalgae the key to the next generation of energy, such as high oil content, rapid biomass growth, ability to mitigate the emissions of

CO_2, and other features that make microalgae superiority over other types of biomass for sustainable development [3,4].

The critical barrier to the commercial production of biofuels from microalgae is their economic feasibility compared with conventional fossil-based fuels. The process of biofuel production involves several steps. The harvesting of microalgae biomass considers the most costly and complicated step in the biorefinery process of biofuel production. Namely, microalgae are in a high diluted mixture (usually 0.1–2.0 g/L) and small size (less than ten micrometers in diameter) for most microalgae strains [5,6].

Different techniques have been exploited for microalgae harvesting, such as centrifugation, sedimentation, flocculation, filtration, flotation, etc. [2, 7–9]. However, the disadvantages of most of these techniques are associated with high operating costs and low efficiency [10].

Electrocoagulation-flocculation approach has been reported as one of the successful tools in wastewater treatment. Moreover, this technique is considered an alternative to conventional chemical coagulants, which use metal salt as chemical coagulants, such as Fe^{3+} or Al^{3+} salts [11–13]. The benefits of the electrocoagulation-flocculation process include easy operation, avoiding adding chemicals, and high efficiency [14].

During the electrocoagulation-flocculation process, Fe^{3+} or Al^{3+} ions are produced by dissolving a sacrificial anode through oxidation reaction as the following reaction on the anode [12,15]:

$$Al \rightarrow Al^{3+} + 2e^- \tag{1}$$

$$2H_2O \rightarrow 4H + O_2 + 4e^- \tag{2}$$

The following reaction accrue in the solution:

$$Al^{3+} + 3H_2O \leftrightarrow Al(OH)_3 + 3H^+ \tag{3}$$

The electrochemical reduction of water takes place at the cathode:

$$2H_2O + 2e^- \rightarrow H_2 + 2OH^- \tag{4}$$

The Al^{3+} ions are dissolved from the anode and react to produce positive charge coagulants, the latter attracts the negative charge microalgae, and the resulting flocs were floated by the aid of the microbubbles (H_2 and O_2) realized on electrodes surfaces.

When chlorides are present in the culture; chlorine, hypochlorous acid, and hypochlorite can be produced from the anodic oxidation of chlorides as in reactions below [11,16]

$$2Cl^- \rightarrow 2e + Cl_2 \tag{5}$$

$$Cl_2 + H_2O \rightarrow HOCl + Cl^- + H^+ \tag{6}$$

$$HOCl \leftrightarrow OCl^- + H^+ \tag{7}$$

The dissolved electrode material is one of the parameters that enhance the cost of the electrocoagulation-flocculation process. However, this type of electrode material requires parodic replacement, and the extensive concentration of dissolved material ions hurts the microalgae and the environment [17,18]. Consequently, other types of electrode materials have been used for the electrochemical harvesting of microalgae. In addition, non-sacrificial electrodes like a boron-doped diamond [19], carbon [18], and other electrodes have been examined for the same purpose.

The polarity of the non-sacrificial electrode drives the negative charge microalgae toward the surface of positive charge anodes and neutralizes there. The resulting algal aggregates are driven upward by the action of the microbubble formatted on the electrodes [20,21].

In the current study, microalgae's electrochemical harvesting is investigated using sacrificial (aluminum) and non-sacrificial (graphite) electrodes. Furthermore, the harvesting efficiency and energy consumption were evaluated based on the effect of the variation in inter-electrode distance and electrolyte concentration.

MATERIAL AND METHODS

Cultivation of microalgae

The microalgae strain used in the current study was *Chlorella* sp., which was offered kindly from the department of Biology/Ibn-Haitham College of Education/University of Baghdad. Ten ml of OD= 1 microalgae inoculate were transferred to two 250 ml flasks containing 100 ml sterile Chu-13 media. Then, two glass jars of 5 liters were used for incubation with fresh culture media at a temperature of 25±2 °C. The algal culture was grown at a fixed light intensity of 2500 Lux with 16/8 light-dark conditions. A continuous air stream was supplied to both growth containers at 500 ml/min for 6 hours daily.

Electrocoagulation experiments

The experimental work was conducted using a Plexiglass cylindrical cell of 9 cm diameter and 10.5 height, as described previously [22]. Two types of electrode material were used as anode martial to compare the electrochemical behaviors of both processes, representing the sacrificial electrode (aluminum) and non-sacrificial electrode (graphite). Both electrodes were of 9 cm × 1 cm × 6 cm dimensions. The cathode used in this work was made of aluminum and had a similar size to the anode electrode. A DC power was supplied to the cell at constant current mode by(Smart Power System) model

AL-YAQOOBI & AL-RIKABEY: ELECTROCHEMICAL HARVESTING OF....

Chem. Ind. Chem. Eng. Q. 29 (1) 23–29 (2023)

EMA-01-32-15-P. The applied current was fixed at 0.2 A for all experiments. A magnetic stirrer (Corning, model PC-410) was used for applied constant mixing at a speed of 200 rpm.

For the aluminum electrode cleaning, the electrodes were washed with 1 M HCl solution for 30 minutes, sanded with abrasive paper, and then rinsed with distilled water.

The harvesting efficiency of the microalgal was calculated based on the change in optical density of the culture suspension. The samples were collected from the electrochemical cell at a constant level of 5 cm from the liquid surface. A spectrometer UV-VIS (Bio-Rad, Smartspec plus) was used to measure the optical density of samples at 680 nm. The harvesting efficiency was calculated according to the following equation:

$$harvesting\ efficiency\ (\%) = \frac{(OD_i - OD_t)}{OD_i} \times 100 \quad (8)$$

where OD_i is the optical density of the initial suspension, and OD_t is the optical density of the suspension at a time (t).

The power consumption (in kWh/kg of recovered microalgae) was calculated using Eq. (9):

$$PC = \frac{(P \times t)}{1000 \times V \times \mu_a \times C_i} \quad (9)$$

where P is the power (W), t is the electrolysis time (h), V is the volume of the microalgal broth treated (m^3), μ_a is the microalgae recovery efficiency, and C_i is the initial microalgae biomass concentration (kg/m^3).

RESULTS AND DISCUSSION

Electrolyte concentration

The effect of electrolyte concentration on the harvesting efficiency of *Chlorella* sp. was investigated with different NaCl concentrations (1, 2, 3, and 5) g/L at a constant applied current of 0.2 A, and the pH of the culture medium was around 10. The results in Figure 1 revealed that the harvesting efficiency of *Chlorella* sp. at 1–2 g/L NaCl concentration increased sharply, and consequently, the maximum removal efficiency was reached in a short electrolysis time. The harvesting efficiency of around 96% and the concentration of 2 g/L were achieved in 12 min. However, increasing the NaCl concentration to 3–5 g/L had a markedly negative influence on the removal efficacy. It required 14 min to obtain around 89% harvesting efficiency with an electrolyte concentration of 5 g/L. Furthermore, the removal efficiency of 3.5 g/L NaCl barely reached the response without NaCl addition by the end of the experimental time.
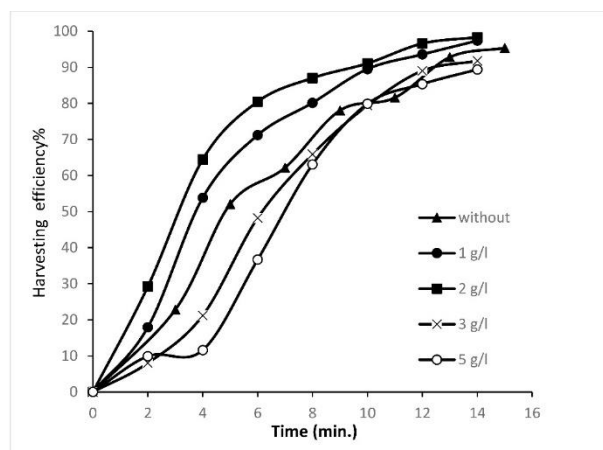
Figure 1. The effect of electrolyte concentration on the harvesting efficiency for the aluminum anode.

For the graphite electrode, the trend of harvesting efficiency is similar to that obtained with the aluminum electrode. Figure 2 shows the effect of different electrolyte concentrations (1, 2, 3, and 5 g/L) on the harvesting efficiency of microalgae. With the electrolyte concentrations of 1, 2, and 3 g/L, the harvesting efficiency was higher than that obtained without adding NaCl. However, with a NaCl concentration of 3 g/L, the removal efficiency was lower than that at 1 g/L and 2 g/L. The harvesting efficiency of more than 98% was achieved in 14 min with electrolyte concentrations of 1 and 2 g/L. In comparison, it required 20 min to obtain about 95% harvesting efficiency with the electrolyte concentration of 3 g/L. Moreover, in compression to zero NaCl addition broth, an increase of the NaCl concentration to 5 g/L has a marked reduction in the removal efficiency for the first 10 minutes of electrolysis time. However, after that, the removal efficiency recovered was almost comparable to that obtained without adding NaCl.
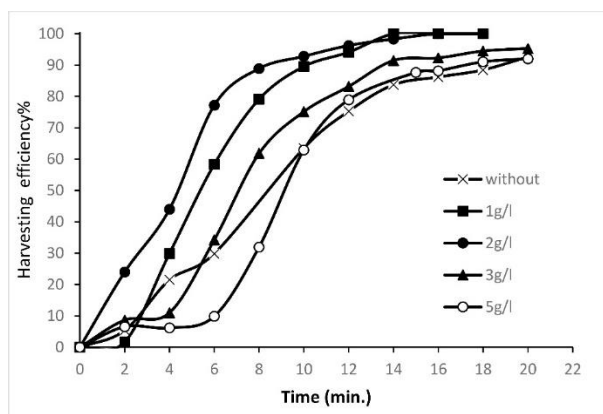
Figure 2. The effect of electrolyte concentration on the harvesting efficiency for the graphite anode.

The above experiments show that both electrodes' highest and lowest harvesting efficiencies were achieved with concentrations of 2 g/L and 5 g/L, respectively. Consequently, the harvesting efficiency of

the two electrode types were compared between these two limiting concentrations, i.e., 2, 5 g/L of NaCl.

Figure 3 compares using aluminum and graphite electrodes at the electrolyte concentrations of zero, 2, and 5 g/L. The harvesting efficiency with the aluminum electrode is higher than that obtained with the graphite electrode in all electrolyte concentrations. For example, with electrolyte concertation of 5 g/L, it required 12 min to achieve a harvesting efficiency of 79% by a graphite electrode. In contrast, for the aluminum anode, the harvesting efficiency was around 85% for the same electrolysis time. However, with an electrolyte concentration of 2 g/L after 6 min of electrolysis time, the graphite anode's harvesting efficiency was enhanced to a level obtained with the aluminum anode.
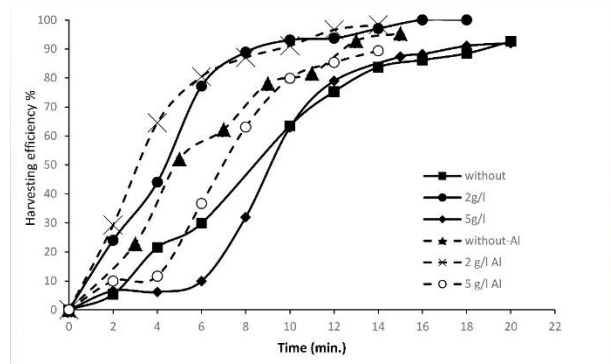
Figure 3. Comparison of graphite and aluminum anodes' harvesting efficiencies with different electrolyte concentrations. The solid line represents the graphite electrode, and the dashed line represents the aluminum electrode.

The presence of chlorine ions in the mixture improved the removal process by increasing the amount of Al^{3+} released by the aluminum electrode and enhanced the current efficiency. The current efficiency increased by approximately 15% when 2 g/L of NaCl was added. It was attributed to the rising conductivity of the electrolyte, which reduced cell voltage. Consequently, at low cell potential, the aluminum dissolution reaction was preferred over the oxygen evaluation reaction [23]. However, the presence of Cl^- in the culture medium reduced the effect of other ions, which could impede the aluminum dissolution and the formation of aluminum hydroxide. Furthermore, the vital rule of chlorine ions was in the de-passivating action of the oxide layer formed on the electrode surface [24,25]. As a result, the passive film built on the electrode led to an increase in energy consumption and a decrease in process efficiency. In addition, when Cl^- is present in the solution, pitting corrosion occurs at the aluminum anode surface, accelerating the dissolution and formation of Al^{3+} [26].

In the electrochemical harvesting process using a sacrificial or nonsacrificial electrode, the increased

NaCl concentration in the algal culture may improve the harvesting efficiency due to the increased mass transport of ions to the anode surface [21].

On the other hand, in the electrochemical harvesting of microalgae process, a noticeable decrease in the active chlorine concentration. It could be caused by the reaction between active chlorine and the microalgae cells immediately after its generation, which also has been proved for *Chlorella vulgaris* microalgae [26–29]. It was observed that the algae cells were damaged and lysed due to the presence of Cl^- in the electrochemical process. The pores formed in cell membranes by the external electric field permitted the generated oxidants to penetrate the cells and led to the oxidation of the cell's cellular constituents. Additionally, due to damage to cell membranes, the chlorophyll-a may be subtracted from the cell to the solution and oxide by the active chlorine species generated through the process [26,30,31].

Furthermore, the oxidation agents generated during the process in the presence of Cl^- had an adverse effect on the floc formation [32]. It has been reported that a decrease in Al^{3+} released occurs at higher Cl^- concentration [33]. The Cl^- ions could deposit on the surface of polymeric aluminum hydrolysis and aluminum hydroxide species, which affects their function in generating active flocs [34]. In fact, according to *Aitbara* et al. [35], when chlorides are in contact with $Al(OH)_3$ in the solution, different intermediate species could be produced, such as $Al(OH)Cl_2$, $Al(OH)Cl_2$, and $AlCl_3$. Also, $AlCl_4$ anion can be produced at a high Cl^- concentration, which contributes to the dissolution of aluminum species and impedes the floc's formation. Moreover, the presence of active chlorine species and radicals (Cl_2, $HOCl$, ClO^- •Cl, $•Cl_2^-$) and other reactive species in the electrolyte have multiple effects on the microorganism, as listed in Table 1 [29].

All of the reasons mentioned above clearly show that adding NaCl can improve the process removal efficiency. However, microalgae cells can be damaged at specific NaCl concentrations, negatively influencing the electrocoagulation process when aluminum electrodes are used. That may explain the sensitivity of the electrocoagulation process to NaCl, where the removal efficiency of 3 g/L of NaCl was lower than that obtained without adding NaCl when the aluminum is used.

The influence of NaCl addition on microalgae removal efficiency obtained in the current study is harmonious with the results stated by several previous studies. For example, the process efficiency of harvesting freshwater *M. aeruginosa* improved by adding NaCl from 1–5 g/L, but the efficiency started to

AL-YAQOOBI & AL-RIKABEY: ELECTROCHEMICAL HARVESTING OF....

Chem. Ind. Chem. Eng. Q. 29 (1) 23−29 (2023)

reduce at an excess concentration of 8 g/L [26]. On the other hand, the removal efficiency of *Chlorella sorokiniana* microalgae using the carbon electrode increased by adding NaCl to the *Chlorella* culture [21].

Table 1. Effect of reactive species on the microorganism in the electrolysis process

Reactive species	Effect
Chlorine	DNA replication enzymes inhibition
ClO_2^-	Changes in cell walls due to oxidation of amino groups
	Disruption of proteo-synthesis
	Disruption of glucose oxidase
O_3	Destruction of cell membranes
	Reaction with glutathione
	Damages of chromosomal DNA
Hydroxyl radicals	Strand breaking in DNA radicals
	Reaction with nucleic acids
	Cell deformation leads to their rupture

Economic feasibility is the most affecting parameter in any process that determines the process efficiency. The energy consumption is calculated based on 90% harvesting efficiency using Eq. 9. Figure 4 shows the effect of NaCl concentration on energy consumption (kWh/kg). It can be observed that the energy consumption obtained with the aluminum electrode is lower than that of graphite with different NaCl concentrations. The energy consumption achieved with graphite at 1 g/L NaCl was 1.7 kWh/kg, decreasing dramatically to around half when the aluminum electrode was used at the same electrolyte concentration. By increasing NaCl concentration, the electrolyte's conductivity increased, the cell voltage decreased, and the energy consumption decreased. However, according to Eq. 9, the time required to achieve 90% is another vital parameter determining energy consumption. The optimum energy consumption achieved with the graphite electrode was 0.413 kWh/kg at an electrolyte concentration of 2 g/L. While with the aluminum electrode, the optimum energy consumption was 0.246 kWh/kg at an electrolyte concentration of 5 g/L. Nevertheless, the optimum removal efficiency was achieved at a NaCl concentration of 2 g/L, at which the energy consumption was 0.258 kWh/kg.

Distance between electrodes

The effect of inter-electrode distance on the harvesting efficiency and energy consumption was investigated with two inter-electrode gaps of 15 mm and
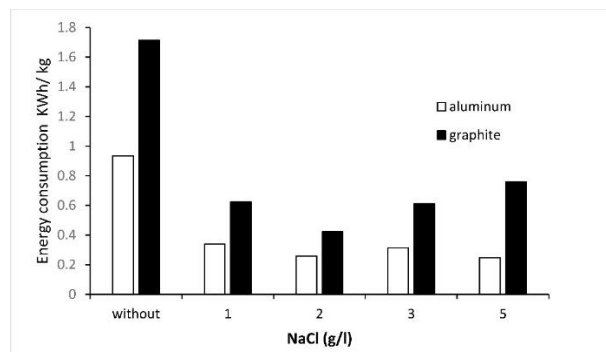
Figure 4. Comparison between the energy consumption of graphite and aluminum anodes with different electrolyte concentrations.

30 mm. The experiment conditions were kept constant at an applied current of 0.2 A without adding NaCl. Figure 5 demonstrated that increasing the distance between the electrodes increases the electrolysis time required to reach the maximum harvesting efficiency. For example, the graphite electrode needed about 20 min to achieve around 92% harvesting efficiency when the gap between the electrodes was 15 mm. At the same time, it took approximately 26 min to attain similar harvesting efficiency when the distance increased to 30 mm. Likewise, with the aluminum electrode, similar behavior was noted. However, the electrolysis time required to reach around 92% decreased from 18 to 13 min when the inter-electrode distance was reduced from 30 mm to 15 mm.
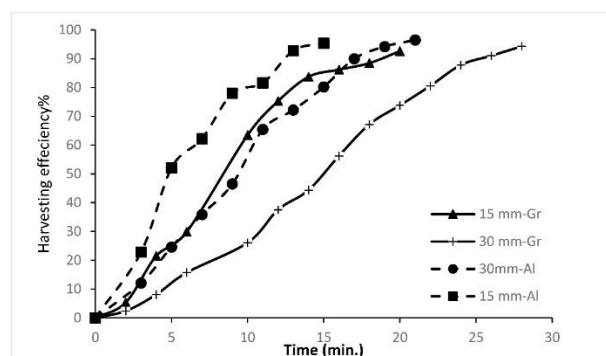
Figure 5. Harvesting efficiency of graphite and aluminum anodes with a distance between the electrodes of 15 mm and 30 mm. The solid line represents the graphite electrode, and the dashed line represents the aluminum electrode.

The reduction of distance between the electrodes increases the process efficiency by increasing the amount of dissolved Al^{+3} and enhancing the performance of flotation and floc formation [11,36,37].

Furthermore, the distance between the electrodes showed a clear impact on the energy consumption for both electrode types, as shown in Figure 6. It can be observed from the results that reducing the gap between the electrodes results in a high reduction in energy consumption. For aluminum electrodes, the energy consumption reduced from 1.4 kWh/kg to

0.93 kWh/kg when the distance was reduced from 30 mm to 15 mm. Likewise, with the graphite electrode, the energy consumption decreased from 2.75 kWh/kg to 1.71 kWh/kg when the electrode gap was reduced from 30 mm to 15mm. The energy reduction is attributed to the decrease in cell resistance with decreasing the inter-electrode distance.
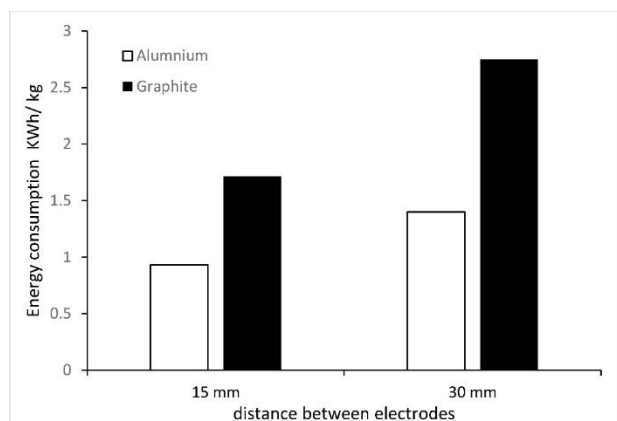
Figure 6. Effect of distance between electrodes on energy consumption for aluminum and graphite electrodes.

CONCLUSION

Although both types of electrodes (aluminum and graphite anodes) have achieved a maximum removal efficiency of the *Chlorella* sp. suspensions, the aluminum anode is more efficient. Cl^- ions have a noticeable effect on the performance of the electrochemical harvesting process. However, the concentration of chloride ions has to be controlled to a specific limit. Maximum harvesting efficiency of 96% has been achieved in a short electrolysis time of 12 min and 14 min with 2 g/L of NaCl for aluminum and graphite electrodes, respectively. With increasing the NaCl concentration to 5 g/L, harvesting efficiency takes longer to achieve the desired value. In general, aluminum anode energy consumption is lower than that of the graphite one. The increase in the NaCl concentration decreases energy consumption. However, electrolysis time is an important parameter in determining energy consumption. The lowest energy consumption value of 0.413 kWh/kg was achieved at 2 g/L of NaCl with graphite, while it was 0.258 kWh/kg with the aluminum one under the same conditions.

The electrolysis time required to achieve the maximum harvesting efficiency was reduced from 26 min to 20 min when the inter-electrode distance decreased from 30 mm to 15 mm for the graphite electrode and from 18 min to 13 min for the aluminum electrode. The energy consumption also decreases with the gap between the electrodes. It was reduced

28

from 1.4 kWh/kg to 0.93 kWh/kg with the aluminum electrode and from 2.75 kWh/kg to 1.71 kWh/kg with the graphite electrode.

REFERENCES

[1] S.R. Medipally, F.M. Yusoff, S. Banerjee, M. Shariff, J. Hazard. Mater. 2015 (2015) 519–513. https://doi.org/10.1155/2015/519513

[2] S.M.A. Mobin, F. Alam, in Application of Thermo-fluid Processes in Energy Systems, M.M.K. Khan, A.A. Chowdhury, N.M.S. Hassan, Springer, Singapore, (2018) p. 83–108. ISBN-13: 978-9811006951

[3] M.G. Saad, N.S. Dosoky, M.S. Zoromba, H.M. Shafik, Energies 12 (2019) 19–20. https://doi.org/10.3390/en12101920

[4] D. Moreira, J.C.M. Pires, Bioresour. Technol. 215 (2016) 371–379. https://doi.org/10.1016/j.biortech.2016.03.060

[5] B. Behera, K. Nageshwari, M. Darshini, and P. Balasubramanian, Water Sci. Technol. 82 (2020) 1217–1226. https://doi.org/10.2166/wst.2020.143

[6] N. Krishnamoorthy et al., J. Environ. Chem. Eng. 9 (2021) 105875. https://doi.org/10.1016/j.jece.2021.105875

[7] B. Behera and P. Balasubramanian, Bioresour. Technol. 283 (2019) 45–52. https://doi.org/10.1016/j.biortech.2019.03.070

[8] J. Kim, G.Yoo, H. Lee, J. Lim, K. Kim, C.W. Kim, M.S.Park, J.W. Yang, Biotechnol. Adv. 31 (2013) 862–876. https://doi.org/10.1016/j.biotechadv.2013.04.006

[9] R. Henderson, S.A. Parsons, B. Jefferson, Water Res. 42 (2008) 1827–1845. https://doi.org/10.1016/j.watres.2007.11.039

[10] J.S. Tan, S.Y. Lee, K.W. Chew, M.K. Lam, J.W. Lim, S.H. Ho, P.L. Show, Bioengineered 11 (2020) 116–129. https://doi.org/10.1080/21655979.2020.1711626

[11] I. Kabdaşlı, I. Arslan-Alaton, T. Ölmez-Hancı, O. Tünay, Environ. Technol. Rev. 1 (2012) 2–45. https://doi.org/10.1080/21622515.2012.715390

[12] A. Alyaqoobi, J. Eng. 16 (2010) 6198–6205. https://www.iasj.net/iasj/download/68d9eca9c8fadc2b

[13] B. Fadhil, A.M. Ghalib, J. Eng. 17 (2011) 441–447. https://www.iasj.net/iasj/download/3fd1564d5c9c7a51

[14] L. Xu, F. Wang, H.Z. Li, Z.M. Hu, C. Guo, C.Z. Liu, J. Chem. Technol. Biotechnol. 85 (2010) 1504–1507. https://doi.org/10.1002/jctb.2457

[15] O. Abdelwahab, N.K. Amin, E.S.Z. El-Ashtoukhy, J. Hazard. Mater. 163 (2009) 711–716. https://doi.org/10.1016/j.jhazmat.2008.07.016

[16] X. Zhu, J. Ni, P. Lai, Water Res. 43 (2009) 4347–4355. https://doi.org/10.1016/j.watres.2009.06.030

[17] N. Uduman, V. Bourniquel, M.K. Danquah, A.F.A. Hoadley, Chem. Eng. J. 174 (2011) 249–257. https://doi.org/10.1016/j.cej.2011.09.012

[18] R. Misra, A. Guldhe, P. Singh, I. Rawat, T.A. Stenström, F. Bux, Bioresour. Technol. 176 (2015) 1–7. https://doi.org/10.1016/j.biortech.2014.11.014

[19] B.G. Ryu, J. Kim, J.I. Han, K. Kim, D. Kim, B.K. Seo, C.M. Kang, J.W. Yang, Algal Res. 31 (2018) 497–505. https://doi.org/10.1016/j.algal.2017.06.012

[20] I. Branyikova, G. Prochazkova, T. Potocar, Z. Jezkova, T. Branyik, Fermentation 4 (2018) 93. https://doi.org/10.3390/fermentation4040093

[21] R. Misra, A. Guldhe, P. Singh, I. Rawat, F. Bux, Chem. Eng. J. 255 (2014) 327–333. https://doi.org/10.1016/j.cej.2014.06.010

[22] A. Al-Yaqoobi, M. Al-Rikabey, M. Al-Mashhadani, Chem. Ind. Chem. Eng. Q. 27 (2021) 121–130. https://doi.org/10.2298/CICEQ191213031A

[23] P. Cañizares, M. Carmona, J. Lobato, F. Martínez, M.A. Rodrigo, Ind. Eng. Chem. Res. 44 (2005) 4178–4185. https://doi.org/10.1021/ie048858a

[24] A.K. Golder, A.N. Samanta, S. Ray, Sep. Purif. Technol. 53 (2007) 33–41. https://doi.org/10.1016/j.seppur.2006.06.010

[25] G. Chen, Sep. Purif. Technol. 38 (2004) 11–41. https://doi.org/10.1016/j.seppur.2003.10.006

[26] S. Gao, M. Du, J. Tian, J. Yang, J. Yang, F. Ma, J. Nan, J. Hazard. Mater. 182 (2010) 827–834. https://doi.org/10.1016/j.jhazmat.2010.06.114

[27] S. Gao, J. Yang, J. Tian, F. Ma, G. Tu, M. Du, J. Hazard. Mater. 177 (2010) 336–343. https://doi.org/10.1016/j.jhazmat.2009.12.037

[28] J. Sun, J. Wang, X. Pan, H. Yuan, Int. J. Mol. Sci. 16 (2015) 13158–13171. https://doi.org/10.3390/ijms160613158

[29] M. Valica, M. Pipíška, S. Hostin, Desalin. Water Treat. 138 (2019) 190–199. https://doi.org/10.5004/dwt.2019.23330

[30] K.P. Drees, M. Abbaszadegan, R.M. Maier, Water Res. 37 (2003) 2291–2300. https://doi.org/10.1016/S0043-1354(03)00009-5

[31] S. Monasterio, F. Dessì, M. Mascia, A. Vacca, S. Palmas, Chem. Eng. Trans. 41 (2014) 163–168. https://doi.org/10.3303/CET1441028

[32] D. Vandamme, S.C.V. Pontes, K. Goiris, I. Foubert, L.J.J. Pinoy, K. Muylaert, Biotechnol. Bioeng. 108 (2011) 2320–2329. https://doi.org/10.1002/bit.23199

[33] G. Mouedhen, M. Feki, M.D.P. Wery, H.F. Ayedi, J. Hazard. Mater. 150 (2008) 124–135. https://doi.org/10.1016/j.jhazmat.2007.04.090

[34] P. Cañizares, F. Martínez, C. Jiménez, C. Sáez, M.A. Rodrigo, J. Hazard. Mater. 151 (2008) 44–51. https://doi.org/10.1016/j.jhazmat.2007.05.043

[35] A. Aitbara, M. Cherifi, S. Hazourli, J.P. Leclerc, Desalin. Water Treat. 57 (2016) 3395–3404. https://doi.org/10.1080/19443994.2014.989411

[36] B. Zeboudji, N. Drouiche, H. Lounici, N. Mameri, N. Ghaffour, Sep. Sci. Technol. 48 (2013) 1280–1288. https://doi.org/10.1080/01496395.2012.731125

[37] A. Mohammed, M. Al-Mureeb, J. Eng. 16 (2010) 5811–5821.https://www.iasj.net/iasj/download/a5123fae2ba58b93

ATHEER M. AL-YAQOOBI[1]
MUNA N. AL-RIKABEY[2]

[1]Department of Chemical Engineering, College of Engineering, University of Baghdad, Iraq

[2]Department of Biochemical Engineering, Al-Khwarizmi College of Engineering, University of Baghdad, Iraq

NAUČNI RAD

ELEKTROHEMIJSKO IZDVAJANJE *CHLORELLA* SP.: KONCENTRACIJA ELEKTROLITA I MEĐUELEKTRODNA UDALJENOST

U ovom radu su istraživana dva načina elektrohemijskog izdvajanja mikroalgi. Žrtvena anoda (aluminijum) je korišćena za proučavanje procesa elektrokoagulacije i flotacije, a nežrtvena anoda (grafit) za istraživanje procesa elektroflotacije. Istražen je uticaj koncentracije hloridnih jona i međuelektrodnog rastojanja na performanse procesa elektrohemijskog izdvajanja. Rezultati su pokazali da su obe elektrode postigle maksimalnu efikasnost izdvajanja sa koncentracijom NaCl od 2g/l. Povećanjem koncentracije NaCl na 5 g/l, efikasnost izdvajanja je dramatično smanjena na najnižu vrednost. Generalno, potrošnja energije opada sa povećanjem koncentracije NaCl. Štaviše, potrošnja energije postignuta sa aluminijumskim anodama je niža od one koja se postiže sa grafitnim. Međutim, povećanjem razmaka između elektroda sa 15 mm na 30 mm, vreme potrebno za postizanje maksimalne efikasnosti se udvostručilo, a samim tim je povećana potrošnja energije.

Ključne reči: elektrohemijsko izdvajanje, elektrokoagulacija, Chlorella sp., nežrtvena elektroda, potrošnja energije.

ANA PAULA R. PAIVA[1]
RAFAEL O. SANTOS[2]
MÔNICA P. MAIA[1]
DIEGO M. PRATA[1]

[1]Department of Chemical and Petroleum Engineering, Universidade Federal Fluminense, Niterói, RJ, Brazil

[2]Chemical Engineering Program, COPPE, Universidade Federal do Rio de Janeiro, Rio de Janeiro, RJ, Brazil

IMPROVEMENT OF THE MONOCHLOROBENZENE SEPARATION PROCESS THROUGH HEAT INTEGRATION: A SUSTAINABILITY-BASED ASSESSMENT

Article Highlights
- Design and simulation of improved monochlorobenzene separation process through heat integration
- Design and simulation of utility plants for more realistic results
- Analysis in terms of water consumption, CO_2 emission, and utility costs
- An eco-efficiency comparison between the original and improved process
- Heat integrated process provides a 25% increase in eco-efficiency for the MCB process

Abstract

Chlorobenzene is an important chemical intermediate in the production of commodities, such as herbicides, dyestuffs, and rubber. In this work, a heat integration was proposed for a monochlorobenzene separation process. The conventional process structure and the proposed integrated one were designed and simulated. An optimization focused on minimizing the cooling and heating costs was performed to obtain the best-operating conditions for the heat integration. The simulation of a utility plant, including cooling water and steam generation sections, was also carried out for more accurate estimations of CO_2 emissions, water, energy consumption, and operating costs. The processes were evaluated and compared in terms of their sustainable performances using the eco-efficiency comparison index method and environmental and economic indicators, such as CO_2 emission, water consumption, and utility cost, to assess the benefits of heat integration. The results demonstrated that the proposed strategy reduced around 57% of all environmental impacts and utility costs. As the composite evaluation index from the performance indicators showed, the proposed optimal heat integrated industrial plant significantly improved the initial processes' eco-efficiencies, up to 83%, proving a suitable strategy for a more sustainable process.

Keywords: eco-efficiency, heat integration, monochlorobenzene, process simulation, sustainability indicators, utility plants.

In recent years, the impacts of rapid industrialization, economic competition, and rising energy demands, coupled with natural resource depletion and population growth, have been receiving

attention globally from researchers, government, and economic agents, which shows that society has become more conscious about the ecosystem equilibrium. In this context, regulations, incentives, and goals have been discussed and proposed, such as the 2030 Agenda developed by the United Nations [1]. As part of the agenda, Sustainable Development Goals (SDGs) have been established as key goals for social, economic, and environmentally friendly development.

In this scenario, industries have evaluated their processes and performed improvement actions to reduce operating costs, risks, raw material consump-

tion, and environmental impacts. Considering this last aspect, impacts, such as water and energy demand, greenhouse gas emissions, and wastewater generation, must be rigorously analyzed, specifically for the conceptual phase of the new process designs. Furthermore, increasing the efficiency of water and raw materials usage is also important to minimize industrial plant wastewater and solid residues.

Chemical products from biochemical and petrochemical industrial plants represent an important role in society [2]. These processes are mainly composed of raw materials extraction or conversion into the desired products, usually called the transformation industry. However, unconsumed raw materials and undesired subproducts can be found as a byproduct of these industrial processes, caused by the global conversion being less than 100%.

For these motives, purification and separation equipment, such as distillation columns, must obtain the main products at the desired commercial purity and recycle unreacted feedstock, increasing the overall process efficiency. Multiple conventional industrial plants employ these techniques: for example, the synthesis of methanol [3], butyl acetate [4], biodiesel [5], cumene [6], ethylbenzene [7], and maleic anhydride [8] addition, and purification processes focused on reutilization, such as the purification of acetic acid [9] and toluene-benzene, are also found in conventional industry. These processes have lower costs since the feedstocks are mixed with other contaminants. Nonetheless, the production costs should be further reduced to make the purified products more competitive.

Based on the concepts of sustainable development, improvement actions to increase the ecoefficiency of these processes are necessary. Many strategies can be performed to achieve this goal. For example, replacing the feedstock for ones with renewable sources, such as the use of biogas in energy generation and methanol synthesis [3,10], and the use of soy oil for biodiesel production [5], replacing a catalyst for another with greater efficiency in conversion and selectivity, as used in newer propylene polymerization plants [11], heat integration [4], single and multi-objective process optimization [5], and the development of process intensification techniques: reactive, double effect and dividing wall distillation [6,7,9,12], including membrane reactors [10].

The use of process simulation as a conceptual design and decision-making tool has been growing in recent years [12,13]. Process simulation is a mathematical model that provides the state of a determined system by numeric solution, starting from previously specified conditions: components, parameters, equipment sizing, flow rate, composition,

pressure, temperature, and other operating conditions. Furthermore, to quantitatively evaluate the benefits of the chosen decision, indicators are commonly used to translate into metrics the economic, safety, and environmental aspects [12].

Thus, this work proposes a novel heat integration for the monochlorobenzene (MCB) separation process to reduce the environmental impacts and operating costs. The conventional and modified processes were simulated to evaluate this proposed concept. Also, eco-indicators were utilized to measure the change in water consumption, CO_2 emissions, and utility costs. The simulation of a utility plant, including cooling water and steam generation sections, was also carried out to achieve more realistic scenarios for water losses and energetic demand. Furthermore, a comparison between both processes was developed based on the eco-efficiency comparison index method to assess if the proposed modification achieves the goal of turning the process towards a more sustainable path.

MATERIAL AND METHODS

Process description

MCB separation process

Monochlorobenzene is an important chemical utilized as an intermediate in a diverse range of sectors such as the production of pesticides, herbicides, adhesives, repellents, degreasers, and pharmaceutical compounds. As a solvent, it has a high boiling point, resulting from the benzene (BEN) chlorination reaction, their main synthesis route. Benzene, an aromatic hydrocarbon, is used to synthesize aniline, cyclohexane, cumene, and mainly ethylbenzene, representing over 50% of benzene demand. In addition, benzene is primarily used in the production of styrene [14], although it can also be used as a fuel additive and a solvent. Both BEN and MCB are insoluble in water and are highly volatile.

In the synthesis process of MCB, residual gases containing both MCB and benzene are released and are primarily connected to a number of contamination cases by inhalation [14]. MCB is also one of the main organic contaminants in soil, sediments, groundwater, and superficial water [15]. Benzene is also commonly found as a contaminant in soil and groundwater due to fuel storage tank leakage [16]. Both compounds are carcinogenic, mutagenic, and have a high potential for bioaccumulation, thus representing a high risk to health and ecosystems. Therefore, the MCB process directly impacts society and the environment.

The chlorination reaction of benzene occurs in the liquid phase at atmospheric pressure, over a temperature range between 27 °C and 37 °C, using iron chloride ($FeCl_3$) as a catalyst, as described by Eq. (1)

.

$$C_6H_6 + Cl_2 \rightarrow C_6H_5Cl + HCl \qquad \qquad (1)$$

The synthesis section of MCB produces a gaseous mixture composed of MCB, benzene, and hydrochloric acid. After scrubbing the hydrochloric acid from the product stream, a distillation unit is needed to separate the chlorobenzene from the benzene. It is important to guarantee that no acid is entering the distillation columns because this contaminant has high corrosivity and will harm the structure of the columns. The MCB separation process flowsheet, based on the works of Seider *et al.* [17], is described in Fig.1. The feed stream from the synthesis section consists mainly of MCB and benzene, with small amounts of HCl. This stream is heated in the HX1 by medium pressure steam and sent to the first flash separator F1. Next, the gas stream from the separator is sent to an absorber column A1, while the liquid is mixed with the bottom product of the absorber. The absorber A1 function removes the hydrochloric acid that persists inside the MCB process. The column is composed of 15 trays but only three theoretical stages. At the top of the absorber, HCl is removed with a purity of 95%, which can be recycled and used in the synthesis section. The upper stage of the absorber also receives a part of the bottom product of the distillation column D1. The mixture stream of the flash separator and the bottom product of the absorber still contains small amounts of HCl, which needs to be removed before the distillation column. For this reason, the stream is sent to a stripper unit T1, where the HCl is collected at the bottom of the treatment unit, and the acid-free stream is then sent to the distillation column. The column D1 is responsible for the separation of MCB from benzene. It has 30 trays corresponding to 20 theoretical stages, and the feed stream enters the column at the tenth stage. The benzene is produced in the distillate with a purity of 99.75%. The bottom product of the column is further cooled down before a fraction of the stream is recycled to the absorber. The product stream, composed of 99.999% of MCB, is represented by the stream S14.
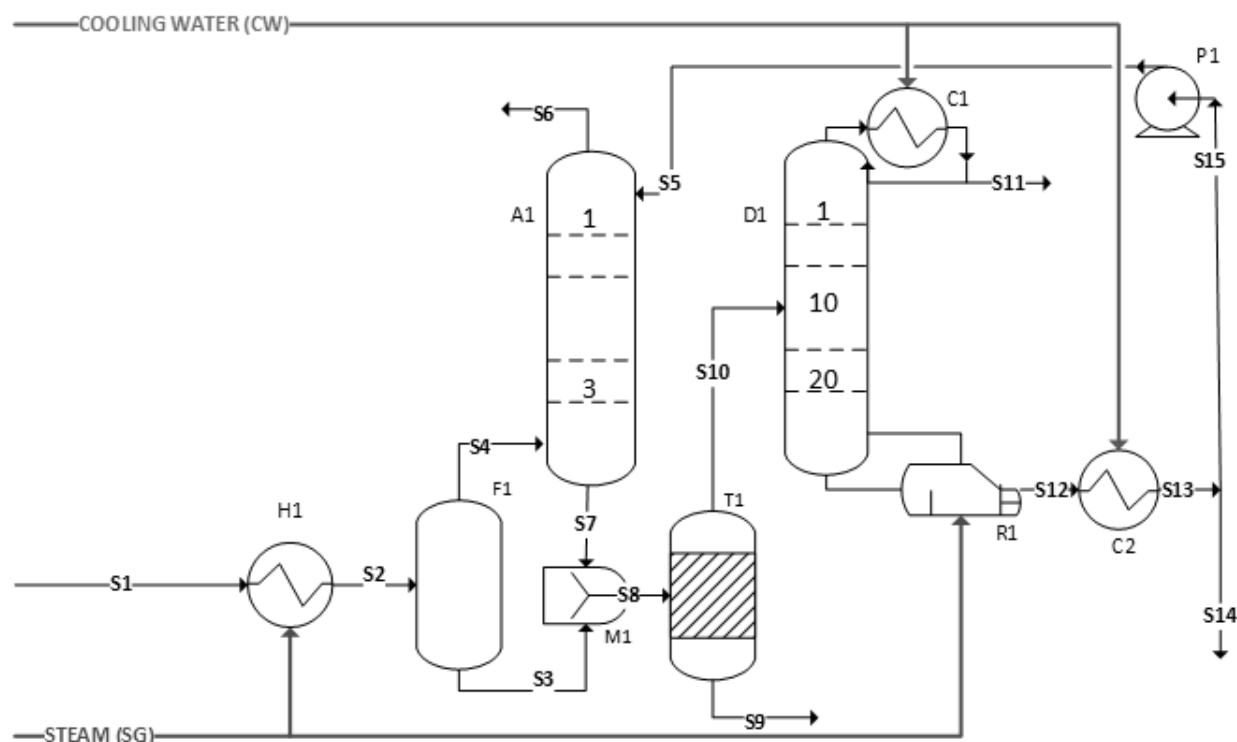
Figure 1. MCB separation process flowsheet.

Modified MCB separation process

The novel MCB separation process flowsheet, developed using heat integration concepts, is described in Fig.2. In the conventional process, the bottom product leaves the distillation columns at a high temperature, around 153 °C, and is cooled down until it reaches a temperature of 49 °C. Furthermore, the process feed stream is heated from 27 °C to 132 °C before being sent to the flash vessel. Based on these properties, a heat integration is proposed using these two streams. The FEHE, the feed effluent heat exchanger, harnesses the energy from the distillation column bottom product to heat the process feed stream, thus lowering the energetic demand for the heater H1 and the cooler C2.

Utility plant

The utility plant supplies auxiliary services such
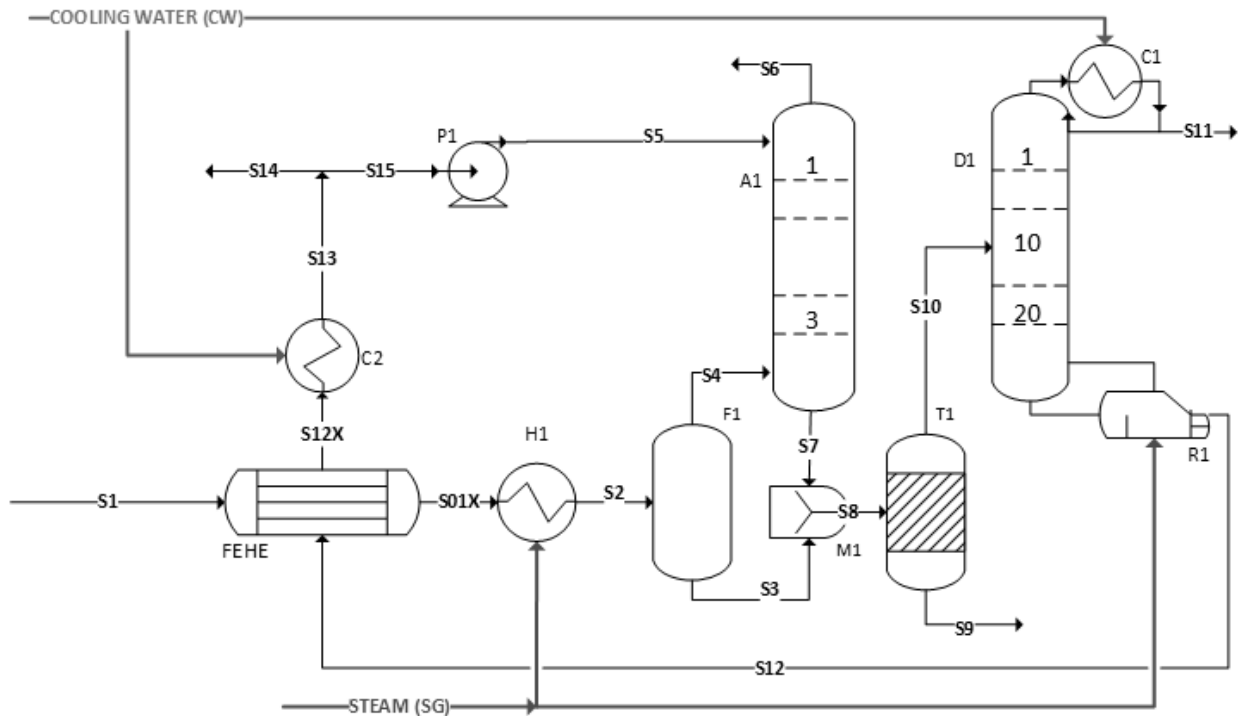
Figure 2. Modified MCB process flowsheet.

as electricity (by cogeneration), cooling water, steam, compressed air-fuel, and other necessary services for the operation of chemical process plants. Through simulations based on heuristics for water losses and equipment duties for this system, it is possible to obtain more realistic and trustworthy results for the total water and energy consumption of the process and, consequently, better estimate the CO_2 emissions and wastewater produced.

The utility plant modeled in this work is based on the system described by Turton *et al.* [18], and its flowsheet is illustrated in Fig.3. The energy cogeneration substation was not considered for the utility system. The water that returns from the cooling process is sent to the cooling tower in the cooling water section. The tower operates with an induced draft system, cooling the water to the desired temperature. A part of the water is lost by drift and another by windage. Furthermore, a blowdown must be done to avoid the accumulation of solids inside the utility plant. The fresh cooling water is then pressurized and recirculated into the cooling system.

In the steam generation section, fresh water passes through a pre-treatment unit composed of ion exchanger absorption beds and solid filters. Then, the treated water is sent to the deaerator, which is mixed with the returning condensate from the heating process. The water stream that comes from the deaerator is known as the boiler feeding water (BFW). Finally, the BFW is pressurized to the desired saturated

steam pressure level and sent to the boiler.

The boiler heating can be divided into two sectors: the first sector, B1, represents the sensible heat exchange, which raises the pressurized water's temperature until the boiling point. The second sector B2 represents the latent heat needed to transform the liquid water into steam, which is then sent to the heating system. Like the cooling section, a blowdown must be done to avoid the accumulation of solids inside the utility system and reduce corrosion and water drift. Besides the boiler blowdown, water losses from the pre-treatment, the deaerator, and the process heating system must also be accounted for.

A makeup water stream is utilized to replenish the total water lost over the operation of the utility plants so that the system can continuously operate. The whole makeup water flow rate (m_{total}) is the sum of the flow rates for the cooling water section (m_{CW}) and steam generation section (m_{SG}). Moreover, Liew *et al.* [19] noted the importance of not neglecting the boiler-sensible heat in the process simulation since this can represent an estimation error of over 18% energy consumption.

Methodology

Process simulation

The MCB separation process plant and its utility plant were simulated using the Honeywell Unisim Design Suite. Both simulations were carried out in steady-state. For the conventional MCB process, the

PAIVA *et al.*: IMPROVEMENT OF THE MONOCHLOROBENZENE....

Chem. Ind. Chem. Eng. Q. 29 (1) 31−42 (2023)
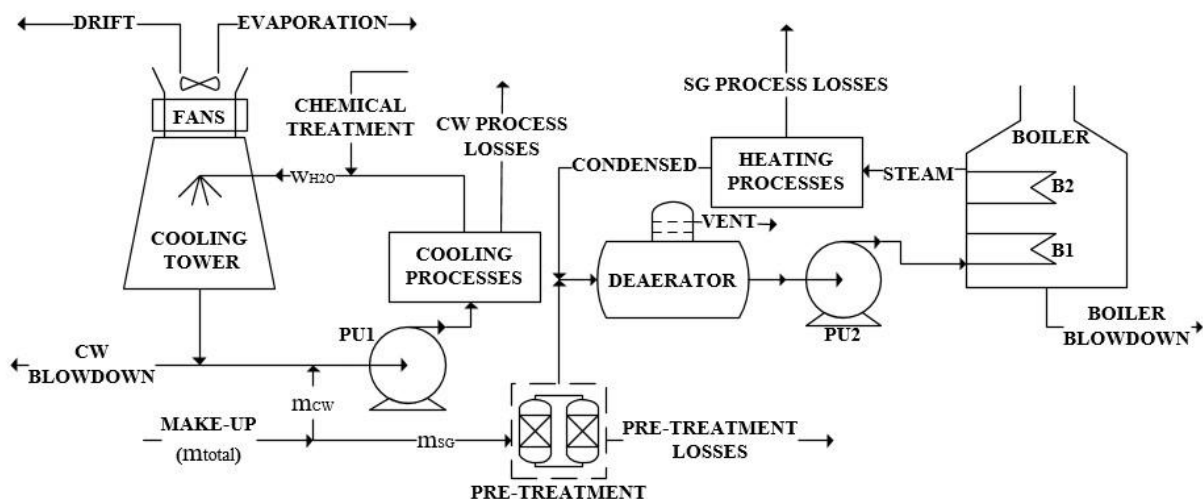
Figure 3. Utility plant flowsheet.

process configuration, main equipment, column specifications, operational conditions, and other parameters were implemented following the data provided by Seider *et al.* [17], to validate our simulation with existing literature data. In addition, the Wilson thermodynamic package was used for the simulation to correctly compare the present results with the reference work since the same thermodynamic model was employed. The Wilson thermodynamic package is an activity coefficient-based model recommended for non-ideal systems and thus, can better describe the phase equilibria inside the absorber and distillation column. The utility plant was simulated using the UNIQUAC thermodynamic package, as suggested by Turton *et al.* [18]. In addition, the energy duties data from the main MCB process were utilized as inputs to the utility plant model, thus obtaining more precise results.

Tables 1 and 2 summarize the heuristics for water losses and other operating, energy factors, and general

assumptions used to simulate the utility system. It is important to note that the medium pressure steam pressure was selected as the desired steam class based on the temperature data from the heaters and distillation columns.

Table 1. Water losses heuristics for the utility plant

Parameter	Water loss (%)	Reference
Cooling tower blowdown	3	[17]
Evaporation losses	2.7	[24]
Water drift losses	0.3	[17]
Cooling system losses	1	[24]
Boiler blowdown	3	[17]
BFW pre-treatment losses	1	[24]
Condensate losses	10	[18]

Note: Vent losses from the deaerator were considered negligible.

Table 2. Utilities operating conditions and assumptions

Parameter	Value	Reference
Makeup water	101.3 kPa–30 °C	[18]
Cooling water (tower inlet)	516 kPa–45 °C	[24]
Cooling water (tower outlet)	216 kPa–30 °C	[24]
Medium pressure steam (MPS)	1136 kPa–185.5 °C	[18]
Boiler efficiency	80%	[17]
Boiler fuel gas - Natural gas	100% methane	[17]
Fan efficiency	99%	Assumed
Centrifugal pumps efficiency	75%	[17]
Heat exchanger temperature approach	10 °C	[18]

According to Caxiano *et al.* [9], the cooling tower fan duties can be calculated (in GJ/h) based on the

cooling tower's circulating water volumetric flow rate by the following equation:

$$E_{fans} = w_{H_2O} \cdot 1.45222 \cdot 10^{-4} \tag{2}$$

Process simulation

The eco-efficiency is a common object of industries that aims for sustainability since the concept evaluates the relationship between the environmental impacts and the economic performance of the process, using tools that directly express this correlation called eco-indicators. According to Mangili *et al.* [13], an eco-indicator is a metric represented by the ratio between an environmental variable (energy and water consumption, CO_2 emissions, and others) and an economic variable (income or production). In this work, the production rate ($m_{production}$) was chosen for the eco-indicators.

For the evaluation of the ecoefficiency of the MCB separation process, three indicators were considered:

• Eco-indicator of water consumption, WC (m^3/t);
• Eco-indicator of CO_2 emissions, CDE (t$_{CO2}$/t);
• Specific utility cost, SUC (US$/t).

The reduction of water consumption, mitigation of greenhouse gas emissions, global climate action, and responsible production are all major objectives contained in the #6, #12, and #13 SDGs [1], which influenced the environmental indicators chosen for this study. In addition, the indicators of water consumption and CO_2 emissions (resulting emissions from fuel combustion in the boiler and the electricity consumption from the main process and the utility plant) are the most commonly used by works in the literature [13] and industrial process monitoring [20].

The chosen indicators must address the environmental consequences and the process economic performance for a more comprehensive evaluation of process ecoefficiency. As a result, the utility cost indicator was chosen as an economic indicator because it is directly related to the other metrics.

The indicators WC, CDE and SUC are defined by the Eqs. (3), (4), and (5), respectively.

$$WC = \frac{v_{H_2O, \, makeup}}{m_{production}} \tag{3}$$

$$CDE = \frac{E_{comb}\xi_{comb} + E_{ele}\xi_{ele} + m_{CO_2}}{m_{production}} \tag{4}$$

$$SUC = \frac{E_{comb}C_{NG} + E_{ele}C_{EE} + m_{total}C_{PW}}{m_{production}}$$
$$+ \frac{m_{CW}C_{CWT} + m_{SG}C_{SGT} + m_{WW}C_{WWT}}{m_{production}} \tag{5}$$

Specifications:

i. The production rate (in t/h), $m_{production}$, corresponds to the mass flow rate of stream S14 (MCB 99.9%). The streams S11 (BEN 99%), S06 (HCl 96), and S09 (HCl pure) are not considered a product stream because the benzene and HCl are recycled to the synthesis section of the MCB, which provides the feed stream of this separation process as a subproduct (fiscal tax).

ii. The $v_{H2O \, makeup}$ is the water makeup volumetric flow rate (in m$^3_{H2O}$) calculated from the sum of the water losses in the utility plant, considering both cooling water and steam generation sections;

E_{comb} and E_{ele} are, respectively, the energy by combustion consumed in the boiler and the electricity energy rate, both in GJ/h and calculated as described in Eqs. (6) and (7), where Q_{B1} and Q_{B2} correspond to the sensible and latent heat exchanged inside the boiler, respectively.

$$E_{comb} = \frac{Q_{B1} + Q_{B2}}{\eta_{comb}} \tag{6}$$

$$E_{ele} = \frac{E_{pumps}}{\eta_{pump}} + \frac{E_{fans}}{\eta_{fan}} \tag{7}$$

iv. η_{comb}, η_{pump}, and η_{fan} are the efficiencies for combustion and electric equipment (pumps and fan);

v. ξ_{comb} and ξ_{ele} are the CO_2 emission factors for direct and indirect sources: ξ_{comb} is equal to 0.0561 t$_{CO2}$/GJ, corresponding to the use of natural gas as fuel [21], and ξ_{ele} is equal to 0.0268 t$_{CO2}$/GJ [22], corresponding to the electricity use. This emission factor is based on the industrial plant locality. In this work, the emission factor corresponds to Brazil's average factor for the first semester of 2021.

vi. m_{CO2} (t$_{CO2}$/h) refers to the CO_2 emissions by fugitive sources. In this work, these emissions are considered negligible for standard operation mode (without shutting down and start-up events);

vii. The wastewater treatment cost refers to a secondary wastewater treatment facility composed of filtration and activated sludge.

viii. m_{WW} refers to the wastewater stream volumetric flow rate in m³/h. Since the water lost by drift and evaporation in the cooling water can't be recovered, these are not considered for the total stream flow rate.

ix. C_{NG}, C_{EE}, C_{PW}, C_{CWT}, C_{SGT}, and C_{WWT} refers to the utility costs described in Table 3 [18,23]. C_{NG} is the natural gas cost ($/GJ), C_{EE} is the electricity cost ($/GJ), C_{PW}, refers to the process water cost ($/m³), C_{CWT}, C_{SGT}, and C_{WWT} are the treatment costs for the cooling water, steam, and wastewater, respectively.

Table 3. Utilities cost

Utilities	Price	References
Natural Gas ($/GJ)	5.00	[23]
Electricity ($/GJ)	18.72	[18]
Process water ($/m³)	0.0157	[18]
Process water ($/GJ)	0.378	[18]
CW treatment ($/m³)	0.0347	[18]
SG treatment ($/m³)	0.1560	[18]
Wastewater treatment ($/m³)	0.0043	[18]

The ECI (Eco-efficiency Comparison Index) can be obtained from the normalized values of each indicator. These values are then plotted on a radar chart, allowing a visual representation of the performance of the processes relative to each category. The area S of each process' chart is then calculated using the Law of Sines, as described in Eq. (8), in which EI is the normalized value of each indicator and n is the total number of indicators utilized in the eco-efficiency analysis.

$$S = 0.5 \cdot \sin(2\pi/n) \cdot \left(EI_1 EI_n + \sum_{i=1}^{n-1} EI_i \cdot EI_{i+1} \right) \quad (8)$$

The ECI for the modified process is obtained by the ratio between the modified and conventional processes areas, as shown in Eq. (9), providing a quantitative metric for the eco-efficiency improvement by the heat integration [9].

$$ECI = 1 - \left(\frac{S_{modified}}{S_{conventional}} \right) \quad (9)$$

An optimization study was developed for the modified MCB separation process to obtain the best-operating conditions to minimize the heating and cooling costs. A preliminary analysis of the operating parameters was done to select the variables to be manipulated in the optimization. The temperature of the streams S01X, S02, S13, and the recycle ratio were the parameters suitable for optimization and chosen as decision variables. The optimization problem can be defined as:

$$\min_x F_{OBJ}(x) = C_{NG}(Q_{HEATER} + Q_{REBOILER}) + C_{PW}(Q_{COOLER} + Q_{CONDENSER}) \quad (10)$$

In which x is the decision variables vector, Q_{HEATER}, $Q_{REBOILER}$, $Q_{COOLER0}$, and $Q_{CONDENSER}$ are the heater, reboiler, cooler, and condenser duties in GJ/h, respectively, and C_{NG} and C_{PW} are the cooling and heating utility costs in $/GJ.

The optimization procedure was developed in a python environment by a multistart algorithm that utilizes the Nelder-Mead method. The optimizer interacts with the software Unisim, giving the decision variables as inputs and receiving the objective function value as output.

RESULTS AND DISCUSSION

Process and utility plant simulation

Table 4 presents the results for the process streams data of the conventional MCB separation plant, and the simulation flowsheet is illustrated in Fig.4.

Table 4. MCB Conventional process results

Process stream	Temperature (°F)	Pressure (psia)	Molar flow (lbmol/h)	Molar Fraction		
				MCB	Benzene	HCl
S1	80	37	50	0.5000	0.4000	0.1000
S11	207	25	0.1	0.0025	0.9975	0.0000
S14	120	25	49	0.9999	0.0000	0.0000

The simulation was validated by comparing the results obtained for the simulation with the data from Seider *et al.* [17]. The results were consistent with those from the base work, without any significant errors.

Figure 5 illustrates the modified MCB separation process simulation flowsheet. The results obtained for the optimized product streams, related to the mass flow rate and compositions, were the same as the conventional process.

Table 5 describes the energetic demand for the conventional original process (OP) and the modified heat-integrated process (HIP), including the main equipment and the duties of the utility plant.

Heat integration can reduce the energy demand of the cooler by up to 85%, the condenser by 52%, and the reboiler by 42%. Furthermore, the optimal conditions eliminate the need for the heater H1. As a result, the optimal duties lead to a total heating/cooling cost of 17.43 $/h, reducing more than 53% of the base case cost (36.59 $/h). Thus, the proposed modification
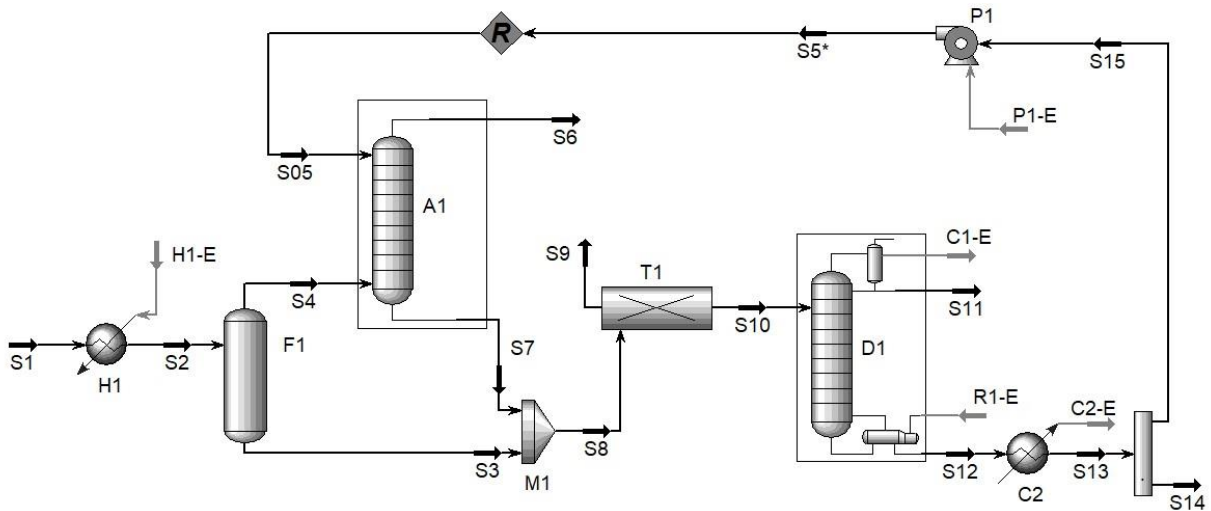
Figure 4. MCB conventional process simulation flowsheet.
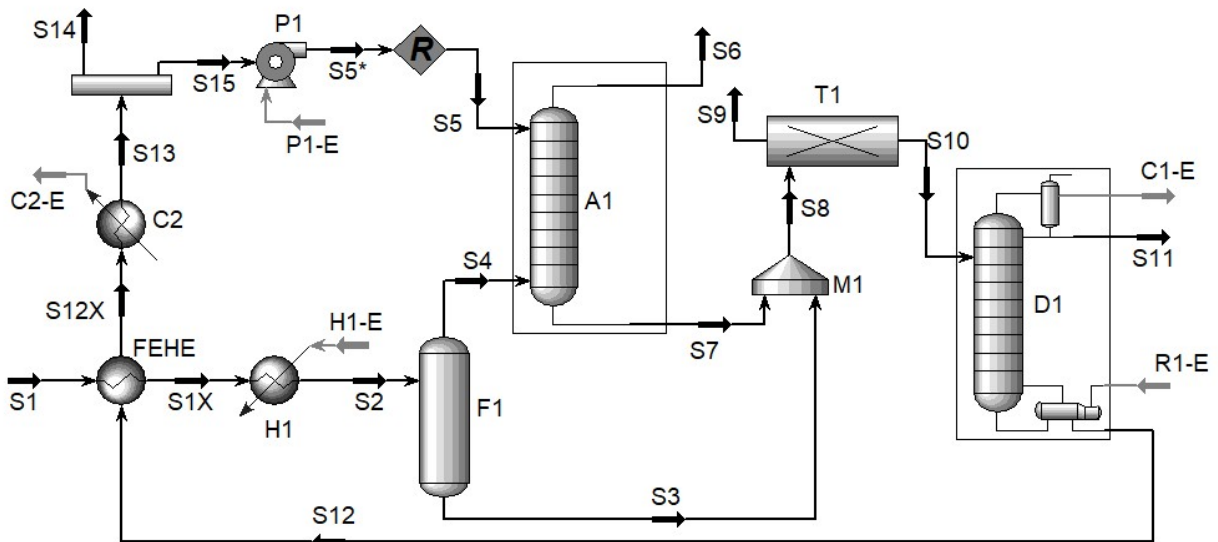
Figure 5. Modified MCB process simulation flowsheet.

achieves the goal of lowering heating and cooling demand.

The energetic duties of electricity-based equipment are significantly lower than the steam-based ones. Consequently, the CO_2 emissions are composed of a large factor of the emissions from the fuel combustion inside the boiler, as shown in Fig. 6.

The difference in scale between the emission sources shows the importance of choosing the right steam class for the process heating based on the operating temperature since it influences both latent and sensible heat portions of the boiler heat demand and, in turn, the process total gases emissions. Furthermore, the sensible heat section of the boiler composes around 17% of the boiler heating duty, in accordance with the results of 18% described by Liew

et al. [19]. This part of the heat duty, commonly disregarded in other simulation works in the literature, can greatly affect the process energy profile. Changing the reboiler operating temperature, for example, can shift the necessary steam pressure class, allowing further manipulation of the total energy consumption. For example, the heat duties of the reboiler R1 is responsible for 37% and 53% of the process energy demand in the conventional and heat-integrated process, respectively.

The results for the water consumption and water losses of each process obtained from the utility plant data are presented in Table 6.

As the total circulating water in the cooling water section is significantly larger than the steam generation section, the water losses from the cooling water plant

Table 5. Energy duties summary

Source	Duty (GJ/h)		Reduction
	OP	HIP	(%)
Main plant			
Condenser C1	3.09	1.50	51.45
Cooler C2	1.20	0.18	84.59
Heater H1	1.23	0.00	100.00
Reboiler R1	3.35	3.35	41.18
Pump P1	3.04E-4	4.12E-5	86.47
Utility plant			
Pump PU1	0.036	0.014	61.11
Pump PU2	0.003	0.001	66.67
Cooling tower fans	0.010	0.004	60.00
Boiler B1 (sensible heat)	1.194	0.514	56.98
Boiler B2 (latent heat)[a]	5.718	2.461	56.96
Cooling utilities	4.290	1.690	60.61
Heating utilities	6.912	2.974	56.97
Electricity consumption	0.050	0.020	60
Total energy consumption	11.252	4.684	58.37

[a] The boiler latent heat corresponds to the steam demand from the heater H1 and reboiler H1.
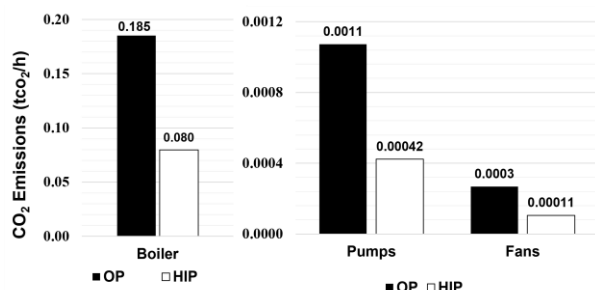
Figure 6. CO_2 emissions for the conventional (OP) and modified process (HIP).

Table 6. Water consumption results

Parameter	Flow rate (m³/h)	
	OP	HIP
Cooling water losses	0.687	0.270
Cooling tower blowdown	1.978	0.778
Evaporation and drift losses	2.039	0.802
Boiler blowdown	0.071	0.031
Steam Generation losses	0.230	0.099
Treatment losses	0.003	0.001
Total water consumption	5.008	1.980

are the main component of the water consumption for both processes. As a result, the cooling water make-up stream represents over 93% of the total water consumption for the conventional and the modified processes.

The specific utility costs depend on both energy and water consumption. The lower heat duties attained from the heat integration cause a 57% lower cost for the modified MCB process than the conventional one. The utilities cost profiles for each process are shown in Fig. 7.
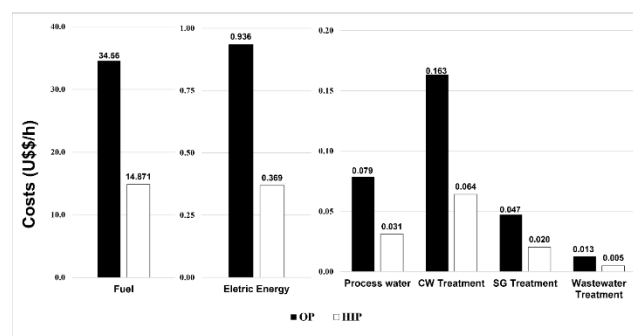
Figure 7. Breakdown of utility cost.

The fuel consumed in the boiler is the main component of the utility cost. However, the combined costs from electricity, wastewater, and water consumption represent lower than 4% of the costs for both processes. Hence, reducing the steam demand from the boiler provoked by the heat integration is responsible for the lower SUC.

Eco-indicators and ecoefficiency

The values of the indicators of water consumption, CO_2 emissions, and specific utility costs calculated for both MCB separation processes, coupled with the percentual reduction obtained by the heat integration, are shown in Table 7.

The indicators of the modified process are around 60% lower than those of the conventional plant. In accordance with the lower heat duties achieved for coolers and heaters, the heat integration provided a significant reduction of the environmental impacts of the MCB separation process.

The water consumption eco-indicator is lower than 2 m³/t of product, a low value considering that the circulating water in the cooling tower has a value of 68 m³/h for the conventional process and 27 m³/h for the modified one. These flow rates are also lower than 4500 m³/h, the maximum limit of the economic viability of a cooling system, as presented by Couper *et al.* [24].

Table 8 describes the results obtained for calculating the ECI from the normalized values of the indicators, and Figure 8 shows the radar charts elaborated for these indicators.

Table 7. Eco-indicators results

	Eco-indicators		Normalized indicators		Reduction (%)
	OP	HIP	OP	HIP	
WC (m^3/t$_{product}$)	1.977	0.781	1.000	0.430	60.47
CDE (t$_{CO2}$/t$_{product}$)	0.143	0.066	1.000	0.395	56.98
UC (U$$/t$_{product}$)	14.128	6.062	1.000	0.429	57.09

Table 8. ECI results

Eco-indicator x Eco-indicator	OP	HIP
CDE x WC	1.000	0.170
WC x UC	1.000	0.170
UC x CDE	1.000	0.185
Total	3.000	0.524
Chart area	1.299	0.227
ECI	0.0%	82.5%
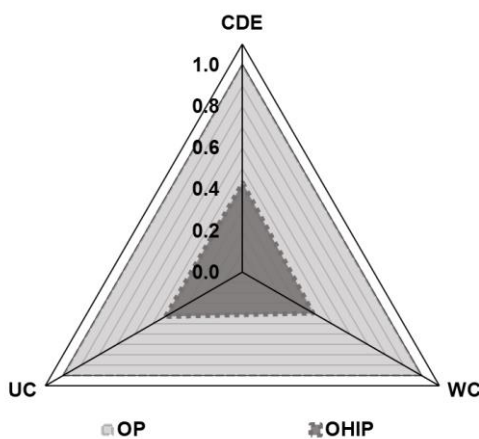
Figure 8. ECI radar chart for the MCB separation processes.

The ECI values, calculated from the chart areas, demonstrate that the heat-integrated process is 83% more eco-efficient than the conventional process. It corroborates the importance of heat integration in developing a more sustainable process. As no data was found for the indicators in previous works on the MCB-benzene separation process, it is believed that this work can hopefully provide a framework for reference for future analysis of the monochlorobenzene separation in the literature.

CONCLUSION

This study proposed a heat integration strategy for monochlorobenzene separation process to increase sustainability performance compared to the original process presented in Seider *et al*. [14]'s work. Both processes were designed via computer simulation based on process data provided in the reference work and a utility plant simulation for more accurate estimations of water and energy consumption and, consequently, the CO_2 emissions.

The optimal heat integrated process reduced over 57% of the utility cost, thus significantly increasing the process' economic performance. Furthermore, the modified configuration, composed of changes to recycle ratio and heat exchangers' temperatures, removes the necessity of a heater before the absorber column.

Results showed that the proposed design provided 60% and 57% lower water and energy consumption and around 57% lower CO_2 emissions than the original process. These lower indicators align with SDGs #6, #12, and #13 of the 2030 Agenda [1]. Thus, the optimal heat integrated design provided an 83% increase in its eco-efficiency compared to the original process.

The results of this work demonstrate the potential of the process heat integration strategy in reducing environmental impacts and improving economic performance. These findings can also help engineers weigh the economy against the environmental impacts for selecting the suitable process intensification. Future works should also consider process intensification studies on distillation columns (vapor recompression, double-effect distillation, etc.) to further increase the eco-efficiency performance.

NOMENCLATURE

BEN	Benzene
BFW	Boiler feeding water
C$_{CWT}$	Treatment costs for the cooling water
CDE	Eco-indicator of CO_2 emissions
C$_{EE}$	Electricity cost

C_{NG}	Natural gas cost
C_{PW}	Process water cost
C_{SGT}	Treatment costs for steam
C_{WWT}	Treatment costs for wastewater
ECI	Eco-efficiency Comparison Index
E_{comb}	Energy by combustion consumed in the boiler
E_{ele}	Electricity energy rate
E_{fans}	Cooling tower fan duties
EI	Normalized value of each indicator
$FEHE$	Feed effluent heat exchanger
$Fobj$	Objective function
HIP	Process through heat integration
MCB	Monochlorobenzene
m_{CO2}	CO_2 emissions by fugitive sources
$m_{CW}\neg$	Flow rate of the cooling water section
$m_{production}$	Production rate
$m_{production}$	Sum of the mass flow rates of streams S06, S09, and S14
m_{SG}	Flow rate of the steam generation section
$v_{H2O,makeup}$	Sum of the makeup flow rates for the cooling water and steam generation sections of the utility plant
m_{WW}	Wastewater stream volumetric flow rate
N	Total number of indicators utilized in the eco-efficiency analysis
OP	Original process
Q_{B1}	Sensible heat exchanged inside the boiler
Q_{B2}	Latent heat exchanged inside the boiler
Q_{COOLER}	Cooler duty
$Q_{CONDENSER}$	Condenser duty
Q_{HEATER}	Heater duty
$Q_{REBOILER}$	Reboiler duty
S	Area of each process' chart
$S_{conventional}$	Conventional process area of ECI chart
$SDGs$	Sustainable Development Goals
$S_{modified}$	Modified process area of ECI chart
SUC	Specific utility cost
WC	Eco-indicator of water consumption
x	Decision variables vector
w_{H2O}	Circulating water volumetric flow rate of the cooling tower
η_{comb}	Combustion equipment efficiency
η_{fan}	Fans efficiency
η_{pump}	Pumps efficiency
ξ_{comb}	CO_2 emission factor for combustion using natural gas as fuel
ξ_{ele}	CO_2 emission factor for electricity

REFERENCES

[1] United Nations. Transforming Our World: the 2030 Agenda for Sustainable Development (2015), sdgs.un.org/2030agenda [accessed 14 March 2022].

[2] A.J. Tula, M. Eden, R. Gani, AIChE J. 66 (2019) 16819. https://doi.org/10.1002/aic.16819

[3] R.O. Santos, L.S. Santos, D.M. Prata, J. Cleaner Prod. 186 (2018) 821–830. https://doi.org/10.1016/j.jclepro.2018.03.108

[4] P.V. Mangili, D.M. Prata, Chem. Eng. Process. 135 (2019) 93–107. https://doi.org/10.1016/j.cep.2018.11.020

[5] P.C. Gonçalves, L.P.C. Monteiro, L.S. Santos, J. Cleaner Prod. 270 (2020) 122322. https://doi.org/10.1016/j.jclepro.2020.122322

[6] P.G. Junqueira, P.V. Mangili, R.O. Santos, L.S. Santos, D.M. Prata, Chem. Eng. Process. 130 (2018) 309–325. https://doi.org/10.1016/j.cep.2018.06.010

[7] P.G. Junqueira, I.N. Caxiano, P.V. Mangili, D.M. Prata, Comput. Chem. Eng. 136 (2020) 106783. https://doi.org/10.1016/j.compchemeng.2020.106783

[8] P.V. Mangili, D.M. Prata, Chem. Eng. Sci. 212 (2020) 115313. https://doi.org/10.1016/j.ces.2019.115313

[9] I.N. Caxiano, P.G. Junqueira, P.V. Mangili, D.M. Prata, Chem. Eng. Process. 147 (2020) 107784. https://doi.org/10.1016/j.cep.2019.107784

[10] H.N.C. da Silva, D.M. Prata, L.P. Zotes, L.V. Mattos, J. Cleaner. Prod. 200 (2018) 598–608. https://doi.org/10.1016/j.jclepro.2018.07.120

[11] D.M. Prata, E.L. Lima, J.C. Pinto, Macromol. Symp. 271 (2008) 26–37. https://doi.org/10.1002/masy.200851104

[12] S. Sitter, Q. Chen, I.E. Grossmann, Curr. Opin. Chem. Eng. 25 (2019) 87–94. https://doi.org/10.1016/j.coche.2018.12.006

[13] P.V. Mangili, L.S. Santos, D.M. Prata, Comput. Chem. Eng. 130 (2019) 106558. https://doi.org/10.1016/j.compchemeng.2019.106558

[14] S.D. Pravasi, in Encyclopedia of Toxicology, P. Wexler Ed., Elsevier, Amsterdam (2014), p. 870–873. eBook ISBN: 9780123864550

[15] C. Güler, in GIS and Geostatistical Techniques for Groundwater Science, Elsevier, Amsterdam (2019), p. 251–268. eBook ISBN: 9780128154144

[16] C.B. Silva, S. Mitri, T. Pavesi, E. Saggioro, J.C. Moreira, Cad. Saúde Colet. 22 (2014) 329–342. https://doi.org/10.1590/1414-462X201400040006

[17] W.D. Seider, D.R. Lewin, J.D. Seader, S. Widagdo, R. Gani, K. Ming Ng, Product and Process Design Principles: Synthesis, Analysis and Evaluation, John Wiley & Sons, West Sussex (2016), p. 784. ISBN: 978-1-119-28263-1

[18] R. Turton, R. Bailie, W.B. Whitting, J.A. Shaeiwitz, D. Bhattacharyya, Analysis, Synthesis and Design of Chemical Processes, Prentice Hall, Upper Saddle River (2018), p. 243. ISBN: 978-0-13-261812-0

[19] P.Y. Liew, S.R.W. Alwi, J.S. Lim, P.S. Varbanov, J.J. Klemes, Z.A. Manan, J. Cleaner. Prod. 77 (2014) 94–104. https://doi.org/10.1016/j.jclepro.2013.12.047

[20] C.P. Pereira, D.M. Prata, L.S. Santos, L.P.C. Monteiro, Braz. J. Chem. Eng. 35 (2018) 63–84.

https://doi.org/10.1590/0104-6632.20180351s20160370

[21]   Intergovernmental Panel on Climate Change, 2006 IPCC Guidelines for National Greenhouse Gas Inventories, www.ipcc-nggip.iges.or.jp/public/2006gl/ [accessed 3 August 2021].

[22]   Ministério da Ciência, Tecnologia, Inovações e Comunicações, Fator Médio - Inventários Corporativos, www.gov.br/mcti/pt-br/acompanhe-o-mcti/sirene/dados-e-ferramentas/fatores-de-emissao [accessed 1 August 2021].

[23]   U.S. Energy Information Administration, Henry Hub Natural Gas Spot Price, https://www.eia.gov/dnav/ng/hist/rngwhhdA.htm. [accessed 25 November 2021].

[24]   J.R. Couper, W.R. Penney, J.R. Fair, S.M. Walas, Chemical Process Equipment: Selection and Design, Butterworth-Heinemann, Oxford (2012), p. 223. ISBN: 978-0-12-396959-0.

ANA PAULA R. PAIVA[1]
RAFAEL O. SANTOS[2]
MÔNICA P. MAIA[1]
DIEGO M. PRATA[1]

[1]Department of Chemical and Petroleum Engineering, Universidade Federal Fluminense, Niterói, RJ, Brazil

[2]Chemical Engineering Program, COPPE, Universidade Federal do Rio de Janeiro, Rio de Janeiro, RJ, Brazil

NAUČNI RAD

POBOLJŠANJE PROCESA SEPARACIJE MONOHLOROBENZENA KROZ INTEGRACIJU TOPLOTE: PROCENA ZASNOVANA NA ODRŽIVOSTI

Hlorobenzen je važan hemijski intermedijer u proizvodnji herbicida, boja i guma. U ovom radu je predložena integracija toplote za proces separacije monohlorobenzena. Projektovana je i simulirana konvencionalna struktura procesa i predložena integrisana. Izvršena je optimizacija usmerena na minimiziranje troškova hlađenja i grejanja, kako bi se postigli najbolji uslovi rada za integraciju toplote. Simulacija postrojenja, uključujući sekcije za proizvodnju rashladne vode i pare, sprovedena je za preciznije procene emisije CO_2, vode, potrošnje energije i operativnih troškova. Procesi su procenjeni i upoređeni u smislu njihovih održivih performansi korišćenjem metode poređenja indeksa eko-efikasnosti i ekoloških i ekonomskih indikatora, kao što su emisija CO_2, potrošnja vode i operativni troškovi, kako bi se procenile prednosti integracije toplote. Rezultati su pokazali da je predložena strategija smanjila oko 57% svih uticaja na životnu sredinu i operativnih troškova. Kao što je pokazao kompozitni indeks evaluacije iz indikatora učinka, predloženo optimalno toplotno integrisano industrijsko postrojenje značajno je poboljšalo ekološku efikasnost početnih procesa, do 83%, dokazujući odgovarajuću strategiju za održiviji proces.

Ključne reči: ekološka efikasnost, toplotna integracija, monohlorobenzen, simulacija procesa, indikatori održivosti, postrojene.

JULIETA L. CERIONI[1,2]
MARIA E.VALLEJOS[3]
FERNANDO E. FELISSIA[3]
MARÍA C. AREA[3]
NORA N. NICHIO[1,2]
GERARDO F. SANTORI[1,2]

[1]CINDECA, Facultad de Ciencias Exactas, Universidad Nacional de La Plata. CCT La Plata- CONICET, Argentina

[2]Facultad de Ingeniería, Universidad Nacional de La Plata, La Plata, Argentina

[3]IMAM, UNaM, CONICET, FCEQYN, Programa de Celulosa y Papel (PROCYP), Félix de Azara, Posadas, Misiones, Argentina

SCIENTIFIC PAPER

UDC 633.2:633.63:66:66.094

OBTAINING XYLITOL BY HYDROLYSIS-HYDROGENATION OF LIQUORS DERIVED FROM SUGARCANE BAGASSE

Article Highlights
- Acid hydrolysis was carried out using an RCT275 sulfonated resin and sulfuric acid as reference
- RCT275 was suitable for hydrolysis, avoiding the presence of sulfur traces in liquors
- The maximum xylose yield was 82% using the RCT275 under mild conditions
- Ni/γ-Al$_2$O$_3$ reached total xylose conversion with selectivity towards xylitol of 100%
- RCT275 and Ni/γ-Al$_2$O$_3$ can be easily separated and reused in several reaction cycles

Abstract

This work presents the study of heterogeneous catalysis of sugarcane bagasse hydrothermal treatment spent liquors using a sulfonated resin. Besides, results were compared with those obtained by a conventional route using sulfuric acid as a homogeneous catalyst. Heterogeneous catalysis is suitable for the hydrolysis of sugarcane bagasse hydrothermal liquors under mild conditions (100 °C and 6 h). The obtained maximum xylose yield was 82% due to furfural formation, which causes a xylose selectivity drop. The hydrogenation of this xylose-rich liquor at 100 °C and 3 MPa of hydrogen pressure employing a supported Ni/γ-Al$_2$O$_3$ produced the total conversion of xylose with a selectivity towards xylitol of 100% by using a catalyst to xylose mass ratio of 0.5. Heterogeneous catalysis in a two-step route (hydrolysis and hydrogenation) constitutes an outstanding alternative to producing xylitol from sugarcane bagasse hydrothermal spent liquors since materials can be easily separated and reused in several reaction cycles.

Keywords: sugarcane bagasse, hydrolysis, hydrogenation, xylose, xylitol.

Lignocellulosic materials constitute one of the most abundant biomass residues, which have recently gained interest. Its use as a raw material in biorefineries would allow obtaining fuels, energy, and high added-value bio-products [1-3]. These materials can come from agricultural residues, such as rice husk, corn stubble, and sugarcane bagasse, and have the advantage of not requiring extra resources such as water, land, or energy to be produced. In 2018, global sugarcane production was approximately 1.9 billion tons. About 40% of the world's sugarcane was produced in South America (about 0.8 billion tons in 2018) [4]. Sugarcane bagasse is a renewable and abundant lignocellulosic waste with a high xylans content, which gives it enormous potential industrial with a wide range of applications. The amount of bagasse obtained from sugarcane depends on the fiber content, the cane variety, the plants' physiological state, and the technology available for harvesting [3,5]. Generally, about 30% of the ground cane is transformed into bagasse, which is composed of cellulose (35–43%), lignin (21–23%), hemicelluloses (25–32%), and soluble organic and inorganic compounds called extractives (2–11%), [3,5].

The structural complexity of lignocellulosic materials requires a pretreatment to fractionate their

major components [3,6,7]. Autohydrolysis in an aqueous medium as pretreatment allows the disaggregation of lignin-carbohydrate complexes, altering the physical properties of the fiber and facilitating the extraction of hemicelluloses [3,6,8]. The protons generated by the autoionization of water catalyze the hydrolysis of hemicelluloses, producing acetic acid as a by-product. Then, the acid medium allows the generation of oligosaccharides and monosaccharides. Lignin is also degraded and causes a sharp increase in hydroxyphenyl compounds [3,9]. Depending on the raw material and used conditions, about two-thirds of lignin and one-quarter of cellulose can be dissolved at this stage [8]. The soluble fraction, rich in hemicelluloses (liquor), is separated from the solid residue composed of cellulose and lignin at the end of the autohydrolysis.

The next stage of liquor treatment is homogeneous hydrolysis, which aims to extract the component sugars from the hemicelluloses. Generally, it is carried out in the presence of acids (H_2SO_4, HCl, H_3PO_4, organic acids) or alkalis (NaOH, $Ca(OH)_2$, KOH, hydrazine, NH_3). Among these options, treatment with H_2SO_4 (0.4–4 wt.%) at high temperatures (120–200°C) is one of the most widely used since it allows recovery of 80–90% of the sugars from hemicelluloses but presents the disadvantage of causing the degradation of sugars to furfural and HMF, phenolic acids and aldehydes, levulinic acid and other aliphatic compounds [8,10,11]. In addition, this treatment requires an acid neutralization step and subsequent concentration by water evaporation [5,6,10,12–14].

Heterogeneous hydrolysis is proposed as a possible alternative to reduce the environmental impact and facilitate the separation and reuse of the catalyst [15–25]. The hydrolysis of hemicelluloses is influenced by their structures, the conformation of their sugar units, and the type of catalyst acid sites, among others [18].

There are numerous studies on the heterogeneous hydrolysis of cellulose, whereas very few have studied the heterogeneous hydrolysis of hemicelluloses. A range of zeolites, resins, carbonaceous acid materials, functionalized silicas, metal oxides, and acidified clays have been used to hydrolyze hardwood and softwood hemicelluloses [15–25].

Xylose obtained from hemicelluloses hydrolysis is of particular interest because their hydrogenation leads to xylitol. Xylitol is a polyalcohol used as a sugar substitute for the consumption of diabetics and has anti-caries and anti-carcinogenic properties, among others [11,26–28]. The production and quality of xylitol depend on xylose purity. Xylitol can be obtained biotechnologically using specific microorganisms.

However, the process is affected by multiple factors, such as the initial concentration of inoculum, type of substrate, temperature, pH, transfer of oxygen, and culture medium composition. When using lignocellulosic hydrolyzates as xylose sources, several purification steps are required to remove all compounds that inhibit the metabolism and growth of the microorganisms [5,8,10].

Xylose hydrogenation has been studied using metallic catalysts based on Pt, Pd, Ru, Ni, and Ni-Raney, in the range of 80–140°C and hydrogen pressures greater than 5 MPa [11, 26,27,29]. Lee *et al.* [29] studied the hydrogenation of xylose in the aqueous phase at 100 °C and 5.5 MPa with Pt, Pd, Ru, Co, and Ni catalysts supported on γ-Al_2O_3. In all cases, xylitol was the only product obtained, following the activity order Ru> Ni ~ Co> Pt> Rh ~ Pd [29]. The same order was obtained by Wisniak *et al.* [30] using Rh, Ru, and Pd catalysts supported on activated carbon.

This research aimed to evaluate the hydrolysis of spent liquor from sugarcane bagasse hydrothermal treatment and its subsequent hydrogenation to obtain xylitol. Hydrolysis was studied using a solid acid catalyst (commercial sulfonated resin). The work consisted of producing a liquor rich in xylose, comparing it with one obtained by the homogeneous catalysis path, and determining the conditions of the heterogeneous route that o generates the maximum xylose yield. In the subsequent hydrogenation reaction to obtain xylitol, the hydrogenating activity of a Ni catalyst supported on γ-Al_2O_3 was studied. The overall yield of xylitol production by heterogeneous catalysis in two stages and the possibility of reusing and (or) regenerating the studied catalysts were analyzed.

MATERIAL AND METHODS

Catalyst

For the hydrolysis reaction, a commercial Purolite CT-275 resin was used, a macroporous strongly acid cation resin called RCT275, with a sulfonic acid as a functional group, and an acid amount of 5.2 mmol g^{-1}. For the hydrogenation of the hydrolyzed liquors, a Ni catalyst supported on γ-Al_2O_3 was prepared by incipient wetness impregnation, using an aqueous solution containing a metal precursor $Ni(NO_3)_2$ x $6H_2O$ to obtain 10 wt.% of Ni in the final solid. The solid was dried at 105 °C for 12 h and activated in H_2 flow (50 cm^3 min^{-1}) at 550 °C for 2 h (10 °C min^{-1}). The γ-Al_2O_3 support was prepared by thermal treatment of $Al(OH)_3$, which was directly calcined (without a heating ramp) at 600 °C for 30 min in the air atmosphere.

Ni-Raney was activated according to the procedure described by Devred *et al.* [31], employing

Ni-Al alloy (50 wt.% Ni) and NaOH (20 wt.%) solution at 80 °C for 3 h was used as a reference of a hydrogenation catalyst. First, the obtained solid was washed with distilled water until neutrality to remove the remaining NaOH.

Catalyst characterization

Adsorption-desorption measurements were performed for textural characterization. Surface area measurements, the Brunauer-Emmett-Teller (BET) multipoint method, and textural analysis were obtained using Micromeritics ASAP 2020 equipment. The samples were pretreated under vacuum in two stages of 1 h each, at 100 °C and 300 °C.

The acid-base properties of the solids were determined by the test of isopropanol decomposition (IPA). This reaction was tested in a continuous-flow fixed-bed reactor between 70 and 350 °C, atmospheric pressure, feed 4.5% IPA in Helium, with a flow of 40 cm^3 min^{-1}.

Potentiometric titrations were performed with 0.05 g of support suspended in acetonitrile (Merck) and stirred for 3 h. Then, the suspension was titrated with 0.05 mol L^{-1} n-butylamine (Carlo Erba) in acetonitrile using a Metrohm 794 Basic Titrino apparatus with a double junction electrode.

The Ni/γ-Al_2O_3 catalyst was characterized by atomic absorption spectrometry (AA), X-ray diffraction (XRD), temperature-programmed reduction (TPR), and transmission electron microscopy (TEM). Experimental details are attached as Supplementary data.

Obtaining and characterizing liquors

The sugarcane bagasse was supplied by the San Javier Mill, located in Misiones province, Argentina. This bagasse was collected, demodulated, and subjected to an autohydrolysis treatment. Autohydrolysis was performed in water at 180 °C for 20 min in a reactor heated with direct steam without stirring using a 7:1 (liquid: solid) ratio. These reaction conditions produce an autohydrolysis liquor with the maximum xylans concentration and the minimum formation of sugar degradation products such as furfural or HMF [9]. The liquors obtained from this treatment were vacuum-concentrated and were called Liquors A.

A subsequent acid hydrolysis step allows obtaining the so-called Liquors B. Heterogeneous acid hydrolysis was performed using the solid catalyst RCT275 resin in a 100 cm^3 reactor (Berghof Instruments BR-100) operated in batch mode, using catalyst/polymers mass ratios of 0.65 to 1.3, corresponding to an acid sites concentration of 0.52

and 1.04 mol L^{-1}, respectively. The obtained liquors were called liquor B1-4 and B1-6.

Homogeneous acid hydrolysis was performed under the optimum conditions using a 1 wt.% H_2SO_4 solution at 120 °C for 1 h (Liquor B2) [14]. Sulfuric acid used in the post-hydrolysis was removed by overliming with $Ca(OH)_2$ at ambient temperature.

The neutralization and purification stages of Liquors B1-4, B1-6, and B2, allow obtaining the Liquors C1-4, C1-6, and C2. For the neutralization, $Ca(OH)_2$ pro-analysis (Cicarelli) was used. Next, the treatment with 3 wt.% of activated carbon (Clarimex, DICA, Argentina) was carried out at 60 °C for 60 min. Finally, Liquors B1-4, B1-6, and B2 were stirred with Amberlite IRA-67 anion exchange resin (Adrem Corporación Industrial S.A., Argentina) to a constant pH for the acetic acid removal.

A diagram of the work stages and the terminology used for the different liquors is shown in Figure 1.
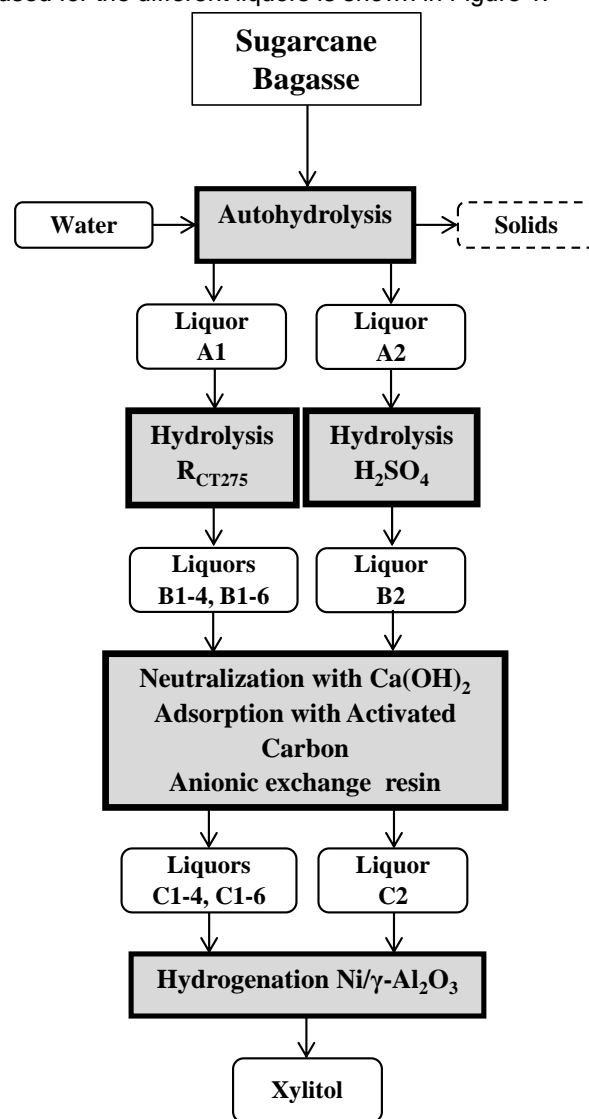
Figure 1. Diagram of the work stages and terminology used for the different liquors.

All liquors were characterized by the determinations of sugars (glucose, xylose, and arabinose), oligomers (glucans, xylans, arabinans), formic acid, acetic acid, and degradation products (furfural, 5-hydroxymethylfurfural (HMF)), according to Technical Report NREL / TP-510-42623 (January 2008) "Determination of Sugars, Byproducts, and Degradation Products in Liquid Fraction Process Samples," National Renewable Energy Laboratory.

$$Xylans\ conversion\,(\%) = 100\,\frac{initial\ moles\ of\ xylose\ in\ xylans - final\ moles\ of\ xylose\ in\ xylans}{initial\ moles\ of\ xylose\ in\ xylans} \quad (1)$$

$$Xylose\ yield\,(\%) = 100\,\frac{moles\ of\ xylose\ produced}{moles\ of\ xylose\ in\ xylans} \quad (2)$$

Hydrogenation

The hydrogenation reaction of xylose to xylitol in the liquid phase was carried out in the 100 cm³ reactor (BR-100 from Berghof Instruments), operated in batch mode at 3 MPa, in the range of 80–130 °C, with reaction

The quantification of these compounds and xylitol were carried out by HPLC liquid chromatography (Waters HPLC System) using an Aminex-HPX - 87 H87H column (BIO-RAD) with the following chromatographic conditions: 4 mM H_2SO_4 as eluent, 0.6 mL min⁻¹, 35 °C, with refractive index, and diode array detectors.

Xylans conversion (%) and xylose yield (%) were determined according to:

times between 2 and 4 h and a catalyst/xylose mass ratio between 0.25 and 0.5. As a reference, the hydrogenation of a commercial xylose solution (Biopack, 99%) was accomplished under the same conditions.

Xylose conversion and xylitol selectivity were determined according to:

$$Xylose\ conversion\,(\%) = 100\,\frac{initial\ moles\ of\ xylose - final\ moles\ of\ xylose}{initial\ moles\ of\ xylose} \quad (3)$$

$$Xylitol\ selectivity\,(\%) = 100\,\frac{moles\ of\ xylitol\ produced}{initial\ moles\ of\ xylose - final\ moles\ of\ xylose} \quad (4)$$

The yield of xylitol was determined as the ratio of the number of xylitol moles formed to the total initial xylose moles:

$$Xylitol\ yield\,(\%) = 100\,\frac{moles\ of\ xylitol\ produced}{Total\ moles\ of\ xylose\ in\ liquor\ A} \quad (5)$$

The Nickel content in the post-reaction liquors was determined by atomic absorption spectrometry (AA-6650 Shimadzu Spectrophotometer). The equipment was an IL Model 457 spectrophotometer

with a single channel and double beam.

RESULTS AND DISCUSSION

Catalyst characterization

The textural and acidic properties of the catalysts used for the heterogeneous hydrolysis stage (RCT275 resin) and hydrogenation (Ni/γ-Al₂O₃) are presented in Table 1.

Table 1. Textural and acid-base properties of catalysts for heterogeneous hydrolysis and hydrogenation

Catalyst	BET		Potentiometric titration	IPA decomposition reaction (X_{IPA} = 15%)		
	SBET[a]	Vp[b]	Ei	S$_{propylene}$[d]	S$_{acetone}$[e]	S$_{DIPE}$[f]
RCT275	30	0.5	718	100	0	0
γ-Al₂O₃	185	0.50	60	73	0	27
Ni/γ-Al₂O₃	165	0.43	68	n.d.	n.d.	n.d.

[a] Specific surface area (m² g⁻¹), [b] total pore volume (cm³ g⁻¹), [c] initial potential (mV), [d] selectivity to propylene (%), [e] selectivity to acetone (%), [f] selectivity to di-isopropyl eter (%)

The resin R_{CT275} has only strong macropores according to the specifications available on the manufacturer's website (https://www.purolite.com/prod uct/ct275). The potentiometric titration technique with n-butylamine allows determining the strength of the

acid sites in a given solid. The initial potential of the titration curve (E_i) indicates the maximum strength of the acid sites. In this sense, R_{CT275} presented very strong acid sites.

The decomposition reaction of isopropanol (IPA)

is an indirect method that allows for characterizing the acid strength and type of sites on the surface of a solid. They are classified according to their ability to dehydrate and form propylene, di-isopropyl ether (DIPE), and (or) acetone, or to dehydrogenize and form acetone and hydrogen. For an IPA conversion of 15%, the selectivity of the different decomposition products is presented in Table 1. R_{CT275} presents propylene as the only product, indicating that these materials possess strong Lewis acid sites and (or) Brønsted [32]. The sulfonic acid groups (HSO_3^-) in the protonated form (H^+) of the R_{CT275} resin give it Brønsted acidity, which agrees with the obtained results.

Regarding the textural properties, γ-Al_2O_3 presents a type IV isotherms with H1 hysteresis, characteristics of mesoporous materials. The XRD diagram for this support (included in supplementary information) shows peaks at $2\theta = 32.5°$, $36.9°$, $39.1°$, $45.3°$, $59.6°$, and $66.7°$, which are characteristics of low crystalline aluminum oxide (JCPDS 04 -0858).

The decomposition reaction of isopropanol (IPA) of γ-Al_2O_3 showed the obtaining of propylene and DIPE that would indicate the presence of Lewis acid sites and basic sites, both with medium or high strength, which corresponds to the acid-base character of the alumina's surface [32]. The oxide anions or the OH^- of the surface provide relatively low basicity, whereas the Al^{+3} ions constitute strong Lewis acid sites [32,33]. The strong acidity of the Al^{+3} ions would explain the higher selectivity to propylene obtained in this reaction [33]. The decomposition reaction of isopropanol by Ni/γ-Al_2O_3 catalyst does not allow evaluation of the acidic properties of the sites, as Ni leads to obtaining dehydrogenation and cracking products. Therefore, it was not carried out.

Regarding the potentiometric titration results, the initial potential (Ei) for the Ni/γ-Al_2O_3 catalyst indicates the presence of stronger acid sites than in the γ-Al_2O_3 support.

The supplementary information shows the XRD diagram of the Ni/γ-Al_2O_3 catalyst. As mentioned before, it is possible to observe characteristic peaks of low crystalline aluminum oxide (JCPDS 04 -0858) and a peak at $51.7°$ that corresponds to the metallic phase of Ni (JCPDS 4-850). Due to the low intensity of that peak, it is not possible to calculate an average crystallite size (using the Scherrer equation), but this may indicate that these particles are highly dispersed, which is corroborated by TEM (Figure 2) since the average particle diameter is ~4 nm.

Hydrolysis of liquors from sugarcane bagasse hydrothermal treatment

The average chemical composition of sugarcane bagasse was: 43.1% glucans, 23.8% xylans, 1.7%

arabinans, 1.7% acetyl groups, 21.3% lignin, 4.8% extractives, and 1.5% ash. The raw materials for hydrolysis reactions are obtained from sugarcane bagasse autohydrolysis. They are named liquors A. It is important to note that this type of lignocellulosic raw material has inhomogeneous characteristics. Therefore, there was little difference in the used liquors A compositions.
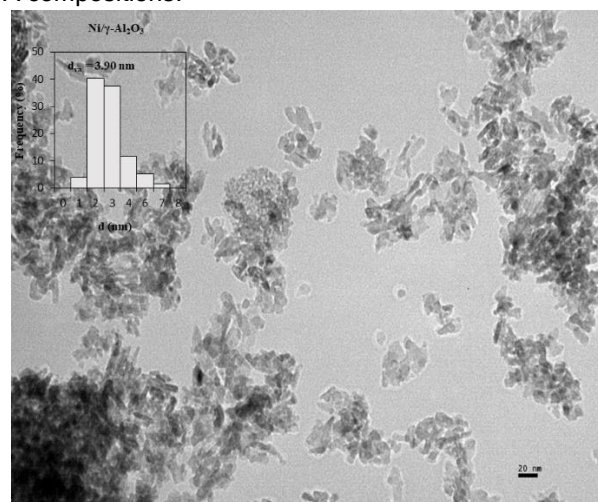
Figure 2. TEM micrograph and particle size distribution of Ni/γ-Al_2O_3 catalyst.

Liquors B1-4, B1-6, and B2 were obtained from liquors A1 and A2 acid hydrolysis. Their ulterior purification led to the xylose-rich liquors denominated Liquors C1-4, C1-6, and C2. Finally, these last liquors were hydrogenated to obtain xylitol. Table 2 summarizes the hydrolysis results employing R_{CT275} as the heterogeneous catalyst and H_2SO_4 as a reference.

The liquors A (raw material) has a xylans concentration (between 300 and 400 mmol L^{-1}) and a concentration of xylose as a monomer (~70 mmol L^{-1}). Acetic acid, which comes from the hydrolysis of acetyl bonds in arabinoxylans, is among the main components. The presence of acetic acid is beneficial for the hydrolysis reactions of polymers [9]. The main organic compounds are reported in Table 2. However, numerous and diverse aromatic compounds are difficult to identify and quantify. It has been reported that phenolic derivatives such as *p*-coumaric acid, ferulic acid, vanillic acid, and vanillin, produced by lignin degradation, are present in a total concentration of approximately 5 g L^{-1} (determined as g equivalent of vanillin L^{-1}) [14].

The Liquor B1-4 is obtained using R_{CT275} as a catalyst and a catalyst/polymers mass ratio of 0.65, corresponding to a concentration of acid sites of 0.52 mol L^{-1}, employing 100 °C and 4 h of reaction time. Liquor B1-4 contains a high content of xylose (392.16 mmol L^{-1}), arabinose (19.85 mmol L^{-1}), glucose (10.13 mmol L^{-1}), cellobiose (6.53 mmol L^{-1}) and acetic acid (115.57 mmol L^{-1}). The reached conversion was

84% after 4 h of reaction, meaning incomplete hydrolysis of the xylans in liquor A. The acetic acid content increased to 115.57 mmol L^{-1} due to the cleavage of the acetylenic bonds favored by the acidity of the medium.

These results are comparable with that reported by Cará *et al.* [24]. These authors employed different sulfonated resins (Amberlyst-35 and Amberlyst-70) for the hydrolysis of commercial Beechwood xylans at 120 °C for 4 h, and they reported a yield of sugar monomers (xylose and arabinose) in the range of 55% to 80% [24].

The variables affecting the hydrolysis yield are temperature, time, and catalyst mass. This study was accomplished at 100 °C because the resin R_{CT275} has a temperature limit of 130 °C. In addition, the effect of reaction time was studied with acid sites concentration of 0.52 mol L^{-1} and 1.04 mol L^{-1} of R_{CT275} as the catalyst, as shown in Figure 3.

Table 2. Composition of the liquors obtained from autohydrolysis, heterogeneous hydrolysis, and purification steps

Treatment		Hydrolysis with R_{CT275}					Hydrolysis with H_2SO_4		
Concentration of products (mmol L^{-1})		A1	B1-4[a]	C1-4	B1-6[b]	C1-6	A2	B2	C2
Monomer	Xylose	66.81	392.16	390.33	408.51	407.65	68.61	353.03	345.70
	Glucose	1.94	10.13	8.33	14.38	13.32	0.94	27.36	und.
	Cellobiose	und.	6.53	6.13	5.84	5.84	und.	3.51	und.
	Arabinose	14.65	19.85	18.65	19.18	18.65	19.78	21.85	und.
	HMF	0.79	0.79	und.	0.87	und.	und.	0.87	und.
	Furfural	5.20	9.26	1.56	56.20	8.43	und.	10.20	7.70
	Acetic acid	73.27	115.57	28.31	107.74	26.64	43.13	128.23	24.98
	Formic acid	und.	18.63	18.47	und.	und.	14.34	9.34	7.39
Polymer	Xylose	418.5	65.78	und.	3.73	und.	304.40	und.	und.
	Glucose	62.39	39.13	und.	45.68	und.	30.47	und.	und.
	Arabinose	8.33	2.33	und.	5.73	und.	4.20	und.	und.
	Acetic acid	31.31	und.	und.	0.50	und.	und.	und.	und.
pH		3.0	1.8	6	1.8	6	3.4	1.3	6
Xylans conversion (%)			84		99			100	
Xylose yield (%)			78		82			95	

[a] 100 °C, 4 h, mass ratio catalyst/polymer = 0.65, 0.52 mol acid sites L^{-1}. [b] 100 °C, 6 h, mass ratio catalyst/polymer = 1.3, 1.04 mol acid sites L^{-1}. und.- undetected.
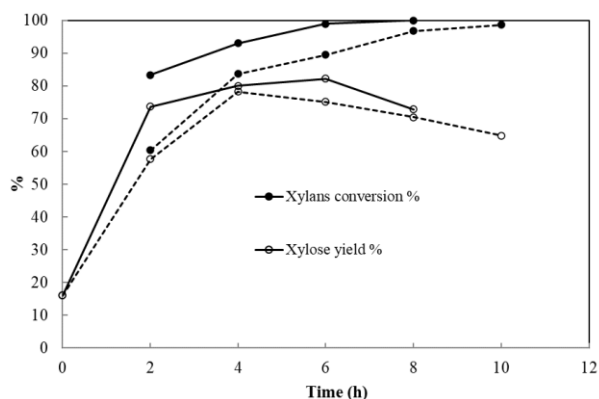
Figure 3. Xylans conversion and xylose yield as a time function. Dotted lines: 0.52 mol L^{-1} acid sites. Full lines: 1.04 mol L^{-1} acid sites.

A xylans conversion of 98.7% was achieved at 10 h, while the maximum xylose yield (78%) was obtained at 4 h of reaction time (liquor B1-4) using an acid concentration of 0.52 mol L^{-1}. With a higher concentration of acid sites (1.04 mol L^{-1}), the total conversion of xylans was achieved at 6 hours, with a maximum xylose yield of 82% (Figure 3 and Table 2).

Figure 4 shows the concentration of the products obtained from the hydrolysis of xylans as a function of time. When using an acid sites concentration of 0.52 mol L^{-1}, due to the dehydration of xylose to furfural, after 4 h of reaction time, the decrease in the xylose

concentration and the increase in the furfural concentration were observed. The same behavior was observed with an acid site concentration of 1.04 mol L^{-1} after 6 h of reaction, which explains the decrease in the yield to xylose shown in Figure 3. Ormsby *et al.* [25] reported that when using Amberlyst-15 to hydrolyze birchwood xylans, xylose concentration decreased after 5 h at 120 °C, suggesting a sequential reaction and formation of a dehydrated product, as furfural.
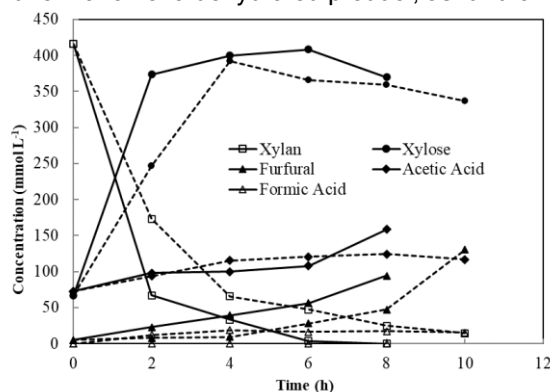
Figure 4. The concentration of xylans hydrolysis products. Dotted lines: 0.52 mol L^{-1} acid sites. Full lines: 1.04 mol L^{-1} acid sites.

The homogeneous hydrolysis of liquor A2 was carried out using H_2SO_4 1 wt.% at 120 °C and 1 h of reaction time. The liquor obtained was named

Liquor B2. In this case, the xylans conversion was 100%, and the xylose yield was 95%. Based on preliminary post-hydrolysis assays, the maximal xylose concentration in spent liquors was achieved using 1 wt.% of H_2SO_4. Higher acid concentrations produce a decrease in xylose concentration and an increase in furfural concentration [14].

The next step for obtaining xylitol by hydrogenation of the xylose-rich liquors B1-4, B1-6, and B2 is a subsequent neutralization (with $Ca(OH)_2$) followed by a purification (with activated carbon Clarimex and Amberlite IRA-67 resin). Details from the previous work of Vallejos *et al*. [14] are in the experimental section. The treatment using activated carbon reduced the phenolic compounds content, furfural, HMF, and polymers, without affecting the concentration of sugars and organic acids. Removal of 80-85% acetic acid was possible using Amberlite IRA-67 resin. This treatment allowed obtaining liquors C1-4, C1-6, and C2 rich in xylose, with a low acetic acid content (Table 2).

Hydrogenation of xylose-rich liquors to obtain xylitol

The first step in studying xylitol production from xylose-rich liquors is to find the most suitable operating condition for the $Ni/\gamma\text{-}Al_2O_3$ catalyst in the hydrogenation reaction of pure xylose (Biopack, 99%) using the same concentration of xylose that has a liquor C (400 mmol L^{-1}).

Conditions varied between 80 °C and 130 °C of temperature, 2 MPa and 3 MPa of hydrogen pressure, and 2 h and 4 h of reaction time (Table 3). Only xylitol was observed at 100 °C, whereas the selectivity towards xylitol decreased at 130 °C to 74% due to the generation of xylose degradation products. At temperatures above 150 °C other authors have obtained by-products such as D-arabinitol, D-xylulose, acid D-xylonic, furfural, and even others from C-C bond break reactions [27,30].

Table 3. Hydrogenation of commercial xylose

Catalyst	mc/mx[a]	Temperature (°C)	Hydrogen Pressure (MPa)	Time (h)	Xylose conversion (%)	Selectivity towards xylitol (%)
	0.25	80	2	2	36	100
	0.25	100	2	2	58	100
$Ni/\gamma\text{-}Al_2O_3$	0.25	130	2	2	80	74
	0.25	100	2	4	81	100
	0.25	100	3	2	85	100
Ni-Raney	0.25	100	3	2	70	100
$Ni/\gamma\text{-}Al_2O_3$	0.50	100	3	2	100	100

[a] mc/mx: mass ratio catalyst to xylose.

$Ni/\gamma\text{-}Al_2O_3$ was more active than the commercial Ni-Raney catalyst (Table 3). The explanation could be the smaller metal particle size in $Ni/\gamma\text{-}Al_2O_3$ compared to the Ni-Raney catalyst. Besides, in the aqueous phase, the xylose forms a cyclic hemiacetal due to the reaction between its aldehyde and hydroxyl groups [10]. Thus, the presence of the acid sites of the $\gamma\text{-}Al_2O_3$ support would favor the cleavage of the C-O bond of hemiacetal. The best results were obtained at 100 °C, 3 MPa of hydrogen pressure, and 2 h, with a mass relation of catalyst to xylose of 0.5, reaching a xylose conversion of 100% with a xylitol selectivity of 100%.

The main components in the liquors susceptible to hydrogenation are xylose, arabinose, glucose, and cellobiose. Xylose is present in percentages between 82% and 90%. Mannose and galactose are minor components in bagasse hemicelluloses. Then, other polyols, such as sorbitol, arabitol, and mannitol, can indeed be produced during the hydrogenation of these liquors but have not been detected. Therefore, it was determined that xylitol is the only hydrogenation product of the liquor (Table 4).

The hydrogenation results of Liquor C1-6 (shown in Table 4) allows obtaining xylose conversions close to 82% and 95% for mc/mx of 0.25 and 0.5, respectively. In addition, the xylitol selectivity was 100% in 2 h in both cases.

By atomic absorption analysis of the post-reaction Liquors C1-6, the presence of nickel was undetected (<1 ppm), which evidenced that its leaching did not occur when the pH of the reaction medium was 6. The acetic acid content in these liquors (~30 mmol L^{-1}) did not affect the hydrogenation step. Additional tests, adding acetic acid to the liquor, allowed the determination of 1000 ppm of Nickel loss by leaching when 116 mmol L^{-1} of acetic acid is reached. The above evidenced the importance of its presence in xylose-rich liquors.

In the hydrogenation experiments of the C2 liquor (from hydrolysis with H_2SO_4), a xylose conversion of 16% was achieved. This low level could be associated with sulfur traces (1–5 ppm) in the liquor, a known poison of the metallic function for any supported metallic catalyst [34,35]. However, this low sulfur content is not detrimental to the biotechnological production of xylitol [14].

Table 4. Hydrogenation of xylose-rich liquors

Concentration of products (mmol L^{-1})	Liquor C1-6 mc/mx^a = 0.25	Liquor C1-6 mc/mx^a = 0.50	Liquor C2 mc/mx^a = 0.50
Xylose	75.27	4.00	335.71
Xylitol	326.65	390.40	63.10
Glucose	5.05	4.72	und.
Cellobiose	6.13	5.84	und.
Arabinose	14.99	15.32	und.
HMF	und.	und.	7.70
Furfural	und.	und.	15.61
Acetic acid	28.31	28.31	5.66
Xylose conversion (%)	81	99	16
Xylitol selectivity (%)	100	100	100
Xylitol yield (%)	67	83	15

^{a} mc/mx: mass ratio catalyst to xylose. Reaction conditions: 100 °C, 3 MPa of H$_2$ and 2 h. und.- undetected.

The higher xylitol yield (83%) was obtained in the hydrolysis with R$_{CT275}$ and subsequent hydrogenation with Ni/γ-Al$_2$O$_3$ (Table 4). Yamaguchi *et al.* [36] achieved a xylitol yield of 60% in a single pot using a RuPt/C bimetallic catalyst in the direct conversion of Japanese cedar bagasse at 190 °C, 5 MPa of H$_2$, and 16 h. Ribeiro *et al.* [37] achieved a xylitol yield of 46% in a single pot with a Ru/C catalyst in the direct conversion of corncob xylans at 205 °C, 5 MPa of H$_2$, and 5 h.

In this way, the xylitol yields obtained in this work in two stages (heterogeneous hydrolysis followed by hydrogenation) are higher than the yields obtained in single pot processes using noble metal-based catalysts like Ru and Pt and more severe reaction conditions.

Finally, to determine the possibility of reusing these solids for other reaction stages, experiments were carried out without removing the R$_{CT275}$ catalyst from the reactor and renewing the reaction mixture to evaluate 4 hydrolysis cycles. On the other hand, in each evaluation of the hydrogenation cycle, the Ni/γ-Al$_2$O$_3$ catalyst is pre-reduced in the H$_2$ atmosphere to ensure the presence of metallic Ni after contact with air.

Figure 5 shows that the activity loss between one cycle and another is very low, so it is possible to reuse both catalysts.

Biological methods for xylose saccharification and fermentation to xylitol have recently been reported but are not implemented at an industrial scale. The saccharification of hemicellulosic xylans into xylose is expensive and requests different xylanase enzymes for its complete hydrolysis. For example, endo-1, 4-β-xylanases produce random hydrolysis, and 1,4-β-d-xylosidases generate oligosaccharides. Besides, to achieve high enzymatic saccharification with low xylitol production cost, xylanases require severe conditions, high activity, substrate specificity, stability, and tolerance to inhibitors [38]. It has recently been reported that accessory enzymes from hypercellulolytic *Penicillium funiculosum* facilitate the complete saccharification of sugarcane bagasse [39].
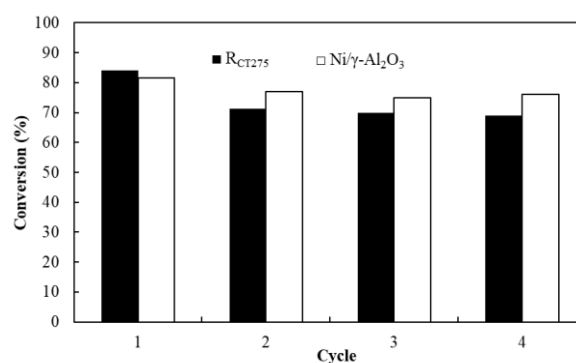
Figure 4. Hydrolysis and hydrogenation catalyst reuses. Reactions conditions: Hydrolysis: 100 °C, 4 h, mass ratio catalyst/polymer = 0.65, (0.52 mol acid sites L^{-1}). Hydrogenation: 100 °C, 2 h, 3 MPa of H$_2$, mass ratio catalyst/xylose = 0.25.

The xylose fermentation to xylitol by microbial strain has been investigated to improve yield and economic feasibility. In addition, modern genetic engineering and adaptive methods of microbial strains have been widely studied. For example, Hernández-Pérez *et al.* [40] achieved 26.19 g L^{-1} of xylitol from a sugarcane bagasse and straw hemicellulosic hydrolysate *Candida guilliermondii* FTI 20037 with a xylitol volumetric productivity of 0.55 g L^{-1} h^{-1}. Recent studies showed that recombined *Saccharomyces cerevisiae* produces high xylitol yields and ethanol from sugarcane bagasse [41,42]. In previous work, Vallejos *et al.* [14] reported maximal xylitol concentration (32.0 g L^{-1}) from hemicellulosic liquors obtained from sugarcane bagasse autohydrolysis using *Candida tropicalis* (104.1 g L^{-1} xylose, 0.46 g g^{-1} yield, 0.27 g L^{-1} h^{-1} productivity). They also determined technological parameters to obtain a detoxified spent liquor rich in xylose and its bioconversion to xylitol. In this work, using heterogeneous hydrolysis and hydrogenation, xylitol yield was 83% and approximately 59 g L^{-1} concentration, indicating that biological procedures require much development.

CONCLUSION

Heterogeneous catalysis in two-step routes (hydrolysis and hydrogenation) constitutes an outstanding alternative to producing xylitol from sugarcane bagasse hydrothermal spent liquors since materials can be easily separated and reused in several reaction cycles.

In the first step, xylose-rich liquors are obtained by heterogeneous hydrolysis. Then, they can be hydrogenated to xylitol using the Ni/γ-Al$_2$O$_3$ catalyst with good yields.

Acid hydrolysis was carried out using an R$_{CT275}$ sulfonated resin and sulfuric acid as reference. The heterogeneous catalyst R$_{CT275}$ was suitable for hydrolysis, avoiding the presence of sulfur traces in liquors. Although the liquor obtained by homogeneous hydrolysis with sulfuric acid is a usual raw material to produce xylitol by biotechnological processes, it cannot be used for hydrogenation with supported metal catalysts because of the poisoning of the metal phase and the catalyst deactivation. Nevertheless, xylitol yields of about 83%, obtained using R$_{CT275}$ and Ni/γ-Al$_2$O$_3$ catalysts, were higher than those from other studies in the literature.

ACKNOWLEDGMENTS

REFERENCES

[1] M. FitzPatrick, P. Champagne, M. F. Cunningham, R. A. Whitney, Bioresour. Technol. 101 (2010) 8915–8922. https://doi.org/10.1016/j.biortech.2010.06.125

[2] W.E. Mabee, P.N. McFarlane, J.N. Saddler, Biomass Bioenergy 35 (2011) 4519–4529. https://doi.org/10.1016/j.biombioe.2011.06.026

[3] M.E. Vallejos, F.E. Felissia, M. C. Area, Bioresources 12 (2017) 2058–2080. https://bioresources.cnr.ncsu.edu/wp-content/uploads/2017/02/BioRes_12_1_2058_REVIEW_Vallejos_FA_Hydrothermal_Treatm_Agro_Forest_Indust_Waste_Value_10459.pdf

[4] Food and Agriculture Organization (FAO). Statistics Division of the FAO (FAOSTAT). http://www.fao.org/faostat/en/#data/QC, [accessed 19 February 2022].

[5] N. Clauser, S. Gutiérrez, M.C. Area, F.E. Felissia, M.E. Vallejos. J. Renew. Mater. 6 (2018) 139–151. http://dx.doi.org/10.7569/JRM.2017.634145

[6] H. Boussarsar, B. Rogé, M. Mathlouthi, Bioresour. Technol. 100 (2009) 6537–6542. https://doi.org/10.1016/j.biortech.2009.07.019

[7] M. Fatih Demirbas, Appl. Energy 86 (2009) 151–161. https://doi.org/10.1016/j.biortech.2009.07.019

[8] D.J. Hayes, Catal. Today 145 (2009) 138–151. https://doi.org/10.1016/j.cattod.2008.04.017

[9] M.E. Vallejos, F.E. Felissia, J. Kruyeniski, M.C. Area, Ind. Crops Prod. 67 (2015) 1–6. https://doi.org/10.1016/j.indcrop.2014.12.058

[10] L. da Costa Sousa, S. Chundawat, V. Balan, B. E. Dale, Curr. Opin. Biotechnol. 20 (2009) 339–347. https://doi.org/10.1016/j.copbio.2009.05.003

[11] Y. Delgado Arcaño, O.D. Valmaña Garcia, D. Mandelli, W.A. Carvalho, L.A. Magalhães Pontes, Catal. Today 344 (2020) 2–14. https://doi.org/10.1016/j.cattod.2018.07.060

[12] K. Nakajima, M. Hará, ACS Catal. 2 (2012) 1296–1304. https://doi.org/10.1021/cs300103k

[13] S. Suganuma, K. Nakajima, M. Kitano, D. Yamaguchi, H. Kato, S. Hayashi, M. Hara, J. Am. Chem. Soc. 130 (2008) 12787–12793. https://doi.org/10.1021/ja803983h

[14] M.E. Vallejos, M. Chade, E. Beda Mereles, D.I. Bengoechea, J.G. Brizuela, F.E. Felissia, M.C. Area, Ind. Crops Prod. 91 (2016) 161–169. https://doi.org/10.1016/j.indcrop.2016.07.007

[15] P.L. Dhepe, R. Sahu, Green Chem. 12 (2010) 2153–2156. https://doi.org/10.1039/C004128A

[16] Y. Jiang, X. Li, X. Wang, L. Meng, H. Wang, G. Peng, X. Wang, X. Mu, Green Chem. 14 (2012) 2162–2167. https://doi.org/10.1039/C2GC35306G

[17] M. Kitano, D. Yamaguchi, S. Suganuma, K. Nakajima, H. Kato, S. Hayashi, M. Hara, Langmuir 25 (2009) 5068–5075. https://doi.org/10.1021/la8040506

[18] B.T. Kusema, G. Hilmann, P. Mäki-Arvela, S. Willför, B. Holmbom, T. Salmi, D.Y. Murzin, Catal. Lett. 141 (2011) 408–412. https://doi.org/10.1007/s10562-010-0530-x

[19] Y. Ogaki, Y. Shinozuka, T. Hara, N. Ichikuni, S. Shimazu, Catal. Today 164 (2011) 415–418. https://doi.org/10.1016/j.cattod.2010.11.002

[20] M. Okamura, A. Takagaki, M. Toda, J.N. Kondo, K. Domen, T. Tatsumi, M. Hara, S. Hayashi, Chem. Mater. 18 (2006) 3039–3045. https://doi.org/10.1021/cm0605623

[21] A. Onda, T. Ochi, K. Yanagisawa, Green Chem. 10 (2008) 1033–1037. https://doi.org/10.1039/B808471H

[22] R. Sahu, P.L. Dhepe, ChemSusChem 5 (2012) 751–761. https://doi.org/10.1002/cssc.201100448

[23] L. Zhou, M. Shi, Q. Cai, L. Wu, X. Hu, X. Yang, C. Chen, J. Xu, Microporous Mesoporous Mater. 169 (2013) 54–59. https://doi.org/10.1016/j.micromeso.2012.10.003

[24] P.D. Cará, M. Pagliaro, A. Elmekawy, D.R. Brown, P. Verschuren, N.R. Shiju, G. Rothenberg, Catal. Sci. Technol. 3 (2013) 2057–2061. https://doi.org/10.1039/C3CY20838A

[25] R. Ormsby, J. R. Kastner, J. Miller, Catal. Today 190 (2012) 89–97. https://doi.org/10.1016/j.cattod.2012.02.050

[26] J.P. Mikkola, R. Sjöholm, T. Salmi, P. Mäki-Arvela, Catal. Today 48 (1999) 73–81. https://doi.org/10.1016/S0920-5861(98)00360-5

[27] J. Wisniak, M. Hershkowitz, R. Leibowitz, S. Stein, Ind. Eng. Chem. Prod. Res. Dev. 13 (1974) 75–79. https://doi.org/10.1021/i360049a015

[28] M. Yadav, D.K. Mishra, J. Hwang, Appl. Catal., A 425 (2012) 110–116. https://doi.org/10.1016/j.apcata.2012.03.007

[29] J. Lee, Y. Xub, G.W. Huber, Appl. Catal., B 140 (2013) 98–107. https://doi.org/10.1016/j.apcatb.2013.03.031

[30] J. Wisniak, M. Hershkowitz, S. Stein, Ind. Eng. Chem. Prod. Res. Dev. 13 (1974) 232–236. https://doi.org/10.1021/i360052a004

[31] F. Devred, A.H. Gieskea, N. Adkins, U. Dahlborg, C.M. Bao, M. Calvo-Dahlborg, J.W. Bakker, B.E. Nieuwenhuys, Appl. Catal., A 356 (2009) 154–161. https://doi.org/10.1016/j.apcata.2008.12.039

[32] A. Gervasini, J. Fenyvesi, A. Auroux, Catal. Lett. 43 (1997) 219–228. https://doi.org/10.1023/A:1018979731407

[33] G. Busca, Catal. Today 226 (2014) 2–13. https://doi.org/10.1016/j.cattod.2013.08.003

[34] D.S. Brands, U.A. Sai, E.K. Poels, A. Bliek, J. Catal. 186 (1999) 169–180. https://doi.org/10.1006/jcat.1999.2553

[35] L.S. Carvalho, C.L. Pieck, M.L. Rangel, N.S. Figoli, C.R. Vera, J.M. Parera, Appl. Catal., A 269 (2004) 105–116. https://doi.org/10.1016/j.apcata.2004.04.006

[36] A. Yamaguchi, O. Sato, N. Mimura, M. Shirai, Catal. Today 265 (2016) 199–202. https://doi.org/10.1016/j.cattod.2015.08.026

[37] L.S. Ribeiro, J.J. Delgado, J.J. de Melo Órfão, M.F.R. Pereira, RSC Adv. 6 (2016) 95320–95327. https://doi.org/10.1039/C6RA19666G

[38] L. Venkateswar Rao, J.K. Goli, J. Gentela, S. Koti, Bioresour. Technol. 213 (2016), 299–310. https://doi.org/10.1016/j.biortech.2016.04.092

[39] O.A. Ogunyewo, P. Upadhyay, G.H. Rajacharya, O. E. Okereke, L. Faas, L.D. Gómez, S. J. McQueen-Mason, S. S. Yazdani, Biotechnol. Biofuels. 14 (2021), 1–17. https://doaj.org/article/aeeb042f69924f6787414bdcf3e672ab

[40] A.F. Hernández-Pérez, A.C. Chaves-Villamil, P.V. de Arruda, J.C. dos Santos, M. das G. de A. Felipe, Waste Biomass Valorization 11 (2020), 4215–4224. https://doi.org/10.1007/s12649-019-00742-6

[41] M.S.S, Reshamwala, A.M. Lali, Biotechnol. Prog. 36 (2020), e2972. https://doi.org/10.1002/btpr.2972

[42] G. Guirimand, K. Inokuma, T. Bamba, M. Matsuda, K. Morita, K. Sasaki, C. Ogino, J.-G. Berrin, T. Hasunuma, A. Kondo, Green Chem. 21 (2019), 1795–1808. https://doi.org/10.1039/C8GC03864C

JULIETA L. CERIONI[1,2]
MARIA E.VALLEJOS[3]
FERNANDO E. FELISSIA[3]
MARÍA C. AREA[3]
NORA N. NICHIO[1,2]
GERARDO F. SANTORI[1,2]

[1]CINDECA, Facultad de Ciencias Exactas, Universidad Nacional de La Plata. CCT La Plata- CONICET, Argentina

[2]Facultad de Ingeniería, Universidad Nacional de La Plata, La Plata, Argentina

[3]IMAM, UNaM, CONICET, FCEQYN, Programa de Celulosa y Papel (PROCYP), Félix de Azara, Posadas, Misiones, Argentina

NAUČNI RAD

DOBIJANJE KSILITOLA HIDROLIZOM-HIDROGENACIJOM OTPADNOG LUGA IZ OBRADE BAGAZE ŠEĆERNE TRSKE

Ovaj rad predstavlja proučavanje heterogene katalize otpadnog luga iz hidrotermičke obrade bagaze šećerne trske korišćenjem sulfonovane smole. Pored toga, rezultati su upoređeni sa onima dobijenim konvencionalnim putem korišćenjem sumporne kiseline kao homogenog katalizatora. Heterogena kataliza je pogodna za hidrolizu otpadnog luga iz hidrotermičke obrade bagaze šećerne trske pod blagim uslovima (100 °C i 6 h). Dobijeni maksimalni prinos ksiloze iznosio je 82% zbog formiranja furfurala, što uzrokuje pad selektivnosti ksiloze. Hidrogenacijom ovog luga bogatog ksilozom na 100 °C i pritisku vodonika od 3 MPa korišćenjem katalizatora Ni/γ-Al₂O₃ u masenom odnosu prema ksilozi od 0,5 postignuta je ukupna konverzija ksiloze sa selektivnošću prema ksilitolu od 100%. Heterogena kataliza u dvostepenom putu (hidroliza i hidrogenacija) predstavlja izvanrednu alternativu proizvodnji ksilitola iz hidrotermičkog otpadnog luga šećerne trske, pošto se materijali mogu lako odvojiti i ponovo upotrebiti u nekoliko reakcionih ciklusa.

Ključne reči: bagasa šećerne trske, hidroliza, hidrogenacija, ksiloza, ksilitol.

52

LV CHAO[1,2]
YIN HONGXIN[2]
SUN MINGHE[2]
ZHU HANGYU[1]

[1]Key Laboratory for Ferrous Metallurgy and Resources Utilization of Ministry of Education, Wuhan University of Science and Technology, Wuhan, China

[2]School of Control Engineering, Northeastern University at Qinhuangdao, Hebei, China

SCIENTIFIC PAPER

SIMULATION STUDY OF CITRIC ACID EFFECTS ON PYROLYSIS OF HYDROCHLORIC ACID PICKLING WASTE LIQUOR

Article Highlights
- The couples and simulations of fluid flow, phase change, and chemical reactions are achieved
- New chemical reactions are added, describing the phenomenon of Fe_3O_4 appearance
- The effects of citric acid on the ingredient of reaction products are discussed

Abstract
During pyrolysis of hydrochloric acid pickling waste liquid in a Venturi reactor from iron and steel enterprises, the reaction products agglomerated and hindered product recovery. Addition of citric acid to materials at the inlet improved product distribution. In this paper, a numerical simulation of the combustion, phase change, and gas-solid chemistry involved in a citric acid-added pickling waste liquid was conducted. These results showed that citric acid added to the inlet resulted in a peak concentration of carbon dioxide (CO_2) in the back half of the Venturi throat, and some ferric oxide (Fe_2O_3) underwent a secondary reaction to afford ferroferric oxide (Fe_3O_4). As the addition of citric acid increased, the flow of Fe_2O_3 at the outlet first increased and then decreased, while the flow rate of Fe_3O_4 first decreased and then increased. When the ratio of citric acid was 7%, the flow rate of Fe_2O_3 was the smallest, and the flow rate of Fe_3O_4 was the largest.

Keywords: pyrolysis, citric acid, Fe_2O_3, Fe_3O_4, numerical simulation.

Hydrochloric acid is used during steel production to remove oxides from the product surface, resulting in a great deal of pickling waste liquid [1]. Most steel manufacturers use Ruthner spray atomization roasting to regenerate hydrochloric acid, which results in an iron oxide powder by-product [2]. The Fe_2O_3 by-product can be used in pigments, polishing powders, and catalysts [3–5]. Also, Fe_3O_4 can be used in magnetic materials and the manufacture of telecommunications equipment [6,7]. However, this process line requires high capital costs and regular cleaning and replacement of atomizing nozzles, which are difficult for small and medium-sized companies to achieve. Small and medium-sized companies use lime and calcium carbide slag, among other things, to neutralize the reaction, and the pH of the waste liquid is adjusted and discharged directly, which results in a waste of resources and the formation of solid waste [8]. Therefore, developing new low-cost treatment options for pickling waste liquid is important. Using a Venturi reactor for waste acid recycling effectively reduces equipment costs, efficiently recovers by-products, and promotes the process.

Many scholars have studied the spray pyrolysis technique. For the preparation of MgO by spray pyrolysis of bischofite in salt lakes, Liu *et al.* [9] used computational fluid dynamics (CFD) to simulate the spray pressure and temperature distribution of the pyrolysis furnace; this provided data and the model basis for nozzle selection, pyrolysis furnace structure optimization and flow field study. Shammari *et al.* [10] used spray pyrolysis to successfully prepare TiO_2/reduced graphene oxide (rGO) films with different

GO concentrations (0, 3, 5, and 10 wt.%) on fluorine-doped tin oxide (FTO) glass substrates. TiO_2/rGO thin films prepared from different GO concentrations (0, 3, 5, and 10 wt.%) were deposited on fluorine-doped tin oxide (FTO) glass substrates using a spray pyrolysis technique (SPT). Moumen *et al.* [11] used spray pyrolysis to prepare CuO films and discussed the influence of substrate temperature on the structure and optical properties of CuO films deposited using spray pyrolysis. The effect of substrate temperature on the structural and optical properties of the films was discussed. Lv *et al.* [12–14] proposed a new process for preparing metal oxides by direct pyrolysis of a solution containing a rare earth chloride, magnesium chloride, and pickling waste hydrochloric acid. This process incorporated a Venturi reactor that atomized the solution using the heat generated by the combustion of methane to provide energy for the phase change of the solution and the pyrolysis of the metal chloride solution to obtain high-quality metal oxides. The structure of the Venturi reactor contributes to a sharp increase in gas velocity at the throat. Then the solution was fiercely collided into droplets by the high-speed gas, which can enhance the mixing and increase the reaction efficiency. Particle agglomerations and large particle sizes were observed when the Venturi reactor was used. Citric acid was added to change the physical properties of the metal chloride solution to

solve this problem by eliminating the hollowing and agglomeration of the product particles [15].

Citric acid may also be added to $FeCl_2$ and $FeCl_3$ solutions to improve Fe_2O_3 agglomeration in a Venturi reactor. In this paper, the direct pyrolysis of pickling waste liquid after citric acid addition was simulated and studied; the coupling of combustion, phase transition, and gas-solid chemistry was completed using Fluent software combined with a user-defined function (UDF).

MODELLING

Figure 1 shows the dimensions of the reactor; the length was 0.85 m, the left-hand gas-phase inlets consisted of a fuel inlet (inlet1), an oxygen inlet (inlet 2), and pipe diameters of $\Phi 1 = 0.01$ m and $\Phi 2 = 0.02$ m. The sectional diameter of the material inlet (inlet 3) was $d = \Phi 1 = 0.01$ m. The sectional diameters of the straight pipelines were $d_1 = d_2 = 0.05$ m. The lengths of the straight pipelines in front and behind the throat were $L_3 = 0.15$ and $L_4 = 0.3$ m, respectively. The throat diameter was $d_e = d_1/2 = 0.025$ m, length $(4*d_e) = 0.1$ m; the length of the diameter-variable pipeline was $L_1 = L_2 = 0.14$ m (tan 8° < [0.5* $(d_1-d_e)/L_1$] <tan 20°), $L_5 = 0.02$ m. The sectional diameter of the outlet was 0.05 m. We chose a grid division of 230k in the simulations.
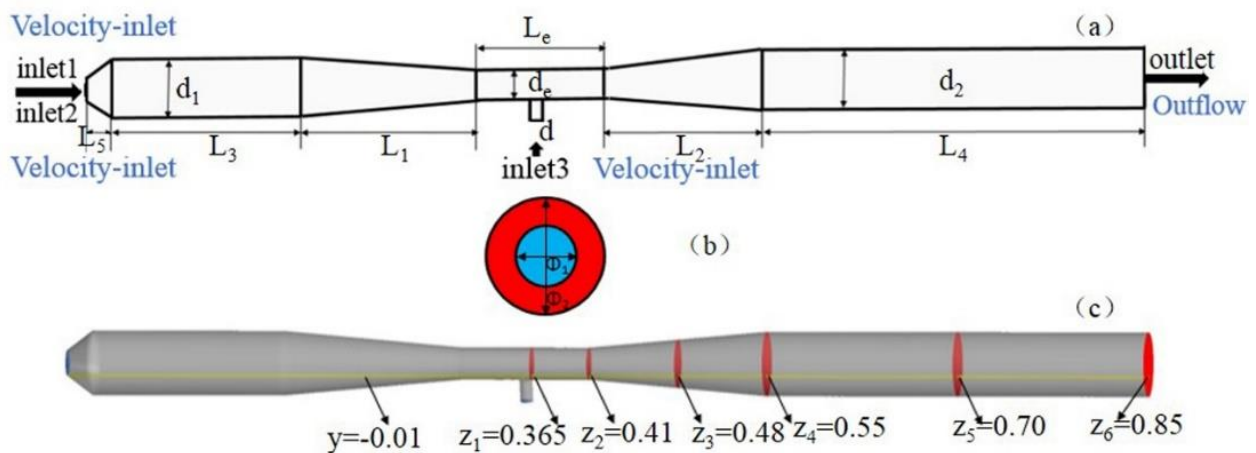
Figure 1. Jet-flow pyrolysis reactor (a) dimension (b) section of gas-phase inlet (c) monitoring line and monitoring surface.

ANSYS 14.5 software was used for the numerical simulation. The simulations were based on a 3D non-steady algorithm, an Euler multi-phase flow model, and volume-finite discrete differential equations. The control equations were differentially treated using a second-order upwind scheme; all items converged to 10^{-4} except for energy (to 10^{-6}). This study focused on $FeCl_2$ and $FeCl_3$ pyrolysis inside the reactor, and the main reactions included:

$$H_2O(l) \rightarrow H_2O(g) \tag{1}$$

$$HCl(l) \rightarrow HCl(g) \tag{2}$$

$$CH_4(g) + 2O_2(g) \rightarrow CO_2(g) + 2H_2O(g) \tag{3}$$

$$2FeCl_2(s) + 2H_2O(g) + 1/2O_2(g) \rightarrow Fe_2O_3(s) + 4HCl(g) \tag{4}$$

$$2FeCl_3(s) + 3H_2O(g) \rightarrow 2Fe_2O_3(s) + 6HCl(g) \tag{5}$$

$$2C_6H_8O_7 + 9O_2(g) \rightarrow 12CO_2(s) + 8H_2O(g) \tag{6}$$

$$6Fe_2O_3(s) \rightarrow 4Fe_3O_4(s) + O_2(g) \tag{7}$$
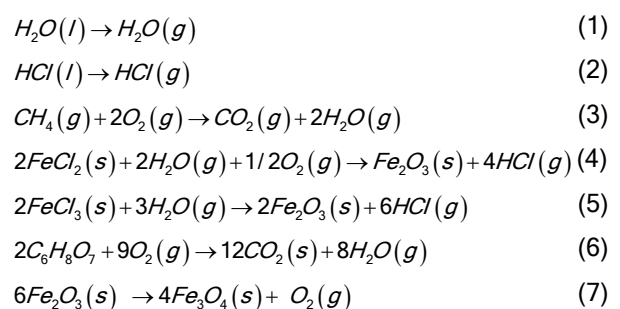
We used UDFs to simulate these processes, employing the boundary conditions summarized in Table 1 and CH_4, O_2, CO_2, HCl(g), H_2O(g), HCl(l), H_2O(l), $FeCl_2$, $FeCl_3$ and Fe_2O_3 as the chemical species involved in the reactions. The physical parameters of all substances were identified by searching inorganic thermodynamics manuals [16]; the particle sizes of Fe_2O_3 and Fe_3O_4 were up to 1 μm. $C_6H_8O_7$ was customized according to its physical properties. The boundary conditions are shown in Table 1.

Table 1. Boundary conditions

	CH_4 inlet	O_2 inlet	Material inlet	Outlet
Condition	Velocity-inlet	Velocity-inlet	Velocity-inlet	Outflow
Value (m/s)	2.88	31.73	0.015 (10% $FeCl_2$, 10% $FeCl_2$, 5% HCl)	
Value (m/s)	2.88	31.73	0.015 (10% $FeCl_2$, 10% $FeCl_2$, 5% HCl, 5%–9% $C_6H_8O_7$)	

RESULTS AND DISCUSSION

Result validation

The mass flow rate at the outlet of the Venturi reactor maintained steady when the simulated time reached 60 s. As shown in Figure 2, when comparing the flow rates of HCl, Fe_2O_3, and Fe_3O_4 collected at the outlet, the numerical simulation exceeds the experimental physical value, which is caused by the loss of the mixed solution and measurement errors caused by the recovery process. However, the error between the simulation and the experiment results was below 5%, so the model and boundary condition settings for the numerical simulation are accurate.
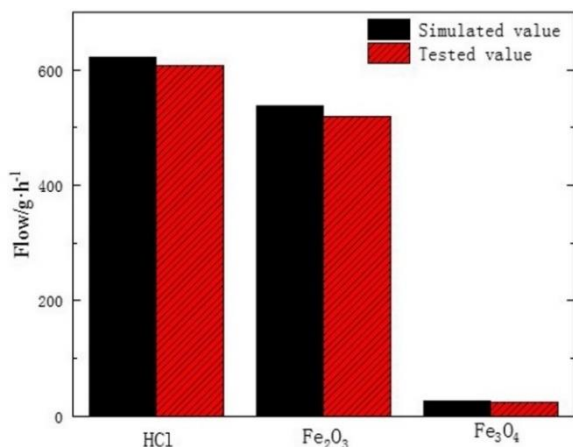
Figure 2. Comparison of product results at the outlet.

Velocity, temperature, and distribution of component concentrations

Figure 3(a) shows the velocity cloud diagram and a velocity vector diagram of the gas phase. Figure 3(a) shows the gas phase velocity maximized at the oxygen inlet and the Venturi throat. Starting from the Venturi throat, a low-velocity area appears in the lower part of the reactor. Figure 3(b) shows the velocity cloud diagram and velocity of the solid phase. Figure 3(b) also indicates the solid phase reached a maximum velocity at the upper right side of the throat. A low-velocity region appears in the lower part of the reactor at the back of the throat due to the vertical collision of the gas and solid phases.

Figure 4 shows the temperature distribution cloud diagrams in the Venturi reactor. The reactor's internal temperature exceeded 2000 K and sufficed for water and hydrochloric acid evaporation from $FeCl_2$ and $FeCl_3$ solutions and pyrolysis. The combustion of methane generated the temperature; the high-temperature zone was concentrated in the first half of the reactor, and the low-temperature zone appeared at the material inlet. The temperature distribution differed from a previous literature report [15] due to a much higher oxygen flow rate.

Figure 5 shows a cloud diagram of the concentration distribution for each component in a

Figure 3. Velocity field distributions.
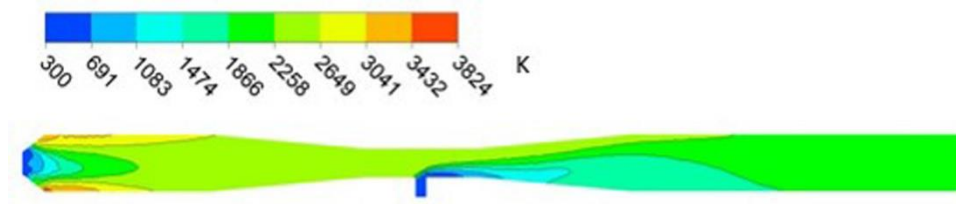
Figure 4. Temperature field distribution.

Figure 5. Distribution of component concentrations.

Venturi reactor and methane concentrated primarily at the methane inlet. As the combustion reaction progressed, methane reacted completely, and the concentration dropped to zero. Oxygen concentrated mainly at the oxygen inlet, and most of the oxygen reacted as combustion progressed. The oxygen produced by Eq. (7) will participate in the chemical reaction according to Eqs. (6) and (4). Therefore, the residual oxygen content was too low obviously in the throat. Carbon dioxide was produced and accumulated with the addition of CO_2 generated by the pyrolysis of citric acid at the Venturi throat; this resulted in a high CO_2 concentration distribution area at the rear of the throat. Evaporation from the hydrochloric acid solution and pyrolysis of cerium chloride produced hydrogen chloride and reached its peak concentration in the latter half of the Venturi throat. The high concentration area of $FeCl_2$, $FeCl_3$, and $C_6H_8O_7$ was concentrated mainly at the inlet. As pyrolysis continued, $FeCl_2$, $FeCl_3$, $C_6H_8O_7$ completely reacted, and their concentrations dropped to zero. Pyrolysis produced Fe_2O_3 and was distributed primarily in the second part of the Venturi reactor. After citric acid addition, Fe_3O_4 was present in the Venturi reactor, albeit at low levels, and indicated that only part of Fe_2O_3 underwent a secondary reaction during pyrolysis. The density of Fe_3O_4 was higher than Fe_2O_3, and that high concentration was localized in the lower part of the pipe.

The concentration changes of CO_2, Fe_2O_3, and Fe_3O_4 on the monitoring line were investigated to analyze the product distributions in the reactor further. Figure 6 shows that CO_2 was produced as combustion of methane proceeded and accumulated with CO_2 generated by $C_6H_8O_7$ decomposition. The concentration of CO_2 at the throat of the Venturi increased rapidly and maximized before decreasing and finally leveling off. The distribution of CO_2 concentrations on the monitoring line was higher than in a previous report [15] because the oxygen velocity was higher, and the high CO_2 concentration area was localized near the reactor wall. After citric acid addition, some Fe_2O_3 in the Venturi reactor reacted to afford Fe_3O_4; however, the total number of Fe ions in the product remained unchanged from the Fe ions added to the material inlet. Therefore, the concentrations of $FeCl_2$ and $FeCl_3$ at the material inlet were consistent with the literature values [15]. Also, the total amount of Fe ions in Fe_2O_3 and Fe_3O_4 agreed with previous literature values [15].

Effects of citric acid levels

Figure 7(a) shows that flow rates of Fe_2O_3 and Fe_3O_4 increased when the reactor was closer to the outlet. Changing the amount of $C_6H_8O_7$ added affected the flow ratio of Fe_2O_3 and Fe_3O_4. Adding 7% $C_6H_8O_7$ resulted in the highest Fe_3O_4 flow rate. As seen in Figure 7(b), increasing citric acid levels caused the flow rate of Fe_2O_3 to increase then decrease; however, the flow rate of Fe_3O_4 initially decreases then increases, and the total Fe ion levels at the outlet remained unchanged. When citric acid levels were 7%, the flow rate of Fe_2O_3 was minimum, and the flow rate of Fe_3O_4 was maximum.
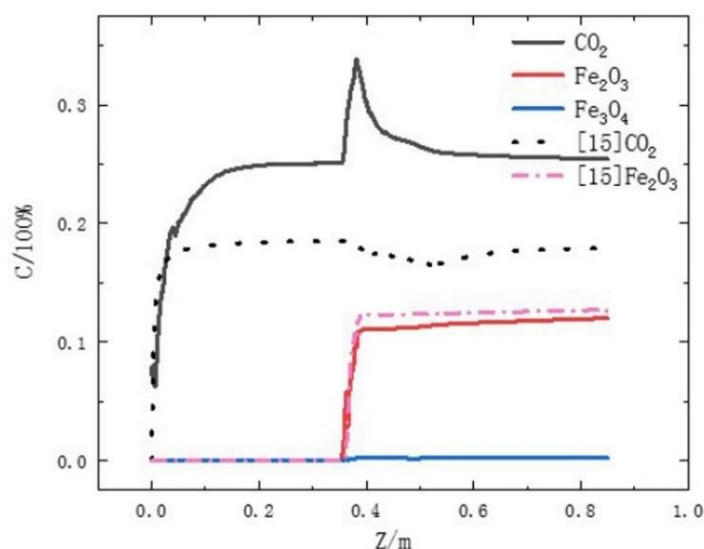
Figure 6. Concentration distribution on the monitoring line.

CHAO *et al.*: SIMULATION STUDY OF CITRIC ACID EFFECTS ON....

Chem. Ind. Chem. Eng. Q. 29 (1) 53–59 (2023)
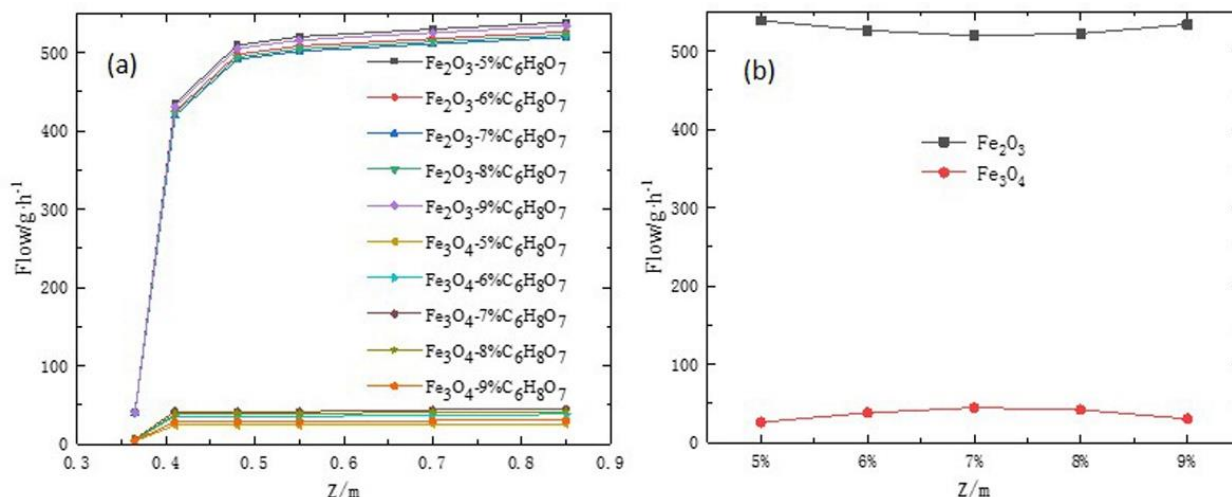
Figure 7. The relationship between the amount of citric acid added and the product (a) at different positions (b) at the outlet.

CONCLUSION

When citric acid was added to the inlet, CO_2 produced by pyrolysis of citric acid and methane combustion combined, and the peak concentration was reached in the back half of the Venturi throat. With the addition of citric acid, part of the Fe_2O_3 in the Venturi reactor underwent a secondary reaction to afford Fe_3O_4, the density of Fe_3O_4 was higher than Fe_2O_3, and that high concentration was localized in the bottom of the pipe. However, the total amount of Fe ions in the product remained unchanged from the Fe ions added at the inlet. As citric acid levels increased, the flow rate of Fe_2O_3 initially increased and then decreased, while the flow rate of Fe_3O_4 first decreased and then increased. Citric acid levels of 7% resulted in the lowest flow rate for Fe_2O_3 and the highest flow rate for Fe_3O_4.

ACKNOWLEDGMENTS

REFERENCES

[1] J. Peng, Y. Zhu, D.F. Zhang, Inor. Chem. Ind. 07 (2019) 81–84.

[2] Y.T. Hong, L. Qiao, X.H. Liu, Mod. Chem. Ind. 01 (2005) 48–50.

[3] A.J. Sushilkumar, B Roberta, L.M. Daniele, F. Daniela, E. Christian, Pigm. Resin. Tech. 04 (2014) 219–227. https://doi.org/10.1108/PRT-07-2013-0057

[4] M. A. Ali, M. M. Uddin, M. N. I. Khan, F.U.Z. Chowdhury, S.M. Hoque, S.I. Liba, Chin. Phy. B. 07 (2017) 377–343. https://doi.org/10.1088/1674-1056/26/7/077501

[5] X. Han, L.L. Wang, L. Wang, X.D. Wang, D.Q. Zhao, J. Chin. Ceram. Soc. 07 (2020) 1097–1106. https://doi.org/10.14062/j.issn.0454-5648.2020.07.20190682

[6] Y. Aylin, V.B. Derman, A. Riza, A.A. Ozgur, A. K. Mine, E. Ugur, M. Carl, H.R.L. Appl. Surf. Sci. 521 (2020) 146332. https://doi.org/10.1016/j.apsusc.2020.146332.

[7] S. Yousefinejad, H. Rasti M. Hajebi, M. Kowsari, S. Sadravi, F. Honarasa, Sens. Actuators, B 247 (2017) 691-696. https://doi.org/10.1016/j.snb.2017.02.145.

[8] C.X. Cui, Coal. Chem. Ind, 11 (2010), 37–38.

[9] Y.T. Liu, F.Z. Liu, W. Du, G.M. Lu, J.G. Yu, J. Mater. Sci. Eng. 6 (2018) 1010-1015.

[10] AlShammari A. S., Halim M.M., Yam F.K., K. N. H. Mohd, Mate. Sci. Semi. Proc, 116 (2020) 1–6. https://doi.org/10.1016/j.mssp.2020.105140

[11] A. Moumen, B. Hartiti, E. Comini, Z.El Khalidi, H.M.M.M. Arachchige, S. Fadili, P. Thevenin, Supe. micr, 127 (2019) 2–10. https://doi.org/10.1016/j.spmi.2018.06.061

[12] Lv, C., Zhang, T. A., and Dou, Z. H., Rare Metals, 12 (2019) 1160–1168. https://doi.org/10.1007/s12598-019-01337-9

[13] C. Lv, T.A. Zhang, Z.H. Dou, Q.Y. Zhao, J. Mate, 5 (2019) 1660–1666. https://doi.org/10.1007/s11837-019-03397-9

[14] C. Lv, J. Mate, 12 (2019) 4944–4949. https://doi.org/10.1007/s12598-019-01337-9

[15] G.S. Yang, X. Bian, L.X. Cui, B. Xie, Y.L. Yao, W.Y. Wu. Chin. Rare. Earths, 01 (2017) 72–78. https://doi.org/10.16533/J.CNKI.15-1099/TF.201701013

[16] D.L. Ye, Beijing: Metallurgical industry press, (1981) 250–257. (in Chinese).

CHAO *et al.*: SIMULATION STUDY OF CITRIC ACID EFFECTS ON....

Chem. Ind. Chem. Eng. Q. 29 (1) 53−59 (2023)

LV CHAO[1,2]
YIN HONGXIN[2]
SUN MINGHE[2]
ZHU HANGYU[1]

[1]Key Laboratory for Ferrous Metallurgy and Resources Utilization of Ministry of Education, Wuhan University of Science and Technology, Wuhan, China

[2]School of Control Engineering, Northeastern University at Qinhuangdao, Hebei, China

NAUČNI RAD

SIMULACIJSKO ISTRAŽIVANJE EFEKATA LIMUNSKE KISELINE NA PIROLIZU OTPADNOG LUGA IZ NAGRIZANJA HLOROVODONIČNOM KISELINOM

Tokom pirolize otpadnog luga iz nagrizanja gvožđa i čelika hlorovodoničnom kiselinom u Venturijevom reaktoru proizvodi reakcije aglomeriraju i ometaju obradu proizvoda. Dodavanje limunske kiseline materijalima na ulazu poboljšalo je distribuciju proizvoda. U ovom radu je sprovedena numerička simulacija sagorevanja, promene faze i hemije gasno-čvrsto vezane za obradu otpadnog luga iz procesa nagrizanja limunskom kiselinom. Ovi rezultati su pokazali da limunska kiselina, dodata na ulazu, dovodi do maksimalne koncentracije CO_2 u drugoj polovini Venturijevog grla, dok je deo Fe_2O_3 je podvrgnut sekundarnoj reakciji u kojoj nastaje Fe_3O_4. Kako se količina dodate limunske kiseline povećava, prinos Fe_2O_3 na izlazu se prvo povećava, a zatim smanjuje, dok se prinos Fe_3O_4 prvo smanjuje, a zatim povećava. Kada je odnos limunske kiseline bio 7%, prinos Fe_2O_3 je bio najmanji, a prinos Fe_3O_4 najveći.

Ključne reči: piroliza, limunska kiselina, Fe_2O_3, Fe_3O_4, numerička simulacija.

SAHRA HAMDOLLAHI
LUO JUN

School of Mechatronic
Engineering and Automation,
Shanghai University, Shanghai,
China

A REVIEW ON MODELING OF PROTON EXCHANGE MEMBRANE FUEL CELL

Article Highlights
- Simplicity is one of the specifications of empirical/semi-empirical models
- The analytical models are helpful for one-dimensional designs with short-time computing processes
- Mechanistic models explain the basic actions of a fuel cell, like the distribution of current density
- The present study enlightens the importance of combining different modeling strategies
- Optimization algorithms like genetic algorithms are used to increase the precision of the model

Abstract

Fuel cells are electrochemical devices that convert chemical energy into electrical energy. Among various fuel cells proton exchange membrane fuel cell (PEMFC) is considered one of the most promising candidates for the next generation power sources because of its high-power densities, zero-emission, and low operation temperature. In recent years, modeling has received enormous attention and interest in understanding and studying the PEMFC phenomena. This article reviews recent progress in PEMFC modeling. Empirical/semi-empirical, analytical, and mechanistic models, zero-to-three dimensional models, and multiphase flow models, such as multiphase mixture, multi-fluid, and VOF models, are different types of PEMFC modeling approaches, respectively, in terms of parametric, dimensional and two or three-phase flow. The present study enlightens the importance of combining different modeling strategies and parameter identification in PEMFC modeling to achieve precise models to reduce the time and cost of experiments.

The serious condition of climate change and global warming in the 21st century is mainly because of the drastically increasing amount of carbon dioxide in the earth's atmosphere. The reason for this incident is the growth in fossil fuel-based energy consumption through inefficient converters and conventional energy. Therefore, detecting a new energy converter, which is low pollution emission and high energy conversion efficiency, becomes a significant matter. Among

numerous possibilities, fuel cells that convert chemical energy directly into electrical energy through electrochemical reactions without including any moving part are one of the most encouraging energy converters in the coming years [1].

Full cells have 40–50 % higher energy conversion efficiency and less noise than internal combustion engines because fuel cells do not have moving parts [2]. Proton exchange membrane fuel cells (PEMFCs), alkaline fuel cells (AFCs), direct methanol fuel cells (DMFCs), molten carbonate fuel cells (MCFCs), phosphoric acid fuel cells (PAFCs), and solid oxide fuel cells (SOFCs) are various kinds of fuel cells [3]. PEMFCs have attracted the most attention and investment among the six fuel cell types. PEMFCs, working at low temperatures (60–80 °C), are more appropriate for portable and automotive power

applications. PEMFCs are featured by zero emissions, low noise, easy scale-up, rapid startup, and high-energy conversion efficiencies. The schematic view of a PEMFC is shown in Figure 1.

Fundamentals of PEMFCs

A PEMFC is an appealing choice for various fuel cell types as a strong contender for an alternative clean energy generation for stationary and automotive applications. It is mainly because of PEMFC's rapid startup, low operating temperature, low pressure, high efficiency in energy conversion with zero greenhouse gas emission, and high power density [4,5]. However, for a PEMFC's wide-range commercialization, several technological obstacles must be overcome, including cell durability and degradation triggered by water and heat management problems [5,6]. Therefore, the cell performance of PEMFCs is mainly determined by numerous factors, including the manufacturing process, the mechanical design, the electrochemical reaction kinetics, the transport phenomena in the cells, and the operating conditions [7].
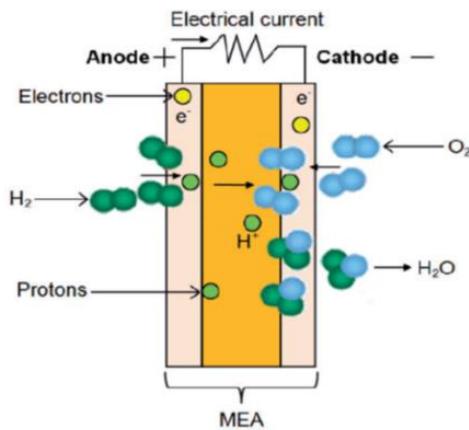
Figure 1. A schematic view of operation in PEMFC [8].

Governing equations for PEMFC modeling

The electrochemical reaction that occurs in the PEMFC [7]:

On the anode side: $2H_2 \rightarrow 4H^+ + 4e^-$

On the cathode side: $O_2 + 4H^+ + 4e^- \rightarrow 2H_2O$

Reaction in the cell: $2H_2 + O_2 \rightarrow 2H_2O$
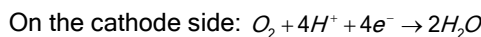
Mass, momentum, chemical species, ionic and electrical current, and thermal energy are the physical quantities transported in a PEMFC. For example, three-dimensional PEMFC transport equations are given as follows [8]:

Continuity equation:

62

$$\frac{\partial(\rho u)}{\partial x} + \frac{\partial(\rho \upsilon)}{\partial y} + \frac{\partial(\rho \omega)}{\partial z} = -\frac{\partial \rho}{\partial t}$$

where velocity in the x, y, and z directions present respectively by u, v, and ω, ρ is the density of reactant gases. The continuity equation concerns membrane and electrode porosity (ε).

$$\frac{\partial(\rho \varepsilon u)}{\partial x} + \frac{\partial(\rho \varepsilon \upsilon)}{\partial y} + \frac{\partial(\rho \varepsilon \omega)}{\partial z} = S_m$$

Mass conservation:

In the gas diffusion layers and gas channels, there is not happening any reaction therefore S_m (kg m^{-3} s^{-1}) that presents mass source term is considered as zero. The next equations calculate the mass source term in the catalyst layer because there is a reaction of reactants; therefore, the mass source term is not zero. Mass source terms for hydrogen, oxygen, and the dissolved water content (λ) in the catalyst layer are:

For gas channels and GDLs: $S_m = 0$

For the anode catalyst layer: $S_{H_2} = -\frac{M_{H_2}}{2F} R_{an}$

For the cathode catalyst layer: $S_{O_2} = \frac{M_{H_2O}}{2F} R_{cat} - \frac{M_{O_2}}{4F} R_{cat}$

where M is the molecular weight (kg/mol) of the species and F is the Faraday constant.

Momentum Conservation:

$$\frac{\partial\left(\varepsilon \rho \vec{V}\right)}{\partial t} + \nabla\left(\varepsilon \rho \vec{V}\vec{V}\right) = -\varepsilon \nabla P + \varepsilon \mu \nabla^2 \vec{V} + S_m$$

where μ is the dynamic viscosity, S_m is the source term of momentum conservation, and P is the pressure. For porous media, the momentum conservation equation can be written as follows:

$$S_m = -\frac{\mu}{K}\vec{V}$$

where K is the permeability.

Species conservation:

$$\frac{\partial(\varepsilon \rho \omega_k)}{\partial t} + \nabla\left(\varepsilon \rho \omega_k \vec{V}\right) = -\nabla\left[\left(D_k \nabla\left(\rho \omega_k\right)\right)\right] + S_k$$

where ρ is density, S_k is the species source term, ω_k is the species concentration, and D_k is the species diffusion coefficient.

The species source term for the liquid water is:

For gas channels and GDLs: $S_k = 0$

For the catalyst layers: $S_{H_2} = -\frac{1}{2F} R_{an}$, $S_{O_2} = -\frac{1}{4F} R_{cat}$,

$S_{H_2O} = \frac{1}{2F} R_{cat}$.

Energy conservation:

$$\frac{\partial(\varepsilon \rho c_p T)}{\partial t} + \nabla\left(\varepsilon \rho c_p T \vec{V}\right) = \nabla\left(k \nabla T\right) + S_E$$

where k is the thermal conductivity, T is the temperature, c_p is the specific heat at constant pressure and S_E is the energy source term.

Electrical current:

$$-\nabla\left(\sigma_e \nabla \phi_e\right) = S_e$$

Ionic current:

$$-\nabla\left(\sigma_i \nabla \phi_i\right) = S_i$$

where S_E and S_i are respectively the electron and proton flow source term, Φ_E and Φ_i are the solid phase potential and membrane phase potential and σ_E and σ_i represent the electrical conductivity.

Butler-Volumer equation can calculate the transfer current. In the anode $S_m = R_{an}$ and $S_e = -R_{an}$; however, on the cathode side $S_m = -R_{cat}$ and $S_m = -R_{cat}$.

Current density in anode and cathode are as followings:

$$R_{an} = R_{an}^{ref}\left(\frac{c_{H_2}}{c_{H_2}^{ref}}\right)^{\gamma_{an}}\left[\exp\left(\frac{\alpha_{an,an}F\eta_{an}}{RT}\right) - \exp\left(\frac{\alpha_{cat,an}F\eta_{an}}{RT}\right)\right]$$

$$R_{cat} = R_{cat}^{ref}\left(\frac{c_{O_2}}{c_{O_2}^{ref}}\right)^{\gamma_{cat}}\left[\exp\left(-\frac{\alpha_{cat,cat}F\eta_{cat}}{RT}\right) - \exp\left(\frac{\alpha_{an,cat}F\eta_{cat}}{RT}\right)\right]$$

where, η is the local surface overpotential, γ_{an} and γ_{cat} are concentration dependence, α is the transfer coefficient and R_{an}^{ref} and R_{cat}^{ref}, respectively, are the reference current density of anode and cathode.
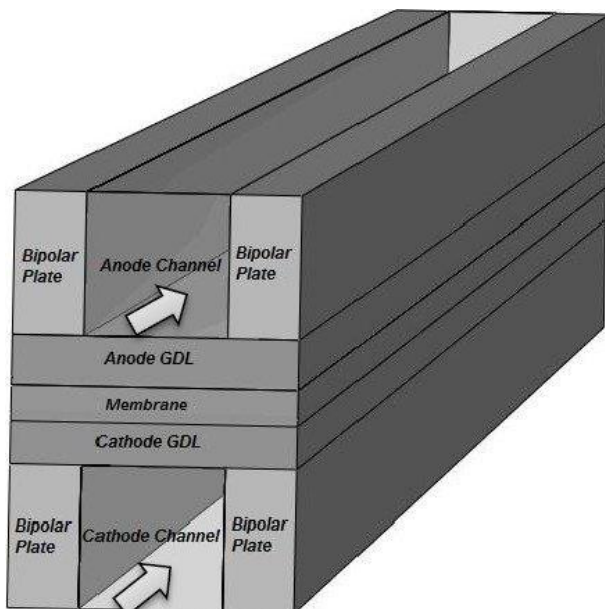
Figure 2. Schematic view of three-dimensional PEMFC model [9].

The combination of thermodynamics, fluid dynamics, and electrochemistry create a complicated system, which is PEMFC. To understand fuel cells' dynamic and static behavior, the mathematical models greatly help estimate control strategies and optimize fuel cells' design. In addition, by applying mathematical models to study fuel cells, there is a reduction in experimental tests, saving time and effort. In these models, the influence of temperature distribution, thermal stress, operating conditions, and other variables could be understood simply through the simulation.

In recent years, modeling has received colossal attention and interest in understanding and studying the fuel cell phenomena. To reduce the time and cost of experiments, fuel cell designers and engineers could get the benefits of using parametric models to predict the fuel cell performance by given operating conditions, geometries, and properties of materials. There are three types of fuel cell models in terms of parametric: empirical/semi-empirical, analytical, and mechanistic. In the following section, these models are described, and the methods that have been applied recently for their optimization are explained. The two other modeling approaches which explain the models in terms of dimensional and phase change are respectively zero to three-dimensional models and multiphase models and are described in this paper.

PEMFC models

Empirical/semi-empirical

There is enormous interest in PEMFC modeling, which saves time and effort as its simulation results will significantly agree with experimental ones [10]. Figure 2 demonstrates a three dimensional PEMFC model. Each application and operating condition has specific features based on experimental data called empirical/semi-empirical models. The details presented by these models are not more than theoretical ones; though, they have a quite favorable advantage in modeling fuel cells and other engineering fields. The empirical/semi-empirical models are designed for particular fields and should be changed for every operating condition or application. For example, the polarization curve of PEMFC, described by 0-dimensional models, are empirical and simple models [11]. Semi-empirical and 0-dimensional models are suitable for beginner researchers trying to find a model for the fuel cell. Simplicity is one of the specifications of empirical/semi-empirical models, and in some fields, these models illustrate better performance than theoretical models [12]. For example, the overpotential of output voltage significantly impacts the reduction factor of fuel cell output [13]. The computation of ohmic overpotential is simplified in empirical/semi-empirical models. The main emphasis of empirical/semi-empirical models is on the correlation between input and output. Besides, these models provide a calculation for the performance of PEMFC in a short time [14]; therefore, the empirical/semi-empirical models are more suitable for problems that focus on controlling.

Analytical models

The analytical models are useful for simple and one-dimensional designs with short-time computing processes and calculating water management and voltage losses [15]. However, the results of analytical models may not be excessively precise. The advantage of analytical models is introducing practical surveys for certain conditions, which provide information easily without requiring a numerical program to run in many cases. However, when the analytical solutions exclusively work for specific elements like catalyst layers and calculate their potential, oxygen concentration, and current density, they neglect the interactions with other parts of PEMFCs [16]. Tafel kinetics and potentials, which are close to open-circuit, are the conditions for achieving the analytical solutions. Furthermore, the analytical approach does not include membrane resistance or mass transport restrictions, which are important for PEMFC performance. By utilizing just mathematical models because of nonlinear problems, it is hard to solve the PEMFC problems, though numerical approaches can solve them. In other words, for every problem, there are computational requirements and a wide range of meshing [17].

Mechanistic models

The difficulty of modeling the PEMFC systems is because they are electrochemical, nonlinear, and multivariable systems [18]. For their explanation, it is necessary to understand internal phenomena at the molecular level of PEMFC. Therefore, the publications aim mainly at the internal phenomena of the PEMFC systems and introduce a model for describing this target. The mechanistic model focuses on thermodynamics, fluid dynamics, and electrochemistry. Being theoretical, these models apply the Stefan-Maxwell, Nernst-Planck, and Butler-Volmer equations for gas phase, species transport, and cell voltage, respectively [19]. In addition, mechanistic models explain the basic actions of a fuel cell, including flow pattern, pressure drop, distribution of current density, and voltage.

The mechanistic models are rigorous in calculations because of the fundamental and partial differential equations they need in a repetitive method to solve a problem. The complexity in mechanistic model confirmation is because it is impossible to compute the pressure, temperature, concentration of species, and other important parameters in a fuel cell with an extreme environment.

By applying electrochemical or physical equations, the operating conditions in PEMFCs occur in mechanistic models. The mechanistic models do not fit applications that aim for control; however, they are

suited for optimization and design applications. Furthermore, there are no huge differences between mechanistic and empirical models [19].

Lu [20] indicated that by using both empirical and mechanistic techniques as combination models, predicting the performance of the PEMFCs becomes more effective. The reason to use a hybrid model that consists of mechanistic and empirical approaches is that the usage of both approaches has advantages in improving the model and defeats the disadvantages of each of them. For example, in a hybrid model, the parameters for operation are reduced because of the fewer input dimensions. The other advantages of the combined model over the empirical and mechanistic model are that it can easily be utilized for any operating condition and application without requiring extensive range calculation.

Optimization methods in PEMFC models

System parameters, different flow field designs, and operation conditions affecting the PEMFC's performance can be analyzed using mathematical modeling and computational tools. The complexity of mechanistic fuel cell models is why they are difficult to use in a simulation. However, the precise empirical/semi-empirical models are suitable and easy for simulation.

The results of different studies in recent years show that to examine the PEMFC performance, the effective and suitable model is parametric. Therefore, to achieve the best performance, the precise model parameter identification of PEMFCs is significant and possible by applying different algorithms [21].

The latest researchers have paid huge attention to fuel cell optimization by classifying different parameters and models, like a genetic algorithm (GA) and other evolutionary computation techniques. These techniques increase the precision of model parameter identification in the fuel cell.

Abdi *et al.* [22] presented particle swarm optimization (PSO) as a practical algorithm. The PSO, in comparison with GA, has better and more precise performance in the convergence of problems by providing global and stable optimization solutions. Furthermore, as a straightforward algorithm, the PSO is useful for successfully optimizing the extensive collection of tasks. Similarly, multidimensional elements with velocity and location can be modeled by PSO.

Different modeling techniques and strategies to study the dynamical and statistical performance of fuel cells are changed by varying the purpose of the study. Many of these modeling approaches to examine the

heat and water management, membrane, electrodes, and cathode performance are highly important to the mechanical and chemical phenomenon. By simulating and studying these modeling techniques, the most favorable operating conditions, high and developed performance, and durability of the fuel cell can be achieved. However, because of the complexity of mechanistic models, implementing these models requires quite a huge amount of parameters that indicate the technology and physics of materials engaged.

In fuel cells' procedure to express the electrochemical and physical phenomena, another model depends on empirical/semi-empirical equations. This model is more appropriate for analyzing fuel cell systems. The critical and challenging point for fuel cell application designers is identifying every parameter for each fuel cell. Empirical nature and technological nature are two types of parameters that should be identified for the fuel cell. Because of the difficulty and complexity of the parameters and identification process, some designers apply values for parameters, and the simulation results are achieved with medium quality. Recent years' promising solution is an optimization method that achieves the identifying parameters in fuel cell systems. Intending to solve real problems, modified particle swarm optimization (MPSO), as a nature-inspired algorithm, is suitable for many engineering applications [23]. The optimal result can be attained by applying MPSO and classifying different parameters for a semi-empirical PEMFC model. Furthermore, to gain the results of a simulation with high accuracy is a rigid mission for extensive operation conditions. The MPSO technique can identify and calculate the parameter's value for a PEMFC under different temperatures and normal conditions [23].

For parameter optimization of real problems, a simple and efficient technique is a Hybrid adaptive differential evolution (HADE) algorithm [21]. For identifying the PEMFC model parameters, the HADE algorithm initiates a dynamic crossover possibility and an adaptive scale factor to progress the convergence of the simulation. As a result, the performance of the HADE algorithm in space with high or low dimensions and comparison with GA, PSO, and a standard and adaptive DE algorithm is better and more reliable.

The Simulink technique, which is applied in Matlab-SIMULINK, is suitable for various operating conditions and fuel cell systems. Moreover, it is easy to apply for different applications; because this modeling is simple, and there is no need for extensive time for computation [24].

The best model for designing, developing, optimizing, and calculating the performance of fuel cells

is a mathematical model. Several studies are about one or three-dimensional, non-isothermal, and non-isobaric mathematical models and identify separate parameters like liquid water transportation, thermal conduction, and gaseous diffusion. In real-time design control applications, applying these models is problematic and complex because they identify parameters for material structure. A steady model, achieved from mechanistic models and can identify the voltage-current features, is unsuitable for real-time control design. PSO algorithm [25] was developed to suit a model for real-time control design applications. LM algorithm can simply be trapped in the minimum neighborhood. The PSO algorithm is established to solve this problem. The PSO and LM algorithms can be used at the beginning of the global and local search stage. For that reason, a hybrid algorithm that consists of LM and PSO algorithms can be used for optimization. This hybrid algorithm can investigate the PEMFC model with voltage and temperature parameters. The advantage of a hybrid algorithm is that it sets aside both algorithms' disadvantages and failing points and attains the application's aim. Furthermore, the simulation of the dynamic performance of PEMFC by this hybrid algorithm has high reliability and uniformity compared with a physical model. The other advantage of this hybrid algorithm over other models is that it is not complicated and can make the model prediction happen quickly [25].

The polarization curve depicts the fuel cell voltage-current characteristics, showing the fuel cell performance. The parameters that depend on fuel cell voltage-current characteristics are power conditioning design, simulators design for fuel cell systems, operating conditions optimization, and system controller design. These show the significance of the polarization curve for the fuel cell. The physical models of fuel cells use electrochemical or empirical mechanisms. The electrical revolution model for fuel cells, uses an electrical element's circuit to depict voltage-current characteristics. Another model that utilizes mathematical strategies to obtain steady-state and high accurate voltage-current characteristics is the mathematical model. The PEMFC model with dynamic voltage-current characteristics and steady state-integrated mathematical model derives from a technique with the smallest squares by electrochemical equations where other input parameters can be computed. In addition, the modeling can be very effective in optimizing output power, power-conditioning design units, operation points, and simulation of PEMFCs [26].

As the PEMFC performance is studied in a short time, in comparison with experimental study, the

modeling of PEMFC attains much interest among the researchers. But unfortunately, a particular PEMFC has various parameters which are unidentified. This problem causes trouble in illustrating the polarization curve; it needs to identify each parameter for the PEMFC model exactly.

As mentioned before, there are not sufficient and precise statistics and rates for particular PEMFC model parameters, which makes inaccuracy in PEMFC performance in a wide range when comparing the real PEMFC with the model. Therefore, the optimization approaches have developed with parameters identification as a numerical problem to obtain the most precise PEMFC model and solve the problem. Thus, these optimization techniques have recently attained much attention and interest. However, creating a perfect and accurate multi-parameter, combined dynamic system, and complicated nonlinear PEMFC system is not a simple and unimportant task. Furthermore, the parameters of the model affect PEMFC performance, indicating the importance of accurately identifying various parameters of the PEMFC model by investigating the optimization approaches. Therefore, there is an essential need for a precise and accurate model for studying and enhancing the performance of PEMFCl.

DE (differential evolution) [27] is an optimization approach that is not too complicated to implement and has a few parameters. However, its difficulty, which is the prevention of untimely convergence, highly depends on operators and related control parameters. Nevertheless, it is a valuable technique to implement by merging it with added solutions like adaptive differential evolution. ADE adaptive differential evolution characteristics are high equilibrium between examination and discovering high potential. By setting up the control elements and various operators online, ADE becomes the development version of DE. Compared with DE and other optimization techniques, the results obtained by ADE show that it is in good agreement with the experimental model. Therefore, the ADE algorithm can be a promising strategy to create, control, optimize the PEMFC model, and improve the precision [27].

In every PEMFC system, the parameters should independently be categorized. For this explanation, the empirical equation applies. However, there is huge significance in setting up the parameters in the electrochemical module as they are adjusted in steady-state conditions and where the optimizing reliability of models is the next task after tuning the parameters.

The modules of energy balance, mass balance, and electrochemical phenomena are individual in the PEMFC system. The electrochemical model expresses

the voltage-current actions of PEMFC. When voltage is lost because of numerous issues, the production of maximum voltage in PEMFC is impossible. Ohmic loss, concentration, and activation overvoltage are different losses in models. The loss terms mentioned above lead to the output voltage of the fuel cell, where the Nernst equation computes the thermodynamic potential. The genetic algorithm in the electrochemical models of PEMFC can provide accurate parameters, which leads to trustworthy outcomes [28].

Nernst equation [12]:

$$E = E^0 + \frac{RT}{2F}\ln\left(\frac{p_{H_2}p_{O_2}^{1/2}}{p_{H_2O}}\right)$$

where p is the partial pressure of H_2, O_2 and H_2O.

The PEMFCs need a precisely adjustable model to design steady-state, dynamic, and control simulations because the output voltage of PEMFCs is not regulated. The typical modeling strategy is to achieve an accurate thermal PEMFC model by considering the fuel cell's mass and momentum's conservation, thermodynamics, and physical power concepts. However, in real-time studies, because of some parameters in nature that cannot be computed in the model, these classic models are unsuitable for such applications. Therefore, to develop models to achieve high accurate performance results in comparison with real PEMFCs, it is necessary to identify the values of parameters in the models precisely.

Different meta-heuristic approaches have been investigated in recent years for identifying parameters in the PEMFC models. The dragonfly algorithm, genetic algorithm, Multi-verse optimizer, differential evolution, particle swarm optimization, and many other optimization approaches are examples of meta-heuristic methods for accurate parameter identification in PEMFCs. Although these meta-heuristic methods are more capable of enhancement, they are trendy because they produce highly accurate results in PEMFCs. The benefits of this algorithm are the closeness of the parameter values to the actual computed values and the short convergence time. Therefore, the PSO [29] is a secure, capable, precise, and valid optimization approach for PEMFC.

A predictive control system is essential for output power to achieve the best effectiveness of fuel cells by optimizing humidity, the pressure of reactants in the membrane, and temperature. The support vector regression machine (SVRM) benefits nonlinear system modeling and makes it valuable in time sequence applications. Furthermore, this optimization approach is part of statistical learning and is sustained by mathematical theory. Therefore, the control system of

PEMFC's output power can be developed by this approach.

In nonlinear population-based optimization applications, PSO is appropriate to apply. The PSO approach needs a small number of parameters, and its implementation is effortless. By modeling the control system for the output power of PEMFC on SVRM and combining it with the PSO algorithm for the optimization process, the produced PEMFC model is more accurate. The need for a short time and short memory in PSO optimization makes this approach suitable and easy to implement. Besides, the mathematical operators that apply in this method are uncomplicated. In results of the studies, which use this optimization approach, are validated, qualified, and successful. In the PEMFC optimization process, it is significant to design a control system to improve the output power by setting up the relative hydrogen humidity [30].

Nowadays, in studies to identify parameters in PEMFCs, bio-inspired optimization approaches achieve much interest and attention. One of the new methods with the features like simple implementation and few parameters is the seagull optimization algorithm (SOA) [31], which is used in nonlinear modeling problems of PEMFCs for parameter identification. Moreover, a balanced SOA (BSOA) can be used instead of the standard SOA to improve the convergence of the application. In modeling complicated nonlinear PEMFCs, this technique promises accurate and precise results [32].

Zero to three dimensional PEMFC models

In terms of dimensions, there are four models for PEMFC. The evaluation of the inner quantities of PEMFC because of its spatial dimensions is not a simple task. Computational fluid dynamics (CFD) is a suitable approach to examining every part's temperature gradients, pressure distribution, and species concentrations. The dimensions of the problem, which should be zero, one, two, or three-dimensional, depend on the number of independent spatial variables of the differential equations.

Zero dimensional models

The simplest fuel cell modeling can be achieved by neglecting the spatial alterations, taking time into account, and is called the zero-dimensional or lumped-parameter model. Based on illustrating the polarization curve of PEMFC, zero-dimensional models, which are usually empirical, are uncomplicated in discovering the different losses that occur in the system, comparing them with each other, and concluding the kinetic parameters. Therefore, zero-dimensional and semi-empirical PEMFC models are simple and helpful for

examiners at the start point [11].

To explain the state of health of a PEMFC based on the degradation of the cathode catalyst layer, a zero-dimensional PEMFC model was investigated by Schneider *et al.* [32]. The developed model is suitable for PEMFC design and control because it is fast and reliable and can understand the degradation mechanisms in the cathode catalyst layer. Du *et al.* [33] investigated a method for parametrizing control-oriented zero-dimensional PEMFC. A two-step parameterization method was introduced by separating the model into two sub-models. This method reduces the solution space significantly. Furthermore, parametrizing a fuel cell model with measurement demonstrates an advantage in the sensitivity analysis.

One dimensional model

One dimensional model is the first model that researchers established to study the fuel cell. It was a complicated model with a sandwich domain in the y-direction. These models give massive details in different operating conditions for fuel cells by examining the temperatures, mass concentrations, electrical potentials, and fluxes. A one-dimensional, semi-empirical, and steady-state model of an HT-PEMFC fed with a gas mixture is developed by Nalbant *et al.* [34] to study the effects of different cell temperatures, Pt loading, phosphoric acid percentage, and different binders on the performance of the fuel cell were examined.

In the precise calculation of the PEMFC performance by Sohn *et al.* [35], a one-dimensional PEMFC model has been developed. Instead of three-dimensional with more detailed models, they preferred a macro-scale one-dimensional PEMFC model, which consists of control volumes for the cathode catalyst layer to compute the liquid water production and fuel concentration.

The characteristics and mechanisms of cold start must be understood; therefore, Jiang *et al.* [36] developed a one-dimensional PEMFC model to simulate the PEMFC cold start to improve fuel cells' startup ability and durability. Salva *et al.* [37] used a one-dimensional analytical model to simulate a PEMFC stack to validate the experimental data. Mass transfer of reactants and electrochemistry are the parameters considered in this work.

Two dimensional model

The Sandwich model in the *y-z* or *x-y* directions is a two-dimensional, upgraded version of the one-dimensional model. These two-dimensional sandwich models could examine the influence of channel geometry, bipolar plates, heat, mass transfer, and

HAMDOLLAHI & JUN *et al.*: A REVIEW ON MODELING OF PROTON ON....

Chem. Ind. Chem. Eng. Q. 29 (1) 61−74 (2023)

fluxes on fuel cells. Like three-dimensional models that significantly contribute to fuel cell modeling studies with their precise and accurate results, both one and two-dimensional models can contain conservation equations by choosing boundary conditions cautiously to achieve results with a high range of exactness.

Liu *et al.* [38] developed a PEMFC with two-dimensional analytical models with the dead-end anode to study the effect of cathode parameters on PEMFC performance. Their results show the model's importance in guiding the practical work of PEMFC with a dead-end anode.

Liu *et al.* [39] examined the reactants' mass transfer, gas flow in channels, and electrochemical reactions on the electrodes by developing a two-dimensional analytical model of PEMFC. The results illustrated that the concentration of hydrogen and oxygen in the direction of flow along the channel and in the catalyst layers decreased. They presented that improving PEMFC performance could improve oxygen mass transfer from the cathode channel to the cathode catalyst layer. A two-dimensional model of a low-temperature PEMFC was used to study the effect of bipolar plate geometry on mass transport, current density, and PEMFC performance by Ionescu *et al.* [40].

Three dimensional model

The most appropriate model to analyze PEMFC in every detail, for instance, current density distribution, the influence of flow field design on fuel cell performance, or bipolar plate blockage impact, is the three-dimensional model, which is in the *x-y-z* direction.

Saco *et al.* [41] developed a three-dimensional model to examine the flow field design influence on PEMFC performance. Because of fast water removal from the gas channels, minimum pressure drop, better proton conductivity, and better hydrogen and oxygen consumption, they introduced the straight zigzag flow field with the best performance among serpentine zigzag, serpentine parallel, and straight parallel flow fields.

To study the influence of membrane geometry on PEMFC performance, a three-dimensional PEMFC model has been investigated by Jourdani *et al.* [42]. The numerical results indicated that higher current density could be obtained by a thinner membrane, hydrogen and oxygen consumption, and high water production.

Caglayan *et al.* [43] developed a three-dimensional model for a PEMFC with a 1000 °C–1800 °C range of temperature. Their result showed that because of high membrane proton conductivity and fast reaction kinetics, the increase in temperature improves the PEMFC performance. In addition, they suggested that the current density is uniform in high operating voltage.

Multiphase flow

Fluid flows, which contain two or three phases, including gas-solid flow, liquid-solid flow, gas-liquid flow, and liquid-liquid flow, are different types of two-phase flow. Three-phase flows are gas-liquid-solid flows, gas-liquid-liquid flows, gas-oil-water flows, and solid-liquid-liquid flows. The mass, momentum, and energy transfer occur in the interface that divides different phases. In the PEMFC, the liquid water production and the phase change processes develop by multiphase transport.

The gas phase consists of hydrogen, water vapor, oxygen, and nitrogen. The liquid phase is liquid water in a two-phase PEMFC model study. VOF model, multiphase mixture, multi-fluid, and some other models have been used in the multiphase flow PEMFC modeling studies.

VOF model

The interface in the gas-liquid flow, as shown in Figure 3, is detected and transported by the VOF model. This model recreates the interface profile; then, the interface transportation occurs in the velocity field. The VOF model can record the surface tension as a significant force in the micro-channel flows. The disadvantage of the VOF model is that it is only examined with a gas-liquid interface [9,44,45]. Zero and one, respectively, are the volume fraction for the gas and liquid phase in the VOF model. The continuity, mass, and momentum equations are as follows [9]:

Continuity equation:

$$\nabla \vec{U} = 0$$

Mass conservation:

$$\frac{\partial \gamma}{\partial t} + \nabla \left(\vec{U}_\gamma \right) + \nabla \left[\vec{U}_r \gamma \left(1-\gamma\right) \right] = 0$$

Momentum conservation:

$$\frac{\partial \left(\rho \vec{U} \right)}{\partial t} + \nabla \left(\rho \vec{U} \vec{U} \right) - \nabla \left(\mu \nabla \vec{U} \right) - \left(\nabla \vec{U} \right) \nabla \mu = -\nabla P_d - \vec{g} \vec{x} \nabla \rho + f_s$$
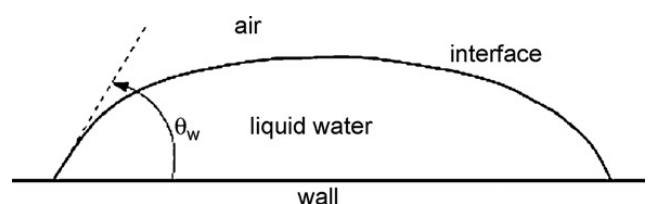
Figure 3. The interface between the gas-liquid phase [46].

Multiphase mixture model

The multiphase mixture model examines a mix of phases instead of separated phases. There is one set of conservation equations for the mixture phase. Among various phases, relative velocity, density, and other mixture quantities are estimated afterward [9].

Mass conservation:

$$\nabla\left(\rho \vec{V}\right)=0$$

Momentum conservation:

$$\vec{V}=-\frac{k}{\rho\mu}\nabla P$$

The density and velocity of the mixture are as follows:

$$\rho=s\rho_1+\left(1-s\right)\rho_g$$

$$\rho\vec{V}=\vec{V}_1\rho_1+\vec{V}_g\rho_g$$

Species conservation:

$$\nabla\left(\gamma_k \vec{Vc}_k\right)=\nabla\left(D_{kg,eff}\nabla c_{kg}\right)-\nabla\left[\left(\frac{w_{kl}}{M_k}-\frac{c_{kg}}{\rho_g}\right)\vec{J}_l\right]+S_k$$

where the convection correction factor γ is a function of the liquid saturation.

Applying the multiphase mixture model is more proficient in the pressure of the gas phase than the pressure of the liquid phase.

Multi-fluid model

The equations for mass and momentum of every phase in the multi-fluid model are solved separately. However, the two phases are coupled because of phase change and relative permeability [9].

Mass conservation:

$$\nabla\left(\varepsilon\rho_g \vec{V}_g\right)=S_{PC}$$

$$\nabla\left(\varepsilon\rho_l \vec{V}_l\right)=S_{PC}$$

Momentum conservation:

$$\vec{V}_g=-\left(1-s\right)\frac{K_g}{\mu_g}\nabla P_g$$

$$\vec{V}_l=-s\frac{K_l}{\mu_l}\nabla P_g-D\left(s\right)\nabla_s$$

In high conditions of saturation, the multi-fluid model works effectively. However, the multi-fluid model tends to be unstable because of the coupled phases and variables in high amounts.

Figure 4. Visualization of two-phase flow in PEMFC channels [47].

Two-phase flow models

Various models based on the water flow in MEA and the gas channels have been investigated to understand water transport within PEMFC [48]. A visualization of two-phase flow in PEMFC channels is illustrated in Figure 4. For example, a steady-state, non-isothermal, and single and two-phase flow PEMFC model, with various temperatures on anode and cathode and extension in cross-section ratio of channel geometry, has been investigated to improve the fuel cell performance [49]. High temperature apparently affects kinetics rise and liquid water reduction and increases PEMFC's performance. The other factors that enhance PEMFC's performance are the gas channel cross-section and the anode side's temperature.

The single and two-phase flow PEMFC model performance are close to each other at low current densities because of the consequence of low transportation of mass and slow reaction rate. High current density causes a reduction in cell voltage. It is detected that mass transport resistance enhancement makes a fast reduction of current density at low voltages. To achieve highly accurate polarization curve estimation, two-phase models are better than single-phase ones.

Zhang *et al.* [50] employed a three-dimensional mathematical model to study the influence of temperature, operating pressure, and relative humidity on PEMFC performance. Also, for processing the liquid water transport in PEMFC, the non-isothermal two-phase flow was simulated. According to the findings in their study, high operating pressure and temperature improve the PEMFC performance. Moreover, two things improve the water removal process: 1) increasing the contact angle at the interface of the GDL/channel and 2) adding the baffles in the cathode channel. Zhang *et al.* [51] presented a multiphase three-dimensional PEMFC model that includes a detailed study of two-phase flow in the PEMFC. The influence of gravity, surface tension, wall adhesion, pressure drop, and mass transport were studied in this simulation. According to their study, there is an improvement in the water removal process by adding baffles in the cathode channel and increasing the contact angle at the interface of the GDL/channel.

CFD software for fuel cell modeling

The measurement of internal quantities of

PEMFC is not a simple task because of its spatial dimensions. However, examination of pressure distribution, temperature gradients, and species concentrations in every part of PEMFC is achievable by utilizing computational fluid dynamics (CFD). Furthermore, the PEMFC performance could be predicted by implementing CFD in various operating conditions.

Fuel cell modeling combines electrochemistry and thermodynamics in porous media over transportation phenomena to the science of material [52]. Improvement of recent computers' calculation abilities and parallel computation make the CFD simulation on a large scale achievable. In fuel cell system investigation, CFD models - influential design devices - have an important role in enhancing robust, effective, powerful, and modern solver algorithms. One fuel cell modeling software with influential pre- and post-processing options is Fluent. By using different solvers, it is possible to apply single or double-precision infinite volume computations. Comsol Multiphysics (FEMLAB), another CFD software, can solve multidimensional PEMFC models by applying chemical engineering modules and using finite elements. MATLAB/Simulink is another suitable software for small-scale fuel cells and parallel computing on a multicore processor. CFD-ACE+, OpenFOAM, and STAR-CD are CFD software based on the finite volume method and suitable for multidimensional fuel cells. NADigest FDEM also provides durable solutions based on a strong error estimation method.

There are several conditions in PEMFC simulation to improve the system's performance. First, one uses different flow field designs [53–55]. Flow field design greatly affects reactants' mass transport and liquid water removal in the gas channels. Therefore, uniform mass transport and distribution of reactants in the flow channel and water transport in the gas channel improve the performance of the PEMFC. Figure 5 is

demonstrated four different PEMFC flow field designs.
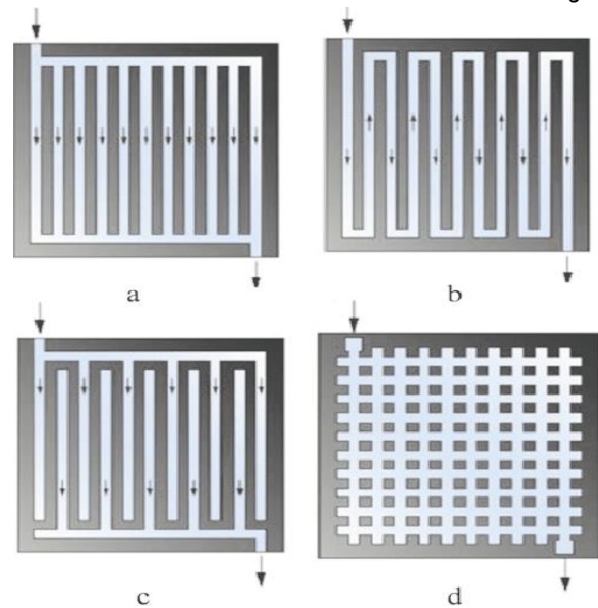
Figure 5. Various types of flow field design, a) Straight channel, b) Serpentine channel, c) Interdigitated channel, d) Pin type channel [56].

The other significant concern that influences PEMFC performance is water management. Different water formation in PEMFC flow channel is illustrated in Figure 6. The amount of water in the PEMFC is a crucial subject; excess water is the reason for flooding in the gas channel, catalyst layer, and gas diffusion layer and causes a problem in reactants transportation. While proton conductivity depends on membrane hydration, inadequate water in the membrane is the reason for membrane dehydration, resulting in a reduction in proton conductivity. There must be a balance between flooding and hydration to enhance PEMFC performance [57]. Figure 7 is shown different sites of PEMFC that are possible for flooding.

Many studies have investigated water management to improve the PEMFC performance and proposed some solutions, for instance, optimization of
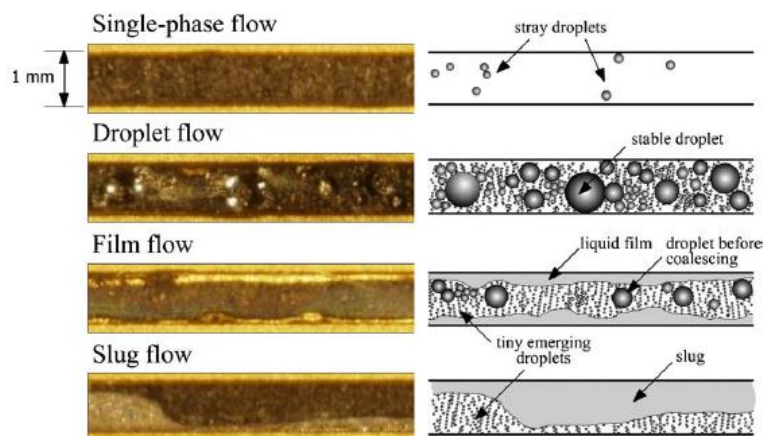
Figure 6. The various form and distributions of liquid water in the flow channel [58].

porous media of gas diffusion layer, catalyst layer, and bipolar plate. The results of the partial flooded two-dimensional PEMFC model [59] presented that one of the factors in decreasing the chance of flooding is high temperature. Partial flooding makes the distribution of current density uneven, and it has an unfavorable influence on PEMFC performance. Mammar et al. [60] investigated a fuzzy logic technique to study the

membrane's hydration level.

Intending to study water flooding and how to solve this problem in PEMFC, Li *et al*. [61] have evaluated several studies in the field of water management in PEMFC. Modifying the structure and the material of membrane electrode assembly and system design and engineering are two strategies to reduce the flooding issue in PEMFC.
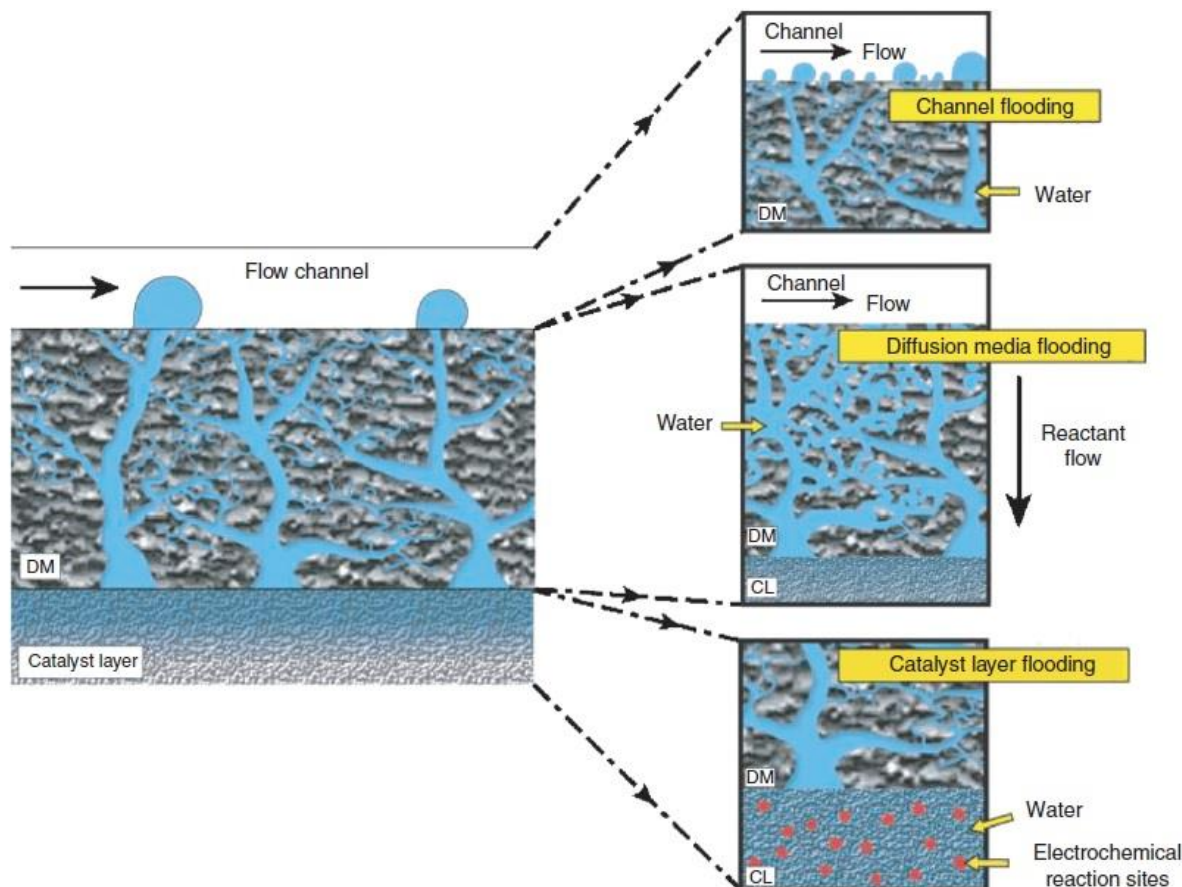
Figure 7. The possible sites of flooding in a PEMFC [62].

CONCLUSION

In recent years, modeling has attracted tremendous attention and interest in understanding PEMFC phenomena. To reduce the time and cost of experiments, fuel cell designers and engineers could get the benefits of using parametric models to predict the fuel cell performance by given operating conditions, geometries, and properties of materials. This review summarizes the different modeling methods for PEMFC and explains their characteristics.

The empirical/semi-empirical models are designed for particular fields and should be changed for every operating condition or application. These models provide a calculation for the performance of PEMFC in a short time; therefore, the empirical/semi-empirical models are more suitable for problems that focus on

controlling. The analytical models are helpful for simple designs with short-time computing processes and calculating water management and voltage losses. The analytical approach does not include membrane resistance or mass transport restrictions, which are important for PEMFC performance. Mechanistic models focus on thermodynamics, fluid dynamics, and electrochemistry and explain a fuel cell's basic actions, including flow pattern, pressure drop, distribution of current density, and voltage. The mechanistic models are suited for optimization and design applications.

Hybrid models have better performance and overcome the pure models' disadvantages. The reason to use a hybrid model that consists of mechanistic and empirical approaches is that the usage of both approaches have advantages in improving the model and defeats the disadvantages of each of them, and

improves the performance of the PEMFCs. Furthermore, in a hybrid model, the parameters for operation are reduced because of the fewer input dimensions. The other advantages of the combined model over the empirical and mechanistic model are that it can be utilized for any operating condition and application and easily does not need extensive range calculation. This review illustrates optimization methods for parametric PEMFC models by applying different algorithms, like GA, PSO, etc.

The zero-dimensional model is uncomplicated in discovering the different losses that occur in the system, comparing them with each other, and concluding the kinetic parameters and general ohmic resistance from data. One dimensional model is the first model that researchers established to study the fuel cell. It was a complicated model with a sandwich domain in the y-direction. These models give massive details in different operating conditions for fuel cells by examining the temperatures, mass concentrations, electrical potentials, and fluxes. The Sandwich model in the *y-z* or *x-y* directions is a two-dimensional, upgraded version of the one-dimensional model. Two-dimensional sandwich models could examine the influence of channel geometry, bipolar plates, heat, mass transfer, and fluxes on fuel cells. A three-dimensional model in the *x-y-z* direction is the most appropriate model to analyze PEMFC in every detail, for instance, current density distribution, the influence of flow field design on fuel cell performance, or bipolar plate blockage impact. It also presents the multiphase flow; there are two and three-phase flow in the PEMFC. Some models, such as the VOF model, have used multiphase mixture and multi-fluid to examine phase change and water production in PEMFC. The interface in the gas-liquid flow can be detected and transported by the VOF model. The VOF model can record the surface tension as a significant force in the micro-channel flows. The multiphase mixture model examines a mix of phases instead of the separated phases. Applying the multiphase mixture model is more proficient in the pressure of the gas phase than the pressure of the liquid phase. The multi-fluid model works effectively in high saturation conditions, although the multi-fluid model tends to be unstable because of the coupled phases and variables.

The characterization of PEMFC simulation has an essential part. This review shows that the influence of different parameters on PEMFC performance can be identified more easily by applying CFD coding. Hence, other CFD softwares are also explained in PEMFC modeling.

Flooded models are important to examine water management in PEMFC. These models can investigate the water in the PEMFC and present solutions to improve the performance.

ACKNOWLEDGMENTS

List of Abbreviations

ADE	Adaptive Differential Evolution
AFC	Alkaline Fuel Cell
BSOA	Balanced Seagull Optimization Algorithm
CFD	Computational Fluid Dynamics
DE	Differential Evolution
DMFC	Direct Methanol Fuel Cell
GA	Genetic Algorithm
GDL	Gas Diffusion Layer
HADE	Hybrid adaptive differential evolution
LM	Levenberg-Marquardt
MCFC	Molten Carbonate Fuel Cell
MEA	Membrane Electrolyte Assembly
MPSO	Modified Particle Swarm Optimization
PAFC	Phosphoric Acid Fuel Cell
PEMFC	Proton Exchange Membrane Fuel Cell
PSO	Particle Swarm Optimization
PTFE	Poly Tetra Fluoro Ethylene
SOA	Seagull Optimization Algorithm
SOFC	Solid Oxide Fuel Cell
SVRM	Support Vector Regression Machine
VOF	Volume of Fluid

Greek Letters

γ	Convection correction
σ	Conductivity (S m^{-1})
ρ	Density (kg m^3)
μ	Dynamic viscosity (Pa s)
ϕ	Electric potential (V)
α_m	Mass accommodation coefficient
ε	Porosity

List of symbols

c_P	Specific heat capacity (J g^{-1} K^{-1})
D	Diffusivity (m^2 s^{-1})
D	Diameter (m)
E	Cell potential (V)

F	Faraday's constant (96485 C mol^{-1} e^{-1})
K	Permeability
R	Universal gas constant (8.314 J mol^{-1} K^{-1})
P	Pressure (Pa)
p	Partial pressure (Pa)
$\vec{U}$	Velocity (m s^{-1})
S_m	Mass conservation
S_M	Momentum conservation
S_k	Species conservation
S_E	Energy conversion
S_e	Electrical charges
S_i	Ionic charges
T	Temperature (K)
t	Time (s)
$\vec{V}$	Velocity (m s^{-1})
w	Mass fraction

REFERENCES

[1]   U. Lucia, Renewable Sustainable Energy Rev. 30 (2014) 164–169. https://doi.org/10.1016/j.rser.2013.09.025

[2]   J. Macedo-Valencia, J.M. Sierra, S.J. Figueroa-Ramírez, S.E. Díaz, M. Meza, Int. J. Hydrogen Energy 41 (2016) 23425–23433. https://doi.org/10.1016/j.ijhydene.2016.10.065

[3]   T. Elmer, M. Worall, S. Wu, S.B. Riffat, Renewable Sustainable Energy Rev. 42 (2015) 913–931. https://doi.org/10.1016/j.rser.2014.10.080

[4]   Y. Chang, Y. Qin, Y. Yin, J. Zhang, X. Li, Appl. Energy 230 (2018) 643–662. https://doi.org/10.1016/j.apenergy.2018.08.125

[5]   N. Limjeerajarus, P. Charoen-amornkitt, Int. J. Hydrogen Energy 40 (2015) 7144–7158. https://doi.org/10.1016/j.ijhydene.2015.04.007

[6]   P. Pei, H. Chen, Appl. Energy 125 (2014) 60–75. https://doi.org/10.1016/j.apenergy.2014.03.048

[7]   S.A. Atyabi, E. Afshari, J. Therm. Anal. Calorim. 135 (2019) 1823–1833. https://doi.org/10.1007/s10973-018-7270-3

[8]   J.P. Kone, X. Zhang, Y. Yan, G. Hu, G. Ahmadi, J. Comput. Multiphase Flows 9 (2017) 3–25. https://doi.org/10.1177/1757482X176923

[9]   N. Ahmadi, S. Rezazadeh, A. Dadvand, I. Mirzaee. J. Renewable Energy Environment 2 (2015) 36-46. https://doi.org/10.30501/jree.2015.70069

[10]   A.A. El-Ferganya, H.M. Hasanien, A.M. Agwa, Energy Convers. Manage. 201 (2019) 112197. https://doi.org/10.1016/j.enconman.2019.112197

[11]   D. Hao, J. Shen, Y. Hou, Y. Zhou, H. Wang, Int. J. Chem. Eng. 2016 (2016) 4109204. https://doi.org/10.1155/2016/4109204

[12]   Y. Akimoto, K. Okajima, J. Energy Technol. Policy 1 (2014) 91–96. https://doi.org/10.1080/23317000.2014.972480

[13]   M. Pan, C. Li, J. Liao, H. Lei, C. Pan, X. Meng, H. Huang, Energy 207 (2020) 1–13. https://doi.org/10.1016/j.energy.2020.118331

[14]   M. Ohenoja, A. Sorsa, K. Leiviskä, Computers 7 (2018) 60–72. https://doi.org/10.3390/computers7040060

[15]   A.U. Thosar, H. Agarwal, S. Govarthan, A.K. Lele, Chem. Eng. Sci. 206 (2019) 96–117. https://doi.org/10.1016/j.ces.2019.05.022

[16]   J.X. Liu, H. Guo, F. Ye, C.F. Ma, Energy 119 (2017) 299–308. https://doi.org/10.1016/j.energy.2016.12.075

[17]   R.K.A. Rasheed, Q. Liao, Z. Caizhi, S.H. Chan, Int. J. Hydrogen Energy 42 (2017) 3142–3165. https://doi.org/10.1016/j.ijhydene.2016.10.078

[18]   B. Grondin-Perez, S. Roche, C. Lebreton, M. Benne, C. Damour, J.A. Kadjo, Engineering 6 (2014) 418–426. https://doi.org/10.4236/eng.2014.68044

[19]   E.J.F. Dickinson, G. Hinds, J. Electrochem. Soc. 166 (2019) 221–231. https://doi.org/10.1149/2.0361904jes

[20]   J. Lu, Ph.D. Thesis, James Cook University, North Queensland, Australia, (2013). https://researchonline.jcu.edu.au/40440/

[21]   Z. Sun, N. Wang, Y. Bi, D. Srinivasan, Energy 90 (2015) 1334–1341. https://doi.org/10.1016/j.energy.2015.06.081

[22]   H. Abdi, N.A. Messaoudene, L. Kolsi, M.W. Naceur, J. Therm. Anal. Calorim. 144 (2021) 1749–1759. https://doi.org/10.1007/s10973-020-10370-1

[23]   M. Sarvi, I. Soltani, Int. J. Comput. Sci. Eng. Technol. 3 (2012) 285–378. https://ijcset.com/docs/IJCSET12-03-08-036.pdf

[24]   S.Z. Chen, Z.G. Bao, Y.C. Wang, Appl. Mech. Mater. 740 (2015) 474–478. https://doi.org/10.4028/www.scientific.net/AMM.740.474

[25]   P. Hu, G. Cao, X. Zhu, J. Li, Simulation Model. Pract. Theory 18 (2010) 574–588. https://doi.org/10.1016/j.simpat.2010.01.001

[26]   A. Omran, A. Lucchesi, D. Smith, A. Alaswad, A. Amiri, T. Wilberforce, J.R. Sodr´, A.G. Olabi, Int. J. Thermofluids 11 (2021) 100–110. https://doi.org/10.1016/j.ijft.2021.100110

[27]   J. Cheng, G. Zhang, Int. J. Electr. Power Energy Syst. 62 (2014) 189–198. https://doi.org/10.1016/j.ijepes.2014.04.043

[28]   K. Priya, T.S. Babu, K. Balasubramanian, K.S. Kumar, N. Rajasekar, Sustain. Energy Technol. Assess. 12 (2015) 46–52. https://doi.org/10.1016/j.seta.2015.09.001

[29]   Y. Cao, X. Kou, Y. Wu, K. Jermsittiparsert, A. Yildizbasi, Energy Rep. 6 (2020) 813–823. https://doi.org/10.1016/j.egyr.2020.04.013

[30]   Y. Li, Z. Ma, Z. Zheng, D. Li, Z. Lu, B. Xu, Membranes 11 (2021) 1–16. https://doi.org/10.3390/membranes11090691

[31]   Y. Cao, Y. Li, G. Zhang, K. Jermsittiparsert, N. Razmjooy, Energy Rep. 5 (2019) 1616–1625. https://doi.org/10.1016/j.egyr.2019.11.013

[32]   P. Schneider, C. Sadeler, A. C. Scherzer, N. Zamel, D. Gerteisen, J. Electrochem. Soc. 166 (2019) F322. https://doi.org/10.1016/j.egyr.2019.11.01310.1149/2.0881904jes

[33]   Z.P. Du, C. Steindl, S. Jakubek, Processes 9 (2021) 713. https://doi.org/10.3390/pr9040713

[34]   Y. Nalbant, C.O. Colpan, Y. Devrim, Int. J. Hydrogen Energy 43 (2018) 5939–5950. https://doi.org/10.1016/j.ijhydene.2017.10.148

[35]   Y. Sohn, S. Yim, G. Park, M. Kim, S. Cha, K. Kim, Int. J. Hydrogen Energy 42 (2017) 13226–13233. https://doi.org/10.1016/j.ijhydene.2017.04.036

[36]   H. Jiang, L. Xu, H. Struchtrup, J. Li, Q. Gan, X. Xu, Z. Hu, M. Ouyang , J. Electrochem. Soc. 167 (2020) 1–18. https://doi.org/10.1149/1945-7111/ab6ee7

[37]   J.A. Salva, A. Iranzo, F. Rosa, E. Tapia, Int. J. Hydrogen Energy 41 (2016) 20615–20632. https://doi.org/10.1016/j.ijhydene.2016.09.152

[38]   S. Liu, T. Chen, Y. Xie, Int. J. Green Energy 17 (2020) 255–273. https://doi.org/10.1080/15435075.2020.1722133

[39]   J.X. Liu, H. Guo, F. Ye, C.F. Ma, Energy 119 (2017) 299–

308. https://doi.org/10.1016/j.energy.2016.12.075

[40] V. Ionescu, N. Buzbuchi, Energy Procedia 112 (2017) 390–397. https://doi.org/10.1016/j.egypro.2017.03.1085

[41] S.A. Saco, R.T.K. Raj, P. Karthikeyan, Energy 113 (2016) 558–573. https://doi.org/10.1016/j.energy.2016.07.079

[42] M. Jourdani, H. Mounir, A. Marjani, Int. J. Multiphys. 11 (2017) 427–442. https://doi.org/10.21152/1750-9548.11.4.427

[43] D.G. Caglayan, B. Sezgin, Y. Devrim, I. Eroglu, Int. J. Hydrogen Energy 41 (2016) 10060–10066. https://doi.org/10.1016/j.ijhydene.2016.03.049

[44] A. d'Adamo, M. Haslinger, G. Corda, J. Höflinger, S. Fontanesi, T. Lauer, Processes 9 (2021) 688. https://doi.org/10.3390/pr9040688

[45] Z. Niu, J. Wu, Z. Bao, Y. Wang, Y. Yin, K. Jiao, Int. J. Heat Mass Transfer 139 (2019) 58–68. https://doi.org/10.1016/j.ijheatmasstransfer.2019.05.008

[46] A. Di. Le, B. Zhou. J. Power Sources 182 (2008) 197–222. https://doi.org/10.1016/j.jpowsour.2008.03.047

[47] A. Di. Le, B. Zhou. J. Power Sources 182 (2008) 197–222. https://doi.org/10.1016/j.jpowsour.2008.01.047

[48] N.S.M. Hassan, W.R.W. Daud, K. Sopian, J. Sahari, J. Power Sources 193 (2009) 249–257. https://doi.org/10.1016/j.jpowsour.2009.01.066

[49] L. Xing, X. Liu, T. Alaje, R. Kumar, M. Mamlouk, K. Scott, Energy 73 (2014) 618–634. https://doi.org/10.1016/j.energy.2014.06.065

[50] Z. Zhang, W. Liu, Y. Wang, Int. J. Hydrogen Energy 44 (2019) 379–388. https://doi.org/10.1016/j.ijhydene.2018.05.149

[51] G. Zhang, L. Fan, J. Sun, K. Jiao, Int. J. Heat Mass Transfer 115 (2017) 714–724. https://doi.org/10.1016/j.ijheatmasstransfer.2017.07.102

[52] C. Siegel, Energy 33 (2008) 1331–1352.

[53] J. Shen, Z. Tu, S. H. Chan. Appl. Therm. Engineering 149 (2019) 1408–1418. https://doi.org/10.1016/j.applthermaleng.2018.12.138

[54] Y. Shen, B. Zhao, T. H. Kwan, Q. Yao. Energy Convers. Manage. 213 (2020) 112840–112855. https://doi.org/10.1016/j.enconman.2020.112840

[55] J. Shen, Z. Tu, S. H. Chan. Appl. Therm. Engineering 164 (2020) 114464–114473. https://doi.org/10.1016/j.applthermaleng.2019.114464

[56] M. Sauermoser, N. Kizilova, B. G. Pollet, S. Kjelstrup. Frontiers in Energy Research 8 (2020). https://doi.org/10.3389/fenrg.2020.00013

[57] Z. Liu, Z. Mao, C. Wang. J. Power Sources 158 (2006) 1229–1239. https://doi.org/10.1016/j.jpowsour.2005.10.060

[58] I. S. Hussaini, C. Y. Wang. J. Power Sources 187 (2009) 444–451. https://doi.org/10.1016/j.jpowsour.2008.11.030

[59] J. Shen, L. Xu, H. Chang, Z. Tu, S. H. Chan. Energy Convers. Manage. 207 (2020) 112537–112545. https://doi.org/10.1016/j.enconman.2020.112537

[60] K. Mammar, F. Saadaoui, S. Laribi. Renewable Energy Focus 30 (2019) 123–130. https://doi.org/10.1016/j.ref.2019.06.001

[61] H. Li, Y. Tang, Z. Wang, Z. Shi, S. Wu, D. Song, J. Zhang, K. Fatih, J. Zhang, H. Wang, Z. Liu, R. Abouatallah, A. Mazza. J. Power Sources 178 (2008) 103–117. https://doi.org/10.1016/j.jpowsour.2007.12.068

[62] E.C. Kumbur, M.M. Mench, in Encyclopedia of Electrochemical Power Sources, J. Garche Ed., Elsevier B.V., (2009), p. 828-847. ISBN 978-0-444-52745-5.

SAHRA HAMDOLLAHI
LUO JUN

School of Mechatronic Engineering and Automation, Shanghai University, Shanghai, China

PREGLEDNI RAD

MODELOVANJA VODONIČNE GORIVNE ĆELIJE: PREGLDENI RAD

Gorivne ćelije su elektrohemijski uređaji koji pretvaraju hemijsku u električnu energiju. Među njima, vodonična gorivna ćelija se smatra jednim od najperspektivnijih kandidata za izvore energije sledeće generacije zbog svoje velike gustine snage, nulte emisije i niske radne temperature. Poslednjih godina modelovanje je dobilo ogromnu pažnju i interesovanje za razumevanje i proučavanje fenomena vodoničnih gorivnih ćelija. Ovaj pregledni rad prikazuje nedavni napredak u modelovanju vodoničnih gorivnih ćelija. Empirijski, polu-empirijski, analitički i mehanistički modeli, nulto do trodimenzionalni modeli i modeli višefaznog toka, kao što su višefazne smeše, multifluidni i VOF modeli, su različite vrste pristupa modelovanju vodoničnih gorivnih ćelija u smislu parametarskog, dimenzionalnog i dvo- ili trofaznog protoka. On osvetljava važnost kombinovanja različitih strategija modelovanja i identifikacije parametara u modelima vodoničnih gorivnih ćelija, kako bi se postigli precizni modeli koji smanjuju vreme i troškove eksperimenata.

Ključne reči: vodonična gorivna ćelija, modelovanje, performanse gorivne ćelije, empirijski/polu-empirijski model, model višefaznog toka.

TEKU KALYANI[1]
LANKAPALLI SATHYA VARA PRASAD[1]
ADITYA KOLAKOTI[2]

[1]Department of Mechanical Engineering, Andhra University College of Engineering(A), Visakhapatnam, India

[2]Department of Mechanical Engineering, Raghu Engineering College(A), Visakhapatnam, India

PREPARATION AND PHYSICOCHEMICAL PROPERTIES OF NATURALLY GROWN GREEN *SPIROGYRA* ALGAE BIODIESEL

Article Highlights
- Cultivation of green algae for 120 days without any externally supplied chemicals or nutrients
- The maximum amount of dried algae powder to algae oil was achieved
- B10 to B100 diesel-biodiesel blends are prepared and characterized
- Mathematical equations are developed for analyzing the fuel properties
- B40 was proposed as an optimum blend ratio for further engine experiments

Abstract

In this study, biodiesel was produced from a naturally grown green algae (Spirogyra). The algae were cultivated in an open pond for 180 days without any fertilizers or nutrients. The dried algae powder to oil yield and significant fuel properties of viscosity, density, cetane number, calorific value, flash point, pour, and cloud points are investigated for B10 to B100 blends. The results of solvent oil extraction show that at a 1:2 (algae powder to solvent) ratio and 65 °C, algae oil yield was 22.66%. Furthermore, Box-Behnken assisted response surface optimization technique was implemented. From the 29 random experiments, 96.24% Spirogyra algae oil biodiesel (SAOBD) yield was achieved under the optimum conditions of 50 °C, 180 minutes, the molar ratio of 9:1, and catalyst concentration of 0.5 wt%. The fatty acid composition reveals that 73.95 wt% saturated FAC was observed in SAOBD. The significant fuel properties are measured by following ASTM-D6751 standards, and 40% SAOBD in diesel fuel could be an optimum blend ratio for engine experimentation. Finally, regression equations with high correlation coefficients (R^2) were developed to predict the various blend ratios for the fuel properties.

Keywords: algae biodiesel, algae cultivation, fuel properties.

SCIENTIFIC PAPER

Fossil fuel-derived petro-diesel is considered one of the primary fuels in the transportation, agricultural and industrial sectors. The high efficiency, availability, and low cost of petro-diesel during the earlier days of its discovery made them a popularly used fuel. However, with the rapid consumption, fossil fuel availability is on the verge of extinction. Furthermore, the exhaust emission from the petro-diesel fuelled engines contributes to the depletion of air quality and increases global environmental air pollution levels [1]. Therefore, the search for clean-burning and renewable fuels is gaining wide attention. To mitigate the challenge, research on different feedstock oils confirmed that biodiesel derived from naturally available oils could replace the existing petro-diesel fuel [2]. Moreover, biodiesel is popular for its non-toxicity, biodegradability, low carbon, and high oxygen profiles [2]. In general, second-generation oils like non-edible (jatropha, pongamia, mahua, neem, etc.) and low-cost feedstocks (waste cooking oils) are commonly used for the production of biodiesel [3]. However, these oils still face impediments like availability, cultivation in arable lands, high free fatty acid (FFA) content, low yield, etc. Therefore, research on third-generation

algae oils [4] is gaining wide popularity among the nations for biodiesel production.

Algae oils have various classifications based on their growth and climatic conditions. The major types are green algae, blue-green algae, red algae, brown algae, phytoplankton, seaweeds, and other algae strains [4]. They mainly rely on the influence of sunlight and Carbon-dioxide (CO_2) for their growth. Compared to first and second-generation oils, algae have the fastest growth rate, produce more oil, and survive in highly saline waters. Furthermore, algae require limited nutrients for their growth with high lipid content (40% to 80%) and high triglycerides than any other terrestrial plants [5]. Studies reveal that algae cultivation and oil extraction are cost-effective. More than 85% of the oil can be extracted if the correct type of algae species is selected [5]. However, the separation and extraction of cellular components of algae are considered one of the cost drivers during the conversion of algae to biodiesels [6].

The concept of algae oil to biodiesel is not a new invention in this 21st century, as the first scientific study on algae was started at the end of the 19th century. However, with the increase in population and pollution, the search for renewable and alternative fuels has become imperative. Therefore, researchers are inclining toward algae cultivation, harvesting, oil extraction, and refining using fresh and marine water. The algae cultivation in seawater [7] attracts researchers due to the maximum share of water on the earth's surface. Furthermore, they don't require any chemical fertilizers for their growth which can save money and energy. The microalgae biomass production in seawater has a great potential for mass production with full utilization of ocean resources, including temperature control, wave energy for mixing, and culture medium preparation [8]. On the other hand, algae cultivation in fresh water and wastewater [9,10] is also popular. Currently, with the advent of the latest technology from industry 4.0 [11], the maximum benefit of extracting the oil from microalgae and converting it to biodiesel is made more economical with the latest optimization and artificial intelligence (AI) tools [12–14].

From the above discussions, it is evident that there is a great scope for algae oil as a sustainable fuel. In the present study, an attempt is made to cultivate algae (*Spirogyra*) without using fertilizers or chemicals in an open tank from June 2021 to December 2021. The algae were collected at regular intervals of 15 days from August 2021 to December 2021, processed for oil extraction, and further transesterified to biodiesel. The physicochemical properties of prepared biodiesel (B10 to B100) are reported.

MATERIAL AND METHODS

Cultivation of *Spirogyra* algae

The cultivation of green algae (*Spirogyra*) is located at 83°24′53.96′′E (83.414994) longitude and 17°59′39.26′′N (17.99424) latitude from June 2021. The cultivation of green algae (*Spirogyra*) is carried out in an open tank of 7.9 m in length, 4.2 m in width, 2 m in external depth, and 1.6 m in internal depth. A maximum temperature of 32.9 °C and a minimum temperature of 19.6 °C were observed from June 2021 to December 2021 in the location. The average temperature was recorded as 26.8 °C, and the pH value varied from 5.76 to 7.32. Similarly, the average sun hours for this period are observed as 10.1. The temperature and natural sunlight play a significant role in algae cultivation, especially outdoor. As algae are ubiquitous photosynthetic organisms, sunlight is an essential source for autotrophic growth and photosynthetic activity. From the available literature [15], it is evident that 20 °C to 30 °C is considered an optimum temperature for the growth of a wide range of algae, and the light irradiation varies from 33 μmol m^{-2}s^{-2} to 40 μmol m^{-2}s^{-2} to achieve maximum growth rate. Therefore, proper care is taken in achieving the required temperature and light for algae cultivation. Initially, the tank is filled with fresh water, and green water from the nearby pond/river is mixed with the freshwater to initiate the algae growth process. As stated in the introduction, no chemicals or fertilizers were used to grow algae. However, the essential nutrients are supplied naturally from rainfall, sunlight, and carbon dioxide due to the cultivation in an open atmosphere. After the desired growth of algae is observed in the tank, the green algae (*Spirogyra*) is collected and processed for oil extraction. The processing involves cleaning algae with deionized water, separating wet algae layer by layer, and drying it under natural sunlight for 10 hours. The dried *Spirogyra* is powdered and stored in an airtight container for further process.

Extraction of *Spirogyra* algae oil

The oil can be extracted from algae using physical techniques, like ball milling, microwave heating, and ultrasonication, and chemical methods, like solvent extraction, lyophilization, and supercritical CO_2 methods. Each technique has its advantages and limitations [16]. In this study, the oil was extracted from *Spirogyra* algae by the solvent extraction method using a Soxhlet apparatus. The setup consists of a temperature control heater, condenser, Soxhlet extractor, and other necessary glass beakers. The optimum extraction conditions were applied to achieve maximum benefit in the extraction of *Spirogyra* algae

oil. A measured quantity of 300 grams of *Spirogyra* algae powder (SAP) is loaded in the Soxhlet extraction chamber with 600 ml of solvent *n*-hexane in the round bottom flask and heated to 65 °C and maintained throughout the process. The vapors of *n*-hexane flow up to the reflux condenser, where it is cooled by circulating cold water. The condensed *n*-hexane was combined with dry algae powder in the extraction chamber, and the mixture later flowed through the siphon arm into the round bottom flask. The process continued until the entire algae powder in the extraction chamber was consumed, and the mixture of algae oil and *n*-hexane was collected in the round bottom flask through the siphon tube. After 18 hours of extraction, the prepared SAO is separated from the solvent through steam distillation. The *Spirogyra* oil was stored in an airtight glass beaker for transesterification. The extracted algae oil efficiency can be estimated using the equation below Eq. (1).

$$\text{Algae oil efficiency}\,(wt\%) = \frac{\text{Mass of oil extracted }(grams)}{\text{The total mass of dried algae}} \times 100 \quad (1)$$

Transesterification process

The obtained algae oil, through the steam distillation process, is heated up to 110 °C to remove traces of water content in algae oil. Later, the basic fuel properties of *Spirogyra* algae are estimated. It is observed that the kinematic viscosity of the *Spirogyra* algae oil (SAO) is above 19 mm^2/s, density is 898.2 kg/m^3, and FFA is 1.69%. Therefore, the high viscous SAO is transesterified into low viscous *Spirogyra* algae oil biodiesel (SAOBD) by the transesterification process [17,18]. Homogeneous catalyst sodium hydroxide (NaOH) and methanol (CH$_3$OH) were used to initiate the transesterification reaction process. A temperature-controlled hot plate magnetic stirrer, glass beakers, and a thermometer were used for the transesterification process. Initially, the desired quantity of raw SAO is taken in the glass beaker and placed on a hot plate magnetic stirrer. The catalyst and methanol are later added to the contents. Until the oil reaches the rated temperature, the contents are stirred continuously. During this process, the oil's triglycerides were transformed into methyl esters (SAOBD) and glycerine. After separation from glycerine, the obtained SAOBD was washed with warm deionized water and heated to remove the water. Then, the SAOBD was blended with mineral diesel fuel at various proportions starting from 10% to 90%, with an increment of 10% by volume. For instance, B10 represents 900 ml of diesel fuel blended with 100 ml of SAOBD10. A high-speed stirrer was utilized for blending the fuels, and each blend was prepared by stirring continuously for 30 min.

Table 1. Process variables and their ranges

S. No	Parameters	Codes	Low Level	Medium Level	High Level
1	Catalyst (wt.%)	X_1	0.5	1	1.5
2	Temperature (°C)	X_2	45	50	55
3	Time (min)	X_3	60	120	180
4	Molar ratio	X_4	6:1	9:1	12:1

The same procedure is repeated with varying process variables like catalyst, alcohol, time, and temperature to identify the influential parameter in the transesterification process as per the matrix design (DOE) using Minitab-19 statistical software, as shown in Table 1. Box-Behnken (BB) designed response surface method (RSM) was used to optimize the process parameters to achieve maximum algae biodiesel yield. A total of 29 experiments were conducted randomly by varying the process parameters, as shown in Figure 1a, and the experimental biodiesel yield was calculated using Eq. (2). Different physicochemical properties of the SAOBD were determined. The blended fuel properties are compared with the popularly followed three international fuel standards of ASTM-D6751, EN-14214, and IS-15607, as shown in Table 2.

$$\text{Biodiesel yield}\,(\%) = \frac{\text{Weight of biodiesel produced}}{\text{Weight of oil used}} \times 100 \quad (2)$$

Yield and model fitting
Spirogyra algae oil yield estimation

The wet algae of 10 kg were collected every 15 days from the pond, and later, it was cleaned. After cleaning almost 40% of the weight was lost by unwanted materials like mud, snails, etc., attached to the *Spirogyra* algae. The cleaned *Spirogyra* algae were dried and ground into a fine powder for further lab-scale oil extraction. The same procedure was repeated, and the algae were collected at regular intervals for 120 days.

For the lab-scale algae oil extraction, 300 grams of the dried *Spirogyra* algae powder was used along with solvent (*n*-hexane) in a ratio of 1:2. The yield from each batch was 68 ml of *Spirogyra* algae oil. Hence, 8.4 kg of dry-cleaned algae powder yielded 1.9 liters of algae oil, further used for estimating physicochemical properties. After the steam distillation, the maximum quantity of *n*-hexane was recovered, which can be reused for subsequent experimental trials. As a result, the SAO yield calculated using Eq. (1) was 22.66%.

a) Experimental design with varying process parameters

b) Experimental and RSM biodiesel yield

c) Actal and Predicted biodiesel yield
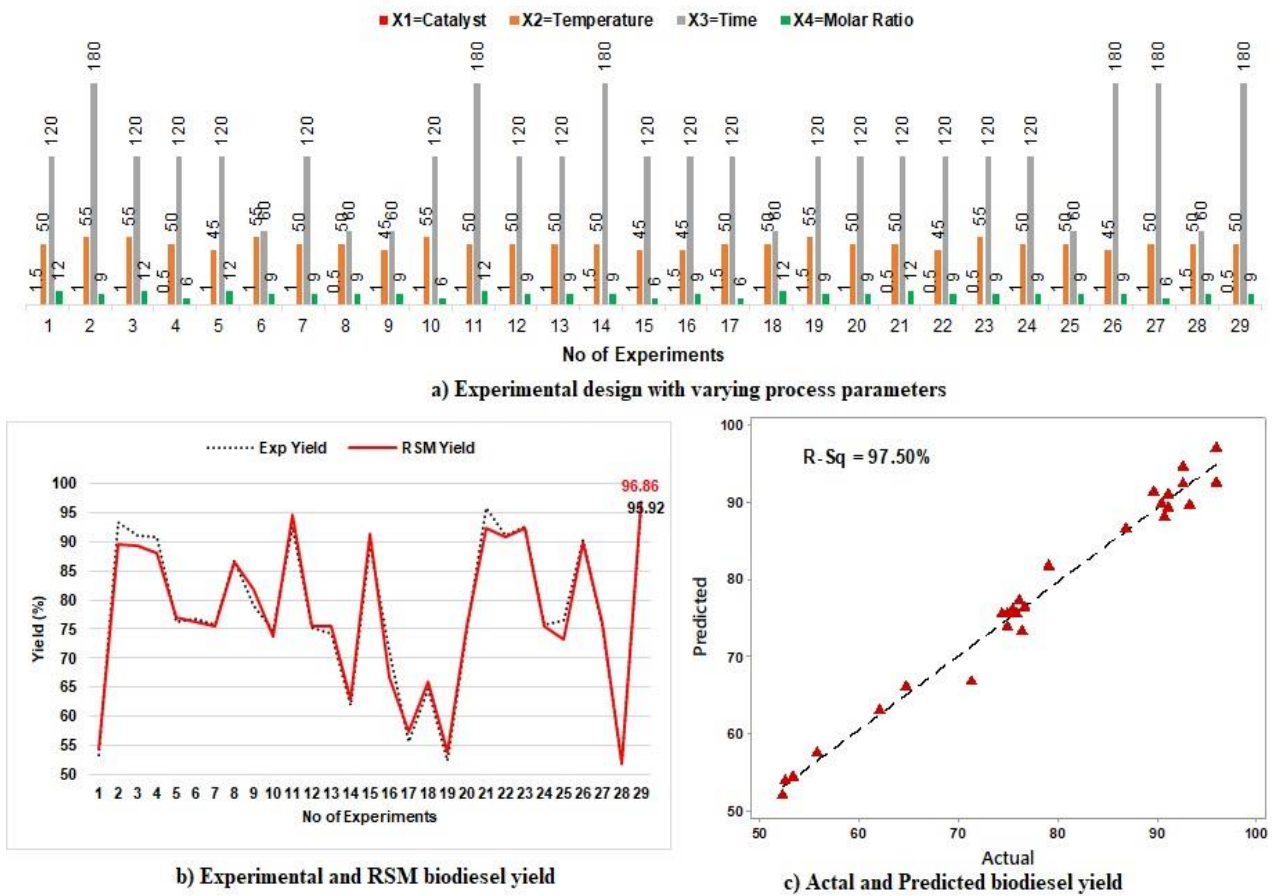
Figure 1. Number of experiments and their yield estimation results.

Table 2. International biodiesel fuel property standards and their range [19]

S. No	Properties	Units	IS-15607	EN-14214	ASTM-D6751
1	Kinematic viscosity at 40 °C	mm^2/sec	2.5–6	1.9–6.0	3.5–5.0
2	Density at 15 °C	kg/m^3	860–900	860–900	860–890
3	Flash point	°C	min 120	min 93	min 120
4	Calorific value	kJ/kg	-	-	-
5	Cetane number	-	min 51	min 47	min 51
6	Cloud point	°C	-	-	-3 – -12
7	Pour point	°C	-	-	-15 – -16

Biodiesel yield and model fitting

During the transesterification process, the significant process variables like alcohol, catalyst, time, and temperature were varied randomly to achieve a maximum biodiesel yield. As shown in Figure 1b, the maximum biodiesel yield (based on 29 experimental trials) of 95.92% was achieved with the alcohol-to-SAO molar ratio of 9:1 and the catalyst amount of 0.5 wt.% at 50 °C for 180 min. The statistically predicted maximum biodiesel yield of 96.86% was in close agreement with the experimental yield. Subsequently, confirmation tests, conducted under the optimum conditions in triplicate, resulted in an average yield of 96.24%.

Based on the 29 experimental data, a regression equation was developed to find the relation between the process variables (X_1, X_2, X_3, and X_4) and biodiesel yield (%). The quadratic model is presented by Eq. (3):

The model's accuracy was assessed through the coefficient of determination R^2 and the adjusted coefficient of determination Adj R^2, which were 97.50% and 95%, respectively. Therefore, more than 97% of the variance was attributed to the variables. The same is evident in Figure 1c, comparing the predicted and actual biodiesel yields.

$$Yield(\%) = 899 + 109.4(X_1) - 26.70(X_2) - 0.779(X_3) - 32.39(X_4) - 15.80(X_1 \cdot X_1) + 0.2347(X_2 \cdot X_2) + 0.000830(X_3 \cdot X_3)$$
$$+ 0.615(X_4 \cdot X_4) - 2.027(X_1 \cdot X_2) + 0.0046(X_1 \cdot X_3) - 1.26(X_1 \cdot X_4) + 0.00431(X_2 \cdot X_3) + 0.497(X_2 \cdot X_4) + 0.0498(X_3 \cdot X_4)$$

(3)

The influencing process parameter from the set of four variables that show a significant effect in achieving maximum biodiesel yield can be analyzed with the ANOVA analysis, shown in Table 3. The statistically significant process variables can be found with the *p*-test. The lowest *p*-value with the highest *F*-value denotes the most influencing parameter in achieving the biodiesel yield from SAO. The catalyst concentration (X_1) is identified as a significant process parameter, followed by the reaction time (X_3). Furthermore, there is only a 0.01% chance that a large *F*-value may occur due to noise, and the probability of the value greater than F and less than 0.050 represents the model terms are significant. Similarly, the values greater than 0.100 represent the model as insignificant. Finally, the model *F*-values is 38.99, which is significant, and the lack of fit is non-significant.

Analysis of fatty acid compositions

Fatty acid composition (FAC) in biodiesels is predominant for biodiesel fuel properties. Therefore, FAC was tested using the gas chromatography method [20]; the results are shown in Table 4. In the present investigation, palmitic acid was identified as a major component with 28.63 wt.%, followed by lauric acid (21.90 wt.%) and oleic acid (21.62 wt.%). As a result, the total saturated fatty acid content was 73.95 wt.%, with the maximum share of palmitic acid, and the total unsaturated fatty acid content was 24.12 wt.%. The available studies [20,21] showed that a highly unsaturated FAC in biodiesel promotes a rise in viscosity and a decrease in heating value. On the other hand, saturated FAC in biodiesel will help regulate NOx emissions during combustion [22,23]. Table 4 compares the present FAC profile with the literature [24].

Table 3. Analysis of variance (ANOVA)

Source	DF	Adj SS	Adj MS	F-value	P-value	
Model	14	5012.34	358.02	38.99	<0.0001	S[a]
Linear	4	3877.77	969.44	105.56	<0.0001	S
X_1	1	3538.05	3538.05	385.26	<0.0001	S
X_2	1	22.94	22.94	2.50	0.136	NS[b]
X_3	1	314.50	314.50	34.25	<0.0001	S
X_4	1	1.17	1.17	0.13	0.727	NS
Square	4	444.22	111.05	12.09	<0.0001	S
X1*X1	1	102.36	102.36	11.15	0.005	NS
X_2*X_2	1	225.78	225.78	24.59	<0.0001	S
X_3*X_3	1	54.10	54.10	5.89	0.029	NS
X_4*X_4	1	12.96	12.96	1.41	0.255	NS
2-Way interaction	6	550.80	91.80	10.00	<0.0001	S
X_1*X_2	1	102.72	102.72	11.19	0.005	NS
X_1*X_3	1	0.08	0.08	0.01	0.929	NS
X_1*X_4	1	14.40	14.40	1.57	0.231	NS
X_2*X_3	1	6.68	6.68	0.73	0.408	NS
X_2*X_4	1	221.86	221.86	24.16	<0.0001	S
X_3*X_4	1	205.06	205.06	22.33	<0.0001	S
Error	14	128.57	9.18			
Lack-of-fit	10	127.02	12.70	32.77	0.002	NS
Pure error	4	1.55	0.39			
Total	28	5140.91				

[a] S - Significant, [b] NS - Non-significant.

Table 4. Comparison of the present with available literature FAC profiles

S.No.	FAC	Structure C:D	SAOBD100 (wt.%)	Algae Biodiesel [24]
1	Caprylic Acid	C8:0	0.3	-
2	Capric Acid	C10:0	0.3	-
3	Lauric Acid	C12:0	21.90	-
4	Myristic Acid	C14:0	15.29	-
5	Palmitic Acid	C16:0	28.63	15.64
6	Stearic Acid	C18:0	4.86	2.10
7	Oleic Acid	C18:1	21.62	54.89
8	Linoleic Acid	C18:2	2.5	4.88
9	Arachidic Acid	C20:0	1.28	2.24
10	Behenic Acid	C22:0	1.39	0.33
	Other		1.93	

RESULTS AND DISCUSSION

Physicochemical properties of *Spirogyra* biodiesel

The fuel properties play a significant role during combustion, storage, and transportation. Therefore, studying the significant fuel properties gives an insight into the physical and chemical behavior during usage. Moreover, research on biodiesels is becoming imperative due to their improved fuel properties. Therefore, SAOBD was blended with mineral diesel fuel (B10 to B100), and the significant fuel properties were studied using the international standard ASTM-D6751.

Kinematic viscosity

The viscosity of liquid fuel plays a predominant role during fuel injection. Therefore, it is always recommended to use low viscous fuels, which help achieve better fuel atomization during combustion and eliminate the fuel injector clogging. In this study, the kinematic viscosity was measured by a redwood viscometer as per the ASTM-D445. The variations of the kinematic viscosity are plotted in Figure 2. Pure biodiesel (SAOBD100) has a maximum kinematic viscosity of 4.23 mm^2/sec, which is 51.61% higher than mineral diesel fuel (2.79 mm^2/sec) due to the presence of large size triglyceride molecules in the SAO. High viscous fuels are not recommended for diesel engine combustion, resulting in incomplete combustion, thereby increasing toxic exhaust emissions. However, due to high compression ratios in diesel engines, pure biodiesels are also tested by different research groups [25] and claim that the efficiency is improved.

Furthermore, as observed in jatropha biodiesel, the kinematic viscosity change narrows beyond 60 °C [26]. Figure 2 shows that kinematic viscosity decreases with the increase in diesel percentage in the blend (Table 2).
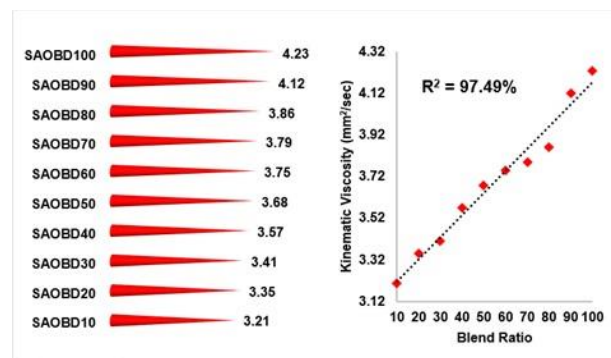
Figure 2. Variation of kinematic viscosity with the coefficient of determination.

Density

Density is measured with a relative density meter by following the ASTM-D1298 standards, and the variations are shown in Figure 3a. A high density characterizes the biodiesel (887 kg/m^3) due to its high molecular weight compared to mineral diesel fuel (830 kg/m^3). Like kinematic viscosity, the density of pure biodiesel is reduced by adding diesel fuel. The fuel density affects the fuel performance, the quality of atomization, and combustion quality as diesel engines utilize the fuel injection pump system to admit the fuel into the combustion chamber. Due to high density, the required quantity of fuel mass may not reach the combustion chamber, which alters the fuel/air ratio, low energy content, and low power output of the engine. The density of methyl or ethyl esters depends mainly on the molar mass, water content, and free fatty acids [21]. However, the density of the blends with the SAOBD content higher than 60% meets the required standards.

Cetane number

The quality of combustion in diesel engines depends on the cetane value of the fuel. Therefore,
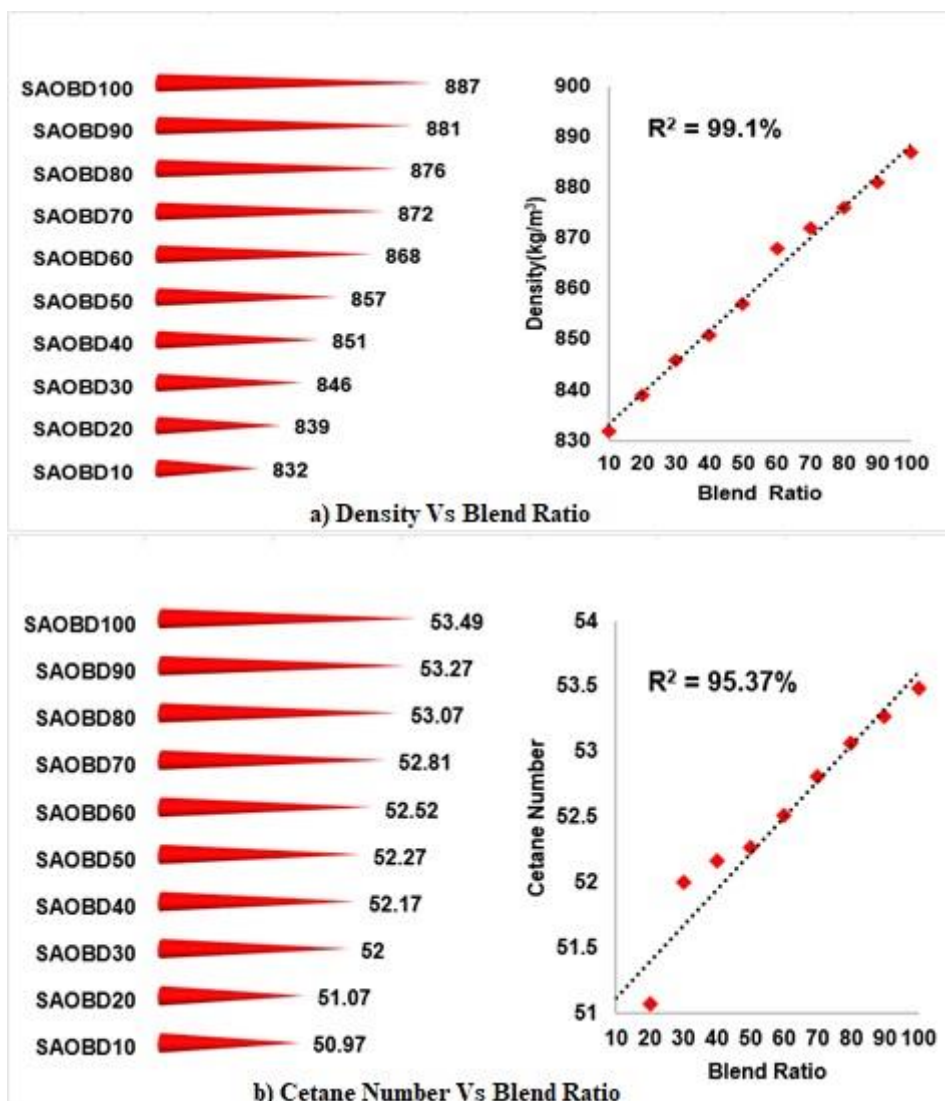
Figure 3. Variation of density and cetane number with the coefficient of determination.

a high cetane number of fuels are always recommended for a diesel engine as they reduce the delay period. Compared to diesel fuel, biodiesel possesses a relatively high cetane number due to the fatty acid compositions [20]. Figure 2b presents the cetane value for various blends. The cetane value increases with the increase in biodiesel percentage in the blends, as shown in Table 2. The international standards recommend the minimum cetane number of 47. In the present study, the values of cetene number for all the diesel-biodiesel blends are within the limits of the prescribed standards.

Calorific value

The calorific value or heating value is considered one of the significant fuel properties, as the engine's fuel consumption and power output mainly rely on it. The heating value reveals the information on the heat liberated by burning a unit mass of fuel. Biodiesels obtained from different feedstocks of plant and animal oils generally have a lower heating value than diesel fuel. It may vary due to the chemically bonded oxygen molecules in biodiesels. Furthermore, the heating value of biodiesel increases with the number of carbon atoms and decreases with the number of double bonds [19]. The heating values determined in the present study using a bomb calorimeter following ASTM-D240 standards are shown in Figure 4a. Unlike viscosity and density, the calorific value decreases with the increase in biodiesel percentage in the blends with diesel fuel.

Flash point

Transportation and storage of fuel are essential for fuel commercialization, and this smooth operation can be achieved with less volatility fuels like biodiesel. The biodiesels possess high flash points, which helps in safe transportation, storage, and distribution. Approximately the flashpoint of biodiesel is 150% more
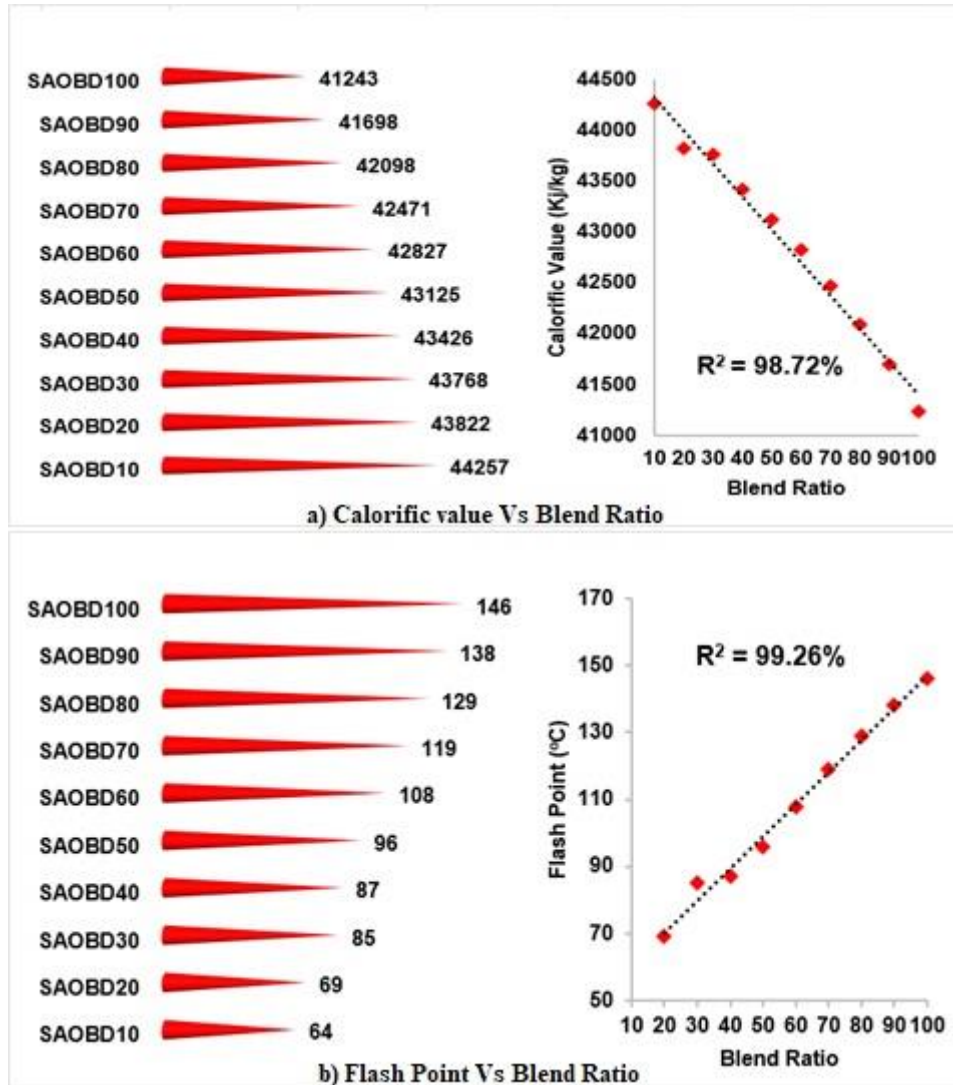
Figure 4. Variation of calorific value and flash point with the coefficient of determination.

than mineral diesel fuel, and these high flashpoints in biodiesels ensure less flammability hazards. The flashpoint for biodiesel-diesel blends was measured with a Pensky marten closed cup apparatus following the ASTM-D93 standards; the results are shown in Figure 4b.

Low-temperature fuel properties

The physicochemical properties of the fuel significantly affect the temperature change (high or low) as the fuel properties may alter, especially at low temperatures. This change is predominant for biodiesel due to saturated and unsaturated fatty acid compositions. Moreover, biodiesels are more likely to react to atmospheric conditions, especially at low temperatures. Therefore low-temperature fuel properties like pour and cloud points were measured following ASTM-D97 and ASTM-D2500 standards, respectively; the data for various blends are shown in

Figures 5a and 5b. The cloud point reveals the information of the minimum temperature at which wax crystallizes or clouds will start when the fuel is cooled down. Similarly, the fuel starts taking gel shapes for the pour point and has no more flowability at minimum temperature. Both the properties of diesel-biodiesel blends appear to be within the limits of the established international fuel standards.

Optimum blend ratio and mathematical modeling

The blends of 10% and 20% biodiesel with diesel fuel, popularly known as B10 and B20, are currently being applied worldwide. These blends meet the essential requirements of various international standards and can be used without any modification to the engine design [23,25] as there is a great concern to fuel refinement policies to mitigate the challenges of energy and the environment. Therefore, researchers are focusing on blending more biodiesel percentage

into diesel fuel. This study shows the tested fuel properties, like kinematic viscosity, density, cetane number, calorific value, flash point, pour point, and cloud point, for all the blends (B10 to B100) as per the international standards of ASTM-D6751 are within limits. Based on these results, a 40% SAOBD blend with diesel fuel may be recommended for further engine performance analysis as it meets the other international fuel standards. For instance, the kinematic viscosity, cetane number, and calorific values of the B40 are optimum (Table 2). However, above a 40% blend ratio, the kinematic viscosity, which plays a vital role in

combustion atomization, increases. Hence, the SAOBD40 blend was chosen as the optimum for further investigation. The fuel properties of SAOBD10 to SAOBD100 are in close agreement with the available literature [27]. Furthermore, regression equations with coefficient of determination R^2 (Table 5) were developed using Minitab19 statistical software to predict the significant fuel properties of B10 to B100. A similar investigation has been carried out with mahua and jatropha oil-based biodiesels, resulting in the mathematical equations for different diesel-biodiesel blends [27,28].
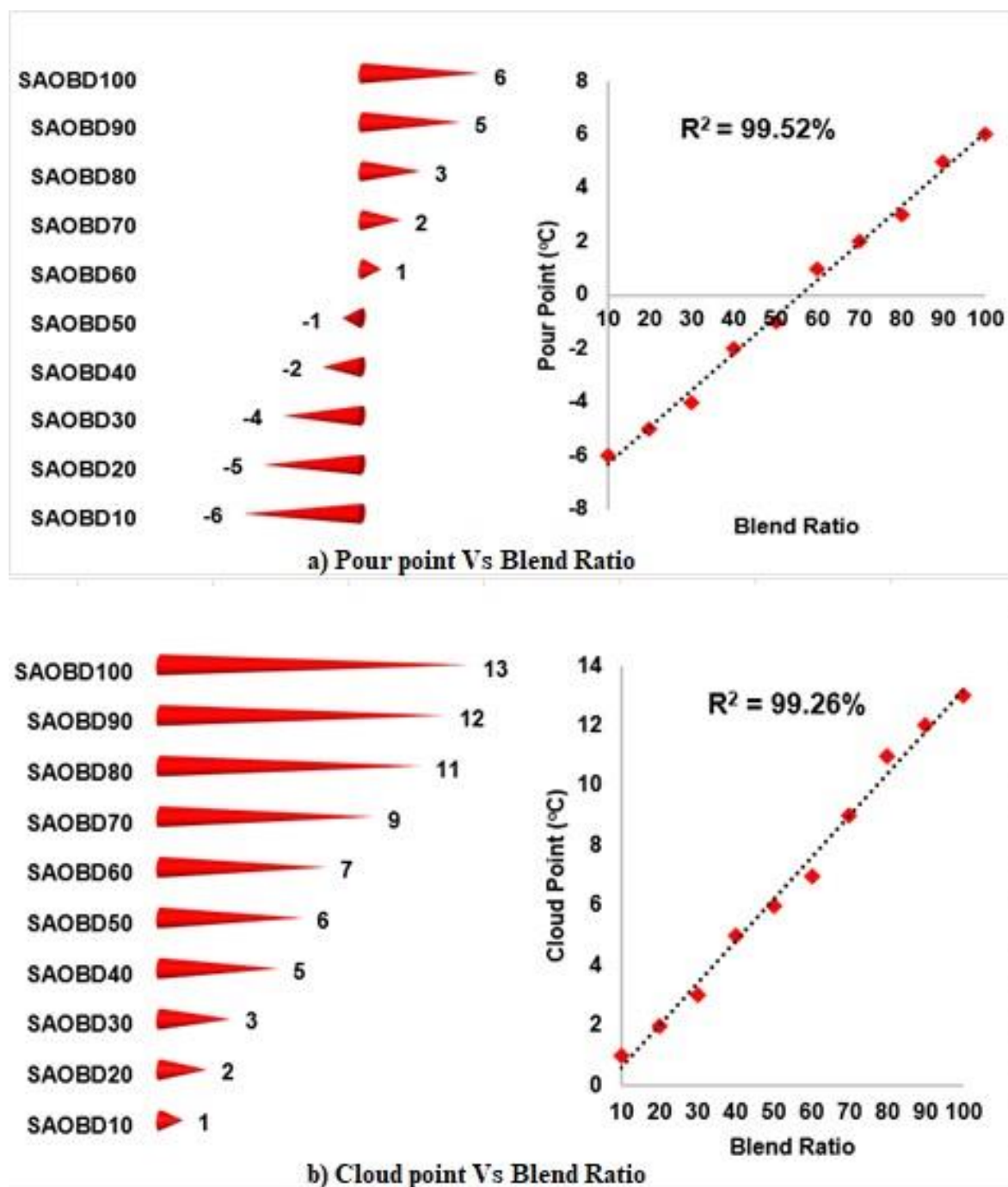
Figure 5. Variation of pour point and cloud point with the coefficient of determination.

Table 5. Mathematical equations for unknown blend ratios

S. No	Property	R^2, %	Adj R^2, %	Mathematical relationship
1	Kinematic viscosity (mm^2/s), 40 °C	97.49	97.17	3.1120+0.010636(X)
2	Density (kg/m3), 15 °C	99.1	99.0	827.1+0.6139(X)
3	Cetane number	95.37	94.79	50.844+0.02764(X)
4	Calorific value (kJ/kg)	98.72	98.56	44657.1-32.43(X)
5	Flash point (°C)	99.26	99.17	52.47+0.9388(X)
6	Pour point (°C)	99.52	99.46	-7.667+0.13578(X)
7	Cloud point (°C)	99.26	99.17	-0.800+0.14000(X)

CONCLUSION

Biodiesel production from algae oil is gaining great potential due to its high conversion rate (raw oil to biodiesel), and it can be grown in any water. In the present study, an attempt is made to cultivate and extract oil from *Spirogyra* algae, and based on the observations, the following conclusions are summarized.

The *Spirogyra* algae are grown naturally without externally supplied nutrients or chemical fertilizers. However, the average temperature of 26.25 °C and sun hours of 10.1 must be maintained for better algae cultivation. The maximum algae oil yield of 22.66% is achieved for a 1:2 ratio (algae powder to solvent), and 90% of the solvent is recovered and reutilized. The maximum algae oil biodiesel yield of 96.24% is achieved during the transesterification process, and catalyst concentration is identified as a significant process variable in ANOVA analysis.

The significant fuel properties for the blends (SAOBD10 to SAOBD100) are characterized as per ASTM-D6751 and observed within the limits of ASTM-D6751, EN-14214, and IS-15607. The optimum blend for engine experimentation may be proposed as SAOBD40 due to the optimum kinematic viscosity (3.57 mm^2/sec), cetane number (52.17), and calorific values (43426 kJ/kg). The regression equations developed for fuel properties achieve the highest coefficient of determination (R^2).

REFERENCES

[1]   V. Ahire, M. Shewale, A. Razban, Arch. Comput. Methods Eng. 28 (2021) 4897–4915. https://doi.org/10.1007/s11831-021-09558-x.

[2]   I. Ambata, V. Srivastavaa, M. Sillanpääa, Renewable Sustainable Energy Rev. 90 (2018) 356–369. https://doi.org/10.1016/j.rser.2018.03.069.

[3]   S.G. Mungodla, L.Z. Linganiso, S. Mlambo, T. Motaung, J. Eng. Des. Technol. 17 (2019) 670–704. https://doi.org/10.1108/JEDT-07-2018-0111.

[4]   C.G. Khoo, Y.K. Dasan, M.K. Lam, K.T. Lee, Bioresour. Technol. 292 (2019) 121964. https://doi.org/10.1016/j.biort ech.2019.121964.

[5]   A. Jacob, B. Ashok, A. Alagumalai, O.H. Chyuan, P.T.K. Le, Energy Convers. Manage. 228 (2021) 113655. https://doi.org/10.1016/j.enconman.2020.113655.

[6]   P. Mäki-Arvela, I. Hachemi, D.Y. Murzin, J. Chem. Technol. Biotechnol. 89 (2014) 1607–1626. https://doi.org/10.1002/jctb.4461.

[7]   X. Zhai, C. Zhu, Y. Zhang, H. Pang, F. Kong, J. Wang, Z. Chi, Sci. Total Environ. 738 (2020) 139439. https://doi.org/10.1016/j.scitotenv.2020.139439.

[8]   P. Mehta, R. Rani, R. Gupta, A.S. Mathur, S.K. Puri, Algal Res. 36 (2018) 88– 95. https://doi.org/10.1016/j.algal.2018 .10.015.

[9]   J. Masojídek, G. Torzillo, Encycl. Ecol. (2008) 2226–2235. https://doi.org/10.1016/B978-008045405-4.00830-2.

[10]   Widayat, J. Philia, J. Wibisono, E3S Web Conf., 2nd Int. Conf. Energy, Environ. Inf. Syst. (ICENIS 2017), 31, Semarang, Indonesia, (2018) p.3. https://doi.org/10.1051/e3sconf/20183104009.

[11]   M. Setiyo, T.A. Purnomo, D. Yuvenda, M.K. Biddinika, N.A.C. Sidik, O.D. Samuel, A. Calam, A. Kolakoti, Mech. Eng. Soc. Ind. 1 (2021) 3–6. https://doi.org/10.31603/mesi.5309.

[12]   S.Y. Teng, G.Y. Yew, K. Sukačová, P.L. Show, V. Máša, J.S. Chang, Biotechnol. Adv. 44 (2020) 107631. https://doi.org/10.1016/j.biotechadv.2020.107631.

[13]   A. Kolakoti, M. Setiyo, B. Waluyo, Mech. Eng. Soc. Ind. 1 (2021) 22–30. https://doi.org/10.31603/mesi.5320.

[14]   S. Prabakaran, T. Mohanraj, A. Arumugam, Renewable Energy 180 (2021) 353–371. https://doi.org/10.1016/j.renene.2021.08.073.

[15]   S.P. Singh, P. Singh, Renewable Sustainable Energy Rev. 50 (2015) 431– 444. https://doi.org/10.1016/j. rser.2015.05.024.

[16]   G. Bhargavi, P.N. Rao, S. Renganathan, IOP Conf. Ser. Mater. Sci. Eng. Hyderabad, India, 330 (2018) 012024. https://doi.org/10.1088/1757-899X/330/1/012024.

[17]   A. Kolakoti, G. Satish, Aust. J. Mech. Eng. (2020) 1–13. https://doi.org/10.1080/14484846.2020.1842298.

[18]   S. Prabakaran, T. Mohanraj, J. Mech. Sci. Technol. 35 (2021) 4765–4773. https://doi.org/10.1007/s12206-021-0942-0.

[19]   I. Barabás, I.A. Todoruţ, in Textbook of Biodiesel-Quality, Emissions and By-Products, In Tech Open book series, G. Montero Ed., London (2011) p.3–28. ISBN: 978-953-307-784-0; EBOOK (PDF) ISBN: 978-953-51-4402-1.

[20]   A. Kolakoti, B.V.A. Rao, Biofuels 10 (2019) 591–605. https://doi.org/10.1080/17597269.2017.1332293.

[21]   A. Kolakoti, B. Prasadarao, K. Satyanarayana, M. Setiyo, H. Köten, M. Raghu, Automot. Exper. 5 (2022) 3–15. https://doi.org/10.31603/ae.6171.

[22]   B. Prasadarao, A. Kolakoti, P. Sekhar, Recent Adv.

Comput. Sci. Commun. 14 (2021) 1824–1832. https://doi.org/10.2174/2666255813666191204143202.

[23] S.Prabakaran, R.Manimaran, T.Mohanraj, M.Ravikumar, Mater. Today: Proc. 45 (2021) 2784–2788. https://doi.org/10.1016/j.matpr.2020.11.742.

[24] F. Yasar, Fuel 264 (2020) 116817. https://doi.org/10.1016/j.fuel.2019.116817.

[25] V.A.R. Basava, A. Kolakoti, P.R. Kancherla, in Handbook of Research on Advancements in Manufacturing, Materials, and Mechanical Engineering, Leonid Burstein, IGI Global, Hershey (2021), p.25–53. https://doi.org/10.4018/978-1-7998-4939-1.ch002.

[26] A. Kolakoti, B.V.A. Rao, Int. J. Automot. Mech. Eng. 17 (2020) 8052– 8066. https://doi.org/10.15282/ijame.17.2.2020.23.0604.

[27] N. Acharya, P. Nanda, S. Panda, S. Acharya, Eng. Sci. Technol. Int. J. 20 (2017) 511–517. https://doi.org/10.1016/j.jestch.2016.12.005.

[28] N.S. Dugala, G.S. Goindi, A. Sharma, J. King. Saud. Univ. Eng. Sci. 33 (2021) 424–436. https://doi.org/10.1016/j.jksues.2020.05.006.

TEKU KALYANI[1]
LANKAPALLI SATHYA VARA PRASAD[1]
ADITYA KOLAKOTI[2]

[1]Department of Mechanical Engineering, Andhra University College of Engineering(A), Visakhapatnam, India

[2]Department of Mechanical Engineering, Raghu Engineering College(A), Visakhapatnam, India

NAUČNI RAD

DOBIJANJE I FIZIČKOHEMIJSKA SVOJSTVA BIODIZELA NA BAZI PRIRODNO GAJENE ZELENE ALGE (*SPIROGIRA*)

U ovoj studiji, biodizel je proizveden od prirodno uzgajanih zelenih algi (spirogira). Alge su uzgajane u otvorenom bazenu 180 dana bez ikakvih đubriva ili hranljivih materija. Istraživani su prinos ulja iz osušenih algi u prahu i značajna gorivna svojstva mešavine B10 do B100, kao što su viskoznost, gustina, cetanski broj, toplotna moć, tačka paljenja, tačka tečenja i tačka zamućenja. Rezultati ekstrakcije ulja rastvaračem pokazuju da je pri odnosu alga:rastvarač 1:2 na 65 °C prinos ulja algi iznosio 22,66%. Nadalje, primenjena je tehnika optimizacije površine odziva uz pomoć Boks-Benkenivim planom (29 eksperimenata). Prinos biodizela iz ulja alge od 96,24% je postignut pod optimalnim uslovima od 50 °C, 180 min, molskog odnosa 9:1 i koncentracije katalizatora od 0,5%. Sadržaj estara zasićenih masnih kiselina u biodizelu je 73,95%. Značajna gorivna svojstva su određena prema standardima ASTM-D6751. Optimalna mešavina za eksperimentisanje sa motorom sadrži 40% biodizela. Takođe, razvijene su regresione jednačine sa visokim koeficijentima determinacije koje predviđaju gorivna svojstva za različite odnose namešavanja..

Ključne reči: algalni biodizel, gajenje algi, gorivna svojstva.